PREDICTION OF THE THREE-PHASE COEXISTENCE CONDITIONS OF PURE METHANE AND CARBON DIOXIDE HYDRATES USING MOLECULAR DYNAMICS SIMULATIONS

A Thesis

by

JOSEPH GAMAL NESSIM COSTANDY

Submitted to the Office of Graduate and Professional Studies of
Texas A&M University
in partial fulfillment of the requirements of the degree of

MASTER OF SCIENCE

Chair of Committee,	Ioannis G. Economou
Co-Chair of Committee,	Marcelo Castier
Committee Member,	Eyad Masad
Head of Department,	M. Nazmul Karim

August 2015

Major Subject: Chemical Engineering

Copyright 2015 Joseph Gamal Nessim Costandy

ABSTRACT

Clathrate hydrates are solid crystals that consist of three-dimensional networks of hydrogen-bonded water molecules forming well-defined cages within which small “guest“ molecules are needed in order to stabilize the structures. More than 130 different molecules can form hydrates when mixed with water at relatively low temperatures and high pressures, including methane, ethane, propane, iso-butane, carbon dioxide, nitrogen and hydrogen. The accurate prediction of thermodynamic properties of clathrate hydrates has gained much attention due to the relevance of clathrate hydrates to many industrial applications. For example, hydrates play a major role in the problem of flow assurance in the oil and gas industry. They are also being considered for use in gas transport and separation applications. In addition, the existence of methane hydrates in large quantities in nature makes them a potential energy source.

In this work, Molecular Dynamics (MD) simulations have been used in order to determine the Hydrate – Liquid water – Guest coexistence line for methane and carbon dioxide hydrates. The direct phase coexistence method was used where slabs of the three constituent phases were separately equilibrated and then brought in contact at the conditions under investigation. In order to account for the stochastic nature of the hydrate growth and dissociation processes, many long, independent simulations at different conditions of temperature and pressure were conducted while avoiding bubble formation phenomena. This allowed for performing a statistical averaging of the results to identify the three-phase coexistence temperature at different pressures. Also, the erroneous use of dispersion tail corrections was investigated.

For methane hydrates, where the Lorentz-Berthelot combining rules for the two force fields used gave accurate predictions for the solubility of methane in the aqueous phase, this approach yielded predictions that are in good agreement with experimental data. A correction to the Lorentz-Berthelot cross-interaction energy parameter was applied in the case of carbon dioxide hydrates to obtain accurate predictions of the solubility of carbon dioxide in the aqueous phase, which in turn resulted in equally accurate and consistent predictions of the three-phase coexistence temperature. Therefore, it was shown that both the water-water and water-guest interactions play an important role in the application of this methodology to the study of clathrate hydrate systems. For systems where the water-guest interactions can accurately predict guest solubility in water, the predictions of the three-phase coexistence are as accurate as the water force field used to predict the melting of ice.

It was also shown that the methodology cannot be directly applied to low pressures for carbon dioxide hydrates, where a liquid-like layer of carbon dioxide is adsorbed at the water surface. Several possible causes for this deficiency are suggested, including the possible effect of box anisotropy and box size fluctuations at low pressures.

DEDICATION

To my parents, brother and sister for their persistent care over my well-being, and for believing in me, supporting my decisions, and encouraging me unwaveringly at every step of my career.

ACKNOWLEDGEMENTS

I would like to thank my supervisor Professor Ioannis Economou for granting me a research assistantship to fund my Master's of Science degree, and providing me with all the necessary training and guidance to gain the essential expertise for accomplishing the results presented in this work. I would also like to thank him for being a mentor to me in all my decisions over the course of my Master's degree, and for helping me plan the next steps in my career. I would also like to give special thanks to Drs. Vasileios Michalis, Ioannis Tsimpanogiannis, and Othon Moultos for their patience, and for the time that they committed to train me in using the tools needed for this work. In addition, I would like to thank Professors Marcelo Castier and Eyad Masad, my graduate committee members, who made themselves available to answer and provide useful insights into the problems that were faced while conducting the research. Also, I would like to thank all staff in the Texas A&M University in College Station and Qatar campuses for their continuous efforts to facilitate and improve my student experience at the university.

I am very grateful for the financial support provided by NPRP Grant No. 6-1547-2-632 from the Qatar National Research fund (a member of the Qatar Foundation). Also, I am grateful to the High Performance Computing Center of Texas A&M University at Qatar for the generous resource allocation.

TABLE OF CONTENTS

Page

ABSTRACT ii

DEDICATION iv

ACKNOWLEDGEMENTS v

TABLE OF CONTENTS vi

LIST OF FIGURES viii

LIST OF TABLES xiii

NOMENCLATURE xiv

1. INTRODUCTION 1

    1.1 Applications of Methane Hydrates 3
    1.2 Applications of Carbon Dioxide Hydrates 4
    1.3 Objectives of Current Study 5

2. FUNDAMENTALS OF MD SIMULATIONS 6

    2.1 History and Overview of MD Simulations 6
    2.2 System Setup 10
        2.2.1 Initial Particle Positions and Velocities 10
        2.2.2 Energy Minimization 12
        2.2.3 Periodic Boundary Conditions 14
    2.3 The Potential Energy Function 16
        2.3.1 Bonded Parameters 17
        2.3.2 Non-Bonded Parameters 19
    2.4 Leap-Frog Integration 25
    2.5 MD Simulations in the NPT Ensemble 27

3. CLATHRATE HYDRATES LITERATURE REVIEW 31

3.1 Hydrate Crystal Structures and Phase Equilibrium 31
    3.1.1 Methane Hydrates Phase Equilibria 35
    3.1.2 Carbon Dioxide Hydrates Phase Equilibria 36
3.2 MD Simulations of Clathrate Hydrates 38
    3.2.1 Water, Methane, and Carbon Dioxide Force Fields 38
    3.2.2 Three-Phase Coexistence from MD Simulations 41

4. METHODOLOGY 48

4.1 Initial Configuration Preparation 49
4.2 Force Field Description 52
4.3 Simulation Details 56

5. RESULTS AND DISCUSSION 58

5.1 Application of the Direct Phase Coexistence Method to Methane Hydrates 59
    5.1.1 Hydrate Growth Characteristics 59
    5.1.2 Stochastic Nature of Hydrate Growth and Dissociation 64
    5.1.3 Calculation of T_3 of Methane Hydrates 69
    5.1.4 Effect of Dispersion Tail Corrections 76
    5.1.5 Calculation of Methane Solubility in the Aqueous Phase 78
    5.1.6 Summary of Findings of Methane Hydrate Study 80
5.2 Application of the Direct Phase Coexistence Method to Carbon Dioxide Hydrates 81
    5.2.1 Equilibration of the WCW Configuration 81
    5.2.2 Calculation of T_3 Using LB Combining Rules 84
    5.2.3 Optimizing the Cross-Interaction Parameters 87
    5.2.4 Calculation of T_3 Using Modified Parameters 92
    5.2.5 Inconsistency in Prediction of T_3 at Low Pressure 97
    5.2.6 Summary of Findings of Carbon Dioxide Hydrate Study 101

6. CONCLUSIONS AND FUTURE WORK 103

REFERENCES 107

APPENDIX A: METHANE HYDRATE TEMPERATURE SCANS 118

APPENDIX B: CARBON DIOXIDE HYDRATE TEMPERATURE SCANS 123

LIST OF FIGURES

Page

FIG. 1. MD simulation algorithm.[77] 9

FIG. 2. A schematic representation of periodic boundary conditions.[71] 15

FIG. 3. Lennard-Jones (12-6) Potential.[76] The red, dashed line illustrates the concept of truncation beyond a cutoff length, rc, LJ. 21

FIG. 4. The three common hydrate unit crystal structures.[42] 32

FIG. 5. Methane hydrate experimental three-phase diagram, showing the H-L_w-V_{CH4} equilibrium points(x), I-H-V_{CH4} equilibrium (+), and the I-L_w-H-V_{CH4} quaternary point (■).[2] 36

FIG. 6. Carbon dioxide hydrate experimental three-phase diagram, showing the H-L_w-V equilibrium points(x), I-H-VCO2 equilibrium (+),the I-L_w-H-V_{CO2} quaternary point (■), the H- V_{CO2}-L_{CO2} equilibrium (○), and the H-L_w-L_{CO2} (△) equilibrium.[2] The pure carbon dioxide saturation line is also shown.[94] 37

FIG. 7. Snapshots of the HWCW system at 1000 bar, showing the initial configuration, and two final states above and below T_3 that correspond to hydrate dissociation and growth, respectively. The water molecules are represented by the red and black lines. The carbon dioxide molecules are represented by the blue spheres (carbon) and pink cylinders (oxygen). 48

FIG. 8. Three snapshots of a typical trajectory of the WHWM system at 294 K and 600 bar (run no. 4 of Fig. 9): (a) initial configuration at t = 0 ns,(b) intermediate step at t = 600 ns, and (c) final state at t = 1500 ns. The red and white lines represent the water molecules and the blue spheres represent the methane molecules.[153] 60

FIG. 9. Potential energy vs time for five independent NPT simulation runs of 1500 ns at 294 K and 600 bar. The inset figure focuses on the second stage of hydrate growth for the case of run no. 2.[153] 61

FIG. 10. Snapshots of a trajectory of the WHWM system at 290 K and 400 bar where (a) a thin methane slab is shown at t = 972.6 ns, and (b) 0.7

ns later a methane bubble has been formed. The red and white lines represent the water molecules and the blue spheres represent the methane molecules.[153] 63

FIG. 11. Time evolution of the potential energy of five different runs at 283 K and 100 bar near equilibrium conditions.[153] 66

FIG. 12. Time evolution of the potential energy of two variations of temperature scans at 100 bar. Although the pressure and temperatures are the same for both figures (a) and (b), different independent runs have been selected in each scenario. In the case of figure (a) the calculated T_3 is 280 K while in the case of figure (b) it is 286 K.[153] 67

FIG. 13. Time evolution of the potential energy of five independent runs at 296 K and 400 bar. The dashed line denotes the value of the potential energy at three-phase equilibrium state.[153] 68

FIG. 14. Indicative temperature scans of time evolution of the potential energy for different pressure values of (a) 40, (b) 400 and (c) 600 bar.[153] 70

FIG. 15. Experimental[170] and calculated values from this work and from the literature for the three-phase coexistence temperature of the methane hydrate system (Conde and Vega,[148] Tung *et al.*,[150] Jensen *et al.*,[149] and Smirnov and Stegailov[152]). All authors used TIP4P/Ice except Tung *et al.* who used TIP4P/Ew. The expected values presented in the figure are defined as $T_{3,expected} = T_{3,experimental} - 3.15$ K.[153] 73

FIG. 16. Density of methane in a methane–water–methane configuration at 280 K and 100 bar, with and without dispersion corrections. The dashed line depicts the experimental value of the pure methane reported by NIST.[94,153] 78

FIG. 17. Methane solubility in water as a function of the three-phase coexistence temperature. Circles denote MD calculations and lines denote continuum-scale models.[2,153,172] 79

FIG. 18. Snapshot of the liquid water – vapor carbon dioxide interface after equilibration of the WCW system at 30 bar and 274 K, showing the film of carbon dioxide on the water surface. The water molecules are represented by the red and black lines, while the carbon dioxide molecules are represented by the blue spheres (carbon) and pink cylinders (oxygen). The inset figure shows the full system before and after equilibration. 83

FIG. 19. Density of carbon dioxide (black squares) and water (red circles) along the direction normal to the interface (x axis) in the WCW system at 30 bar and 274 K (vapor carbon dioxide). The dashed line represents the experimental value of the density of pure carbon dioxide [94]. The solid lines are a guide to the eye only. 83

FIG. 20. Evolution of the potential energy with time of the HWCW system using the TIP4P/ice model for water and the LB combining rules at 1000 bar and four different temperatures. 86

FIG. 21. Snapshot of the CWC configuration after 50 ns using the LB combining rules. Molecule representation is the same as Fig. 18. 91

FIG. 22. Number density profile of carbon dioxide and water in the CWC system. The red area represents the number of carbon dioxide molecules in the volume between 3 and 10 nm of the x axis. The sum of the red and grey areas gives the number water molecules in the same region. 91

FIG. 23. Dependence of the carbon dioxide solubility (mole fraction) on the modification factor of the LB cross-interaction energy parameter for the case of TIP4P/ice (red up triangles) and TIP4P/2005 (blue down triangles) at 400 bar and 286 K. The solid black line depicts the experimental solubility.[179] 92

FIG. 24. Experimental and calculated values of T_3 for carbon dioxide hydrates from this work (triangles) and from Tung *et al*.[163] (pink diamonds), and Miguez *et al.*[156] (green pentagons (TIP4P/ice) and orange circles (TIP4P/2005)). The red upside-up triangles represent results obtained using the TIP4P/ice force field, and the blue, upside-down triangles represent results obtained using the TIP4P/2005 force field. Open points indicate the runs were conducted using the LB combining rules, while the filled points indicate that the appropriate modification factor for the force field was applied. The red and blue dashed lines represent the expected values of T_3 for the TIP4P/ice ($T_{3,expected} = T_{3,experimental} - 3.15$ K) and TIP4P/2005 ($T_{3,expected} = T_{3,experimental} - 22.7$ K) force fields, respectively. Experimental T_3 line obtained by polynomial fit from data collection of Sloan and Koh.[2] The pure CO_2 saturation points are shown using grey squares.[94] 94

FIG. 25. Box x dimension as a function of time for the WCW system at 20 bar and 279 K. 100

FIG. 26. Runs conducted at 40 bar. The calculated temperature is $T_3 = 273.0$ K with a standard deviation of 2.4 K. 119

FIG. 27. Runs conducted at 100 bar. The calculated temperature is T_3 = 282.8 K with a standard deviation of 2.3 K. 120

FIG. 28. Runs conducted at 400 bar. The calculated temperature is T_3 = 293.4 K with a standard deviation of 0.9 K. 121

FIG. 29. Runs conducted at 600 bar. The calculated temperature is T_3 = 297.0 K with a standard deviation of 0.0 K. 122

FIG. 30. Runs conducted at 20 bar using TIP4P/ice and LB combining rules. The calculated temperature is T_3 = 270.0 K with a standard deviation of 0.0 K. 124

FIG. 31. Runs conducted at 30 bar using TIP4P/ice and LB combining rules. The calculated temperature is T_3 = 270.0 K with a standard deviation of 0.0 K. 125

FIG. 32. Runs conducted at 200 bar using TIP4P/ice and LB combining rules. The calculated temperature is T_3 = 276.1 K with a standard deviation of 0.5 K. 126

FIG. 33. Runs conducted at 400 bar using TIP4P/ice and LB combining rules. The calculated temperature is T_3 = 274.2 K with a standard deviation of 1.6 K. 127

FIG. 34. Runs conducted at 1000 bar using TIP4P/ice and LB combining rules. The calculated temperature is T_3 = 280.1 K with a standard deviation of 1.7 K. 128

FIG. 35. Runs conducted at 20 bar using TIP4P/ice and χ = 1.08 modification. The calculated temperature is T_3 = 279.0 K with a standard deviation of 0.0 K. 129

FIG. 36. Runs conducted at 30 bar using TIP4P/ice and χ = 1.08 modification. The calculated temperature is T_3 = 277.1 K with a standard deviation of 0.5 K. 130

FIG. 37. Runs conducted at 200 bar using TIP4P/ice and χ = 1.08 modification. The calculated temperature is T_3 = 281.5 K with a standard deviation of 0.9 K. 131

FIG. 38. Runs conducted at 400 bar using TIP4P/ice and χ = 1.08 modification. The calculated temperature is T_3 = 283.5 K with a standard deviation of 0.7 K. 132

FIG. 39. Runs conducted at 1000 bar using TIP4P/ice and χ = 1.08 modification. The calculated temperature is T_3 = 287.3 K with a standard deviation of 0.8 K. 133

FIG. 40. Runs conducted at 2000 bar using TIP4P/ice and χ = 1.08 modification. The calculated temperature is T_3 = 289.9 K with a standard deviation of 1.7 K. 134

FIG. 41. Runs conducted at 3000 bar using TIP4P/ice and χ = 1.08 modification. The calculated temperature is T_3 = 290.9 K with a standard deviation of 1.3 K. 135

FIG. 42. Runs conducted at 4000 bar using TIP4P/ice and χ = 1.08 modification. The calculated temperature is T_3 = 289.7 K with a standard deviation of 0.8 K. 136

FIG. 43. Runs conducted at 5000 bar using TIP4P/ice and χ = 1.08 modification. The calculated temperature is T_3 = 288.7 K with a standard deviation of 1.3 K. 137

FIG. 44. Runs conducted at 200 bar using TIP4P/2005 and LB combining rules. The calculated temperature is T_3 = 250.9 K with a standard deviation of 1.8 K. 138

FIG. 45. Runs conducted at 400 bar using TIP4P/2005 and LB combining rules. The calculated temperature is T_3 = 252.5 K with a standard deviation of 1.2 K. 139

FIG. 46. Runs conducted at 1000 bar using TIP4P/2005 and LB combining rules. The calculated temperature is T_3 = 256.1 K with a standard deviation of 1.1 K. 140

FIG. 47. Runs conducted at 200 bar using TIP4P/2005 and χ = 1.115 modification. The calculated temperature is T_3 = 261.2 K with a standard deviation of 1.3 K. 141

FIG. 48. Runs conducted at 400 bar using TIP4P/2005 and χ = 1.115 modification. The calculated temperature is T_3 = 262.5 K with a standard deviation of 0.0 K. 142

FIG. 49. Runs conducted at 1000 bar using TIP4P/2005 and χ = 1.115 modification. The calculated temperature is T_3 = 265.6 K with a standard deviation of 0.5 K. 143

LIST OF TABLES

Page

Table I. The melting temperature of ice, T_m, at 1 bar predicted using the four-point water models TIP4P[99], TIP4P/ice[157], TIP4P/2005[158], and TIP4P-Ew[159] as reported by Fernandez *et al.*[154] and the deviation from the experimental value of each model, ΔT_m.. 43

Table II. Number of molecules in the guest slab for each studied pressure....... 51

Table III. Potential parameters of the TIP4P/Ice (water) [157], TIP4P/2005 (water) [158] and TraPPE (carbon dioxide) [107] models. The distance, in Å, between atoms A and B is denoted d_{AB}. The angle, in degrees, formed at a central atom B separating two A atoms is denoted $\angle A–B–A$. The charge is denoted q. The Lennard-Jones parameters are denoted σ (size parameter) and ε/k_B (energy parameter, with k_B the Boltzmann constant). 55

Table IV. Statistical averaging of 25 simulation runs for the determination of the T_3 at a pressure of 100 bar. The calculated temperature is $T_3 = 282.8$ K with a standard deviation of 3.2 K. The final state of each realization is denoted as (*g*) for hydrate growth or (*d*) for hydrate dissociation.[153] 72

Table V. Experimental and calculated T_3 along with standard deviations, and deviation of predictions from experimental values. Experimental values are taken from the polynomial fit reported by Moridis.[153,170] 73

Table VI. Experimental[2] and calculated three-phase coexistence temperatures (T_3; statistical uncertainty in parenthesis) using the TIP4P/Ice and TIP4P/2005 water forcefields for the cases where cross-interaction parameters are calculated using the LB combining rules (χ = 1.00) and where the modification parameter χ was applied with value optimized with respect to the carbon dioxide solubility in water................. 87

NOMENCLATURE

Latin Letters

$\mathbf{a}$	Acceleration vector
E_k	Kinetic energy [kcal/mol]
$\mathbf{F}$	Force vector
h	Maximum particle displacement
k_B	Boltzmann constant
$\boldsymbol{k}$	Fourier transformed position
k^b	Hooke's constant for bond vibrations
k^θ	Hooke's constant for angle vibrations
L	Box length
L_w	Liquid water phase
m	Mass
N	Number of molecules in simulated system
$\mathbf{P}$	Total system momentum
P	Pressure of simulated system [bar]
$\mathrm{P_C}$	Critical pressure [bar]
q	Charge
$\mathbf{r}$	Position vector [nm]
r	Distance [nm]
t	Time [ns]

T	Temperature of simulated system [K]
T_3	Three-phase coexistence temperature [K]
T_C	Critical temperature [K]
V	Volume of simulated system [nm^3]
$\boldsymbol{v}$	Velocity vector
$V(r)$	Potential energy [kcal/mol]

Greek Letters

α	Width of Gaussian Distribution
γ	Isothermal compressibility of system
ε	Potential well depth
ε_0	Dielectric permittivity of a vacuum
η	Scaling factor
Ξ	Inner Virial term for pairwise additive interactions
ρ	Density
σ	Potential collision diameter
τ	Time constant

Subscripts

0	Equilibrium properties

Abbreviations

C	Carbon dioxide slab
CCS	Carbon Capture and Sequestration
DFT	Density-Functional-Theory
H	Solid hydrate slab
HPCC	High Performance Computing Cluster
M	Supercritical methane slab
MC	Monte Carlo
MD	Molecular Dynamics
NPT	Isobaric-isothermal ensemble
NVT	Canonical ensemble
sH	Structure H hydrate
sI	Structure I hydrate
sII	Structure II hydrate
TSE	Taylor-Series-Expansion
W	Liquid water slab

1. INTRODUCTION

Clathrate hydrates are self-assembling, ice-like, crystalline structures that were discovered in 1810 by Sir Humphry Davy, who observed that a crystalline solid was formed upon cooling of an aqueous solution of chlorine.[1,2] They consist of three-dimensional networks of hydrogen-bonded water molecules encaging low molecular weight "guest" molecules in well-defined polyhedral cavities (or cages). The enclathration of the guest molecules enables hydrate formation since they stabilize the crystal structure. More than 130 guest molecules are known to be hydrate formers including methane, ethane, propane, iso-butane, carbon dioxide, hydrogen sulfide, oxygen, nitrogen, argon and hydrogen.[2] Hydrates are formed under conditions of relatively high pressure and low temperature, in the presence of both water and the guest molecules.

In the early 20th century, the formation of clathrate hydrates was identified as the cause for pipeline and equipment blockages in the gas industry where the conditions of pressure and temperature are suitable for hydrate nucleation and growth.[3] Such blockages pose safety threats and cause large financial losses.[4–6] On the other hand, the fact that the volumetric density of most gases in the hydrate form corresponds to that of a condensed state makes their use for gas storage and transport applications a promising prospect.[7–12] In addition, the differences in thermodynamic and structural stability of hydrates of different guest molecules can be exploited in industrial gas separation for energy[13,14] or environmentally[15–

[17] related processes.[18] Furthermore, hydrate growth results in ion exclusion from the crystal structure, a process that can be used for water purification and desalination.[19,20]

The vast potential applicability of clathrate hydrates has prompted the need for accurate property calculation and prediction, which can be seen by the continuous increase in the number of studies conducted on clathrate hydrates per year.[21] Experimental measurements, modeling at the macroscopic scale using equations of state, and atomistic simulations including both Molecular Dynamics (MD) and Monte Carlo (MC) simulations are different approaches that have been used to provide predictions of hydrate properties. While experimental measurement is the most accurate approach, the financial cost and time associated with measurements of all the possible combinations of guest mixtures that may form hydrates would render the approach impractical.

Therefore, it is necessary to develop theoretical methods that enable efficient prediction of equilibrium and transport properties of hydrate systems. The van der Waals–Platteeuw statistical theory[22] and its variations[23–28] are useful continuum-scale models that have been used for the modelling of hydrate systems. In addition, the use of molecular simulation techniques can provide further insight into the effect of events at the molecular level on the hydrate nucleation, growth, and dissociation processes. They can also be used for the calculation of important thermodynamic and transport properties. If proven accurate, molecular simulation techniques can later be used in the design of new hydrate-related processes, together with the traditional experimental and continuum-scale modelling approaches. This multi-scale approach serves to maximize our understanding of any process.

Due to the relevance of methane and carbon dioxide hydrates to many industrial processes, the accurate estimation of the properties of these hydrates is the topic of many studies, including this work. An outline of the potential applications of these two gas hydrates is provided in the following two sections.

1.1 Applications of Methane Hydrates

The methane hydrate is the most extensively studied clathrate hydrate due to its relevance to some of the most important industrially-relevant problems. The oil and gas industry is greatly interested in methane hydrates from the flow assurance point of view, since the formation of the methane hydrate solid in natural gas pipelines can cause blockages that result in large financial losses and pose significant safety threats.

On the other hand, methane hydrates exist in large quantities in nature, mainly under the oceanic floor and at the permafrost regions.[29] In fact, it has been estimated that approximately 10^{16} kg of methane gas is stored in naturally occurring methane hydrates in oceanic sediments and in continental regions around the globe.[30–33] If this estimate is correct, the amount of methane carbon stored in hydrates is roughly twice the amount of carbon present in all known fossil fuel deposits combined, which makes natural methane hydrates an attractive potential energy source. It is important to note that methane, which constitutes the largest fraction of natural gas, is a less carbon-intensive fuel than coal or oil, producing only half as much carbon dioxide as coal per unit of combustion products.[34–38]

However, the change in global climate that has been brought about with the onset of global warming can cause the decomposition of natural methane hydrates, releasing large volumes of methane into the atmosphere. This would enhance the global warming effect since methane is 21 times more potent than carbon dioxide as a greenhouse gas.[5,39,40] In addition, the occurrence of uncontrolled dissociation of natural methane hydrates can cause geologic hazards such as the collapse of oceanic slopes.[41,42]

1.2 Applications of Carbon Dioxide Hydrates

Carbon dioxide hydrates are of great interest for many industrially-relevant applications. With the ever-increasing need for developing appropriate methods for carbon capture and sequestration (CCS),[43] the hydrate science and technology could offer alternative, viable solutions to both aspects of the capture and storage problem. In particular, the capture of carbon dioxide from flue gases using hydrates has attracted significant attention during the recent years.[15–17]

In section 1.1, the large potential of naturally occurring methane hydrates to act as an energy source was mentioned. However, the difficulty in recovering methane hydrate to use as a fuel arises from the fact that it is in the solid form, which makes it not amenable to conventional oil and gas recovery techniques. This has prompted suggestions of utilizing carbon dioxide gas in the recovery of methane gas from natural methane hydrates. The high concentration of carbon dioxide per unit mass of water, as well as the high thermodynamic stability of carbon dioxide hydrates,[44] enables the substitution of methane stored in methane hydrate sediments by carbon dioxide molecules. This is a favorable process as it provides a means for both retrieving the hydrocarbon and utilizing it in the energy industry, while simultaneously sequestering carbon dioxide gas in the form of carbon dioxide hydrates.[45–48] This idea has been extensively studied using experimental techniques,[49–54] as well as modeling both at the continuum scale[22,55,56] and the microscopic scale using MD[57–63] and Density Functional Theory (DFT)[64] simulation techniques. In addition, carbon dioxide hydrates could find applications in other fields such as for use in fire extinguishers,[65] in the food industry,[66,67] and for biotechnology applications.[68]

1.3 Objectives of Current Study

The main goal of this work is to use the direct phase coexistence methodology[69] for the prediction of the three-phase coexistence line in pure gas hydrate systems using MD simulations. The proposed methodology is tested on two guests; namely, methane and carbon dioxide. The two guests are chosen due to the availability of experimental data which would enable validation of the accuracy of the results, as well as the fact that many of the proposed applications for gas hydrates involve systems that contain these two guests.

2. FUNDAMENTALS OF MD SIMULATIONS

2.1 History and Overview of MD Simulations

Computer simulation techniques are an important development that occurred as early as 1953,[70] and allowed scientists to obtain accurate results for complicated statistical mechanics problems involving many-particle systems. In a molecular simulation, microscopic properties of a system (such as the atomic mass of its constituent molecules or the molecular geometries) are directly translated to macroscopic properties of the system (such as pressure, temperature, or total energy). The simulations can therefore be considered a bridge between experimental results and theoretical predictions, and are often used to provide inputs to macroscopic scale theoretical models. However, it is important to note that the accuracy of the results obtained using molecular simulation techniques is largely dependent on our imperfect knowledge of the molecular properties of the system. It is therefore essential to prove the validity of the models used by comparison of the results of molecular simulations with experimental data.[71]

The MD simulation technique in particular involves the solution of the classical equations of motion for a set of molecules. The inception of this technique dates back to 1957 in the pioneering work of Alder and Wainwright, who calculated the equilibrium properties of a system consisting of 32 hard spheres in a rectangular box.[72] With the ever-increasing computational power that has been achieved since, many developments were made that increased the accuracy and speed of the techniques, allowing for the simulation of larger, more complex systems such as the simulation of many-particle systems that interact via the Lennard-Jones potential in the 1960's.[73–75] Today, with the advent of High Performance Computing Clusters (HPCC), it has become possible to perform MD simulations on multiphase systems that consist of thousands of molecules, which allows the computation of many properties including thermodynamic properties (such as solubility, density, coexistence temperatures, interfacial tension and enthalpy), transport properties (such as diffusion coefficient and viscosity), and kinetic rates (such as the rate of solid formation or dissociation). The simulations are typically over length scales of several nanometers and time scales of nanoseconds to a few microseconds.

The MD simulation technique involves the calculation of the trajectory in space and time of a system consisting of a defined number of particles. This is done through the integration with respect to time *t* of Eqn. (1), which is Newton's second law:

$$\mathbf{F}_i = m_i \mathbf{a}_i = m_i \frac{\partial^2 \mathbf{r}_i}{\partial t^2} \tag{1}$$

where $\mathbf{F}_i$ is the force exerted on a particle i, $\mathbf{r}_i$ is the particle's position vector, m_i is the particle's mass, and $\mathbf{a}_i$ is the acceleration vector of the particle. The force on each particle is defined as the first derivative of the potential energy, $V(r)$, with respect to the particle's position, as shown in Eqn. (2):[76]

$$\mathbf{F}_i = -\frac{\partial V(r)}{\partial \mathbf{r}_i} \qquad (2)$$

By defining the initial velocities and positions of the particles, the equations can be integrated to provide the time evolution of the system. In order to accomplish this, the potential energy of each particle as a function of the position of all the other particles in the system must be known. This function is specific for every type of molecule in the simulation and is known as the force field. It provides a means for calculating both the intermolecular (non-bonded) and intramolecular (bonded) interactions between particles.

The overall algorithm used in a MD simulation is provided in Fig. 1.[77] First, appropriate force fields are selected for the constituent molecules of the system under consideration. The system is setup with particular considerations that increase the accuracy and efficiency of the simulations. This is described in section 2.2. Then, the total potential energy of the system is calculated using the methods provided in section 2.3. The equations of motion are integrated over a defined time step to find the new position of each particle in the system. The most common integration algorithm used, and the one implemented in this work, is the “Leap-Frog” algorithm. This algorithm is described in section 2.4. The integration is repeated until the total, pre-defined simulation time is reached.

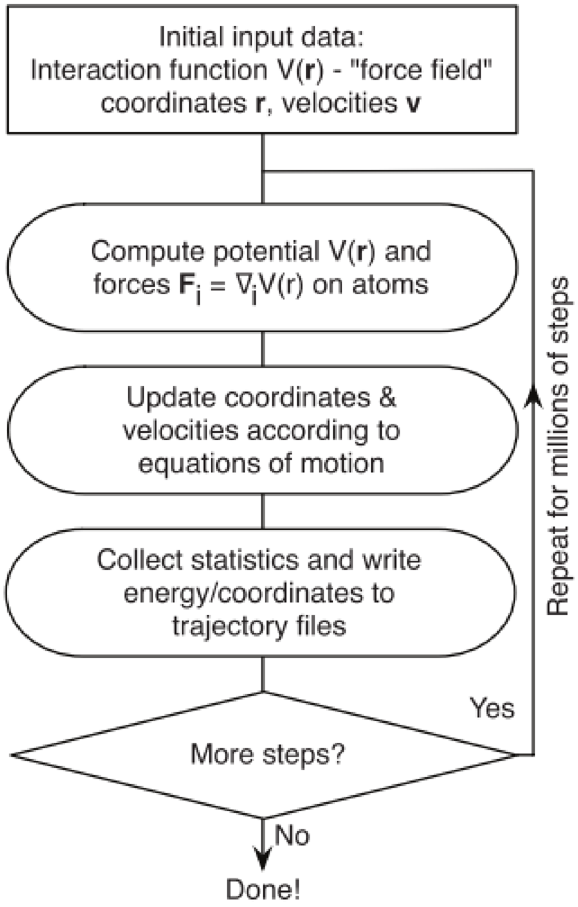
Initial input data:
Interaction function V(r) - "force field"
coordinates r, velocities v
Compute potential V(r) and
forces F_i = ∇_iV(r) on atoms
Update coordinates &
velocities according to
equations of motion
Collect statistics and write
energy/coordinates to
trajectory files
More steps?
Yes
No
Done!
Repeat for millions of steps

FIG. 1. MD simulation algorithm.[77]

Finally, the recorded trajectory is studied both qualitatively by observation of the system evolution, and quantitatively by calculating the properties of interest to the problem under consideration. The method used for the calculation of these properties depends on the molecular ensemble implemented in the simulation, which is the set of fixed macroscopic parameters that define the phase space through which the system evolves. For example, in the canonical ensemble (NVT), the total number of molecules N, the total volume V, and the temperature T of the system are kept constant throughout the simulation. In this work, the isobaric-isothermal (NPT) ensemble was used. A description of this ensemble and the methods used to fix the pressure and temperature throughout the simulation is provided in section 2.5.

2.2 System Setup

2.2.1 Initial Particle Positions and Velocities

The purpose of the simulation is to replicate the properties of the real system as closely as possible. For this reason, the initial system must be constructed in a manner that mimics the real system being simulated as closely as possible. First, all the particles of the system must be placed at specific positions in a box of known dimensions. In assigning these positions, the known properties of the system must be carefully incorporated. For example, if the system being studied is pure water at 298 K and 1 bar, the box should be constructed such that the density of the system is around 1000 kg/m^3.

Each particle is also assigned an initial velocity. The average velocity, $\langle v^2 \rangle$, is directly related to the average kinetic energy of the system, $\langle E_k \rangle$, according to Eqn. (3):

$$\langle E_k \rangle = \frac{1}{2} m \langle v^2 \rangle = \frac{3kT}{2} \tag{3}$$

where m is the mass of each particle, T is the system temperature, and k is Boltzmann’s constant.

If a generating temperature is specified, the above equation can be solved for a system of particles of known mass to find the average velocity. Each particle can then be given a random initial velocity from a Gaussian distribution, which is shown in Eqn. (4):

$$\rho(v_{i\alpha}) = \sqrt{\left(\frac{m}{2\pi kT}\right)} e^{-\frac{m v_{i\alpha}^2}{2kT}} \tag{4}$$

where $\rho(v_{i\alpha})$ is the probability density for the velocity $v_{i\alpha}$ of particle i in the direction α.[78,79]

Random number generators are used in order to assign velocities to each particle in the system such that the velocity distribution obeys the function above. This is particularly useful, since a different random number would result in a different initial velocity assigned to each particle while maintaining the same initial positions, potential energy, and average kinetic energy. Each simulation would then proceed by a different trajectory through the phase space. Hence, it is possible to run multiple, independent simulations at the same conditions and obtain an estimate of the error in the measurement of any property of interest.[71]

A further requirement in the initialization of the velocity of each particle is that the total momentum of the system is zero, as shown in Eqn. (5):

$$\boldsymbol{P} = \sum_{i=1}^{N} m_i \boldsymbol{v}_i = 0 \tag{5}$$

where $\boldsymbol{P}$ is the (3×1) vector of the resultant momentum in each direction, and $\boldsymbol{v}_i$ is the $3N$ velocity vector for all particles. In order to accomplish this, the initially assigned velocities are scaled such that the condition of zero momentum is satisfied.

2.2.2 *Energy Minimization*

In addition to creating a box with realistic properties, it is important that none of the molecules placed inside the lattice are overlapping. As will be discussed in section 2.3, the intermolecular potential energy between any two atoms tends to infinity if the two atoms are overlapping. The presence of such high potential energy will result in excessively large forces causing the MD simulation to fail. In order to avoid this, an energy minimization algorithm is needed, which removes any particle overlaps before starting the simulation.

The purpose of the energy minimization algorithm is not to find the particle coordinates that correspond to the one global minimum in the potential energy hypersurface, since the potential energy function is a very complex landscape with many dimensions making it extremely difficult to locate this. However, starting from an initial configuration, it is possible to locate the nearest local potential energy minimum. Many energy minimization algorithms exist that accomplish this. The algorithm used in this work is the so-called “steepest descent” algorithm. While this is not the most efficient algorithm that exists for performing the search, it is commonly used due to its robustness and ease of implementation.

In the steepest descent method, the particles in the system are moved in an iterative manner such that the new positions exhibit a lower energy than the previous step, until a controlling criterion is met. The first step is to compute the force acting on each particle in the initial configuration as the negative derivative with respect to position of the potential energy, as described by Eqn. (2). Also, a maximum displacement for each particle, h_0 is defined by the user, and is needed in order to ensure that the particles are not displaced by very large distances, distorting the initial, user-defined configuration. The new positions of the particles are then calculated using Eqn. (6):

$$\boldsymbol{r}_{n+1} = \boldsymbol{r}_n + \frac{\boldsymbol{F}_n}{\max\left(\left|\boldsymbol{F}_n\right|\right)} h_n \tag{6}$$

where $\boldsymbol{r}_n$ is the $3N$ vector of the three coordinates of each of the N particles in the system at step n, $\boldsymbol{F}_n$ is the $3N$ vector of the forces acting on each particle, and $\max(|\boldsymbol{F}_n|)$ is the largest of the absolute values of the force components.

When the positions are updated, the new potential energy is calculated. If the potential energy for the new position vector is less than the previous step, the new positions are accepted. Also, a larger step size can be used to increase the efficiency of the descent in the potential energy. If the new potential energy is greater than the previous step, the new positions are rejected, and the step size is decreased. These criteria are presented in Eqn. (7):

$$\begin{aligned} &\text{if } V_{n+1} < V_n \Rightarrow \text{set } \boldsymbol{r}_n = \boldsymbol{r}_{n+1} \text{ and } h_{n+1} = 1.2h_n \\ &\text{if } V_{n+1} \geq V_n \Rightarrow \text{reject } \boldsymbol{r}_{n+1} \text{ and set } h_{n+1} = 0.2h_n \end{aligned} \tag{7}$$

The algorithm is terminated either after a certain number of pre-defined steps is completed, or when $\max(|\boldsymbol{F}_n|)$ is smaller than a specified tolerance.

2.2.3 *Periodic Boundary Conditions*

While the interest from most molecular simulations is to estimate bulk properties, the use of several thousand molecules in a box would mean that most molecules are at the box surface. The forces experienced by a molecule near a wall are significantly different from those experienced by a molecule within the bulk. Ideally, one would like to simulate a very large number of molecules such that a sufficient volume is a large distance away from the walls and can be used to represent the bulk. However, due to the limited storage and computational power of even the best computer systems, this is not possible. For this reason, the concept of periodic boundary conditions has been developed to overcome the problem of surface effects.[79]

A schematic representation of periodic boundary conditions is provided in Fig. 2.[71] When periodic boundary conditions are applied, the original box prepared is considered one cell that lies within a periodic lattice which consists of an infinite number of replicas of the same box. If a particle i leaves the box at position $\left({}^{L}\!/_{2}, y_1, z_1\right)$, where L is the length of the box in the x-dimension and the box Center is placed at the origin $(0,0,0)$, it re-enters the box at position $\left(-{}^{L}\!/_{2}, y_1, z_1\right)$. In this way, any particle found within the box can be considered part of a bulk system, and properties measured from simulation are directly comparable to experimental bulk property measurements.

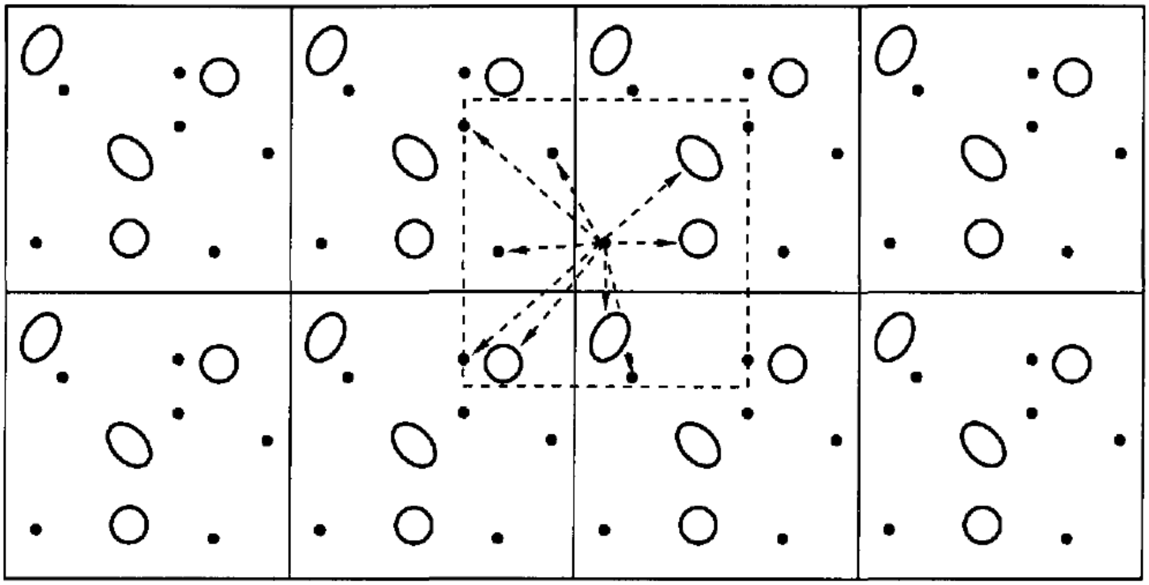

FIG. 2. A schematic representation of periodic boundary conditions.[71]

However, since the heart of a MD simulation is the calculation of the potential energy, and therefore the force exerted on each particle, the problem arises for an infinite, periodic system that there is an infinite number of interactions to calculate for each particle. Since this is not possible, the non-bonded interactions calculated using the methods presented in section 2.3.2 are truncated after a certain cutoff distance, r_C. This is appropriate since the short-range interactions are much stronger than the long-range interactions. Methods exist for the calculation of the errors that arise from truncating the potential energy at a short distance, and making corrections accordingly. These will be discussed in the next section.

The choice of r_C is critical in the accuracy of the potential energy calculation. A very small value of r_C would minimize the number of interactions accounted for, reducing the accuracy of the calculation. However, using a large value of r_C (greater than $L/2$, where L is the shortest box dimension) would increase the cost of the calculation, and will give the possibility for explicitly calculating the interaction between two molecules i and j twice; once between the two molecules in the same box, and once between molecule i from one box and the nearest periodic image of molecule j. If the interaction between any two molecules should be explicitly accounted for only once for computational efficiency, r_C should be chosen such that it does not exceed $L/2$.

The algorithms used for the identification of the pairs can then identify the minimum distance between any central molecule and any of the other molecules. This is known as the “minimum image convention”, and is illustrated by the dotted box in Fig. 2. It is used for predominantly short-range interactions, such as dispersion forces. This method is not appropriate for long-range interactions where explicitly accounting for pairs that are far apart is essential for accuracy of the calculations. This is the case for electrostatic (or coulombic) interactions, and efficient methods exist for specifically accounting for interactions of this nature, as discussed in section 2.3.2.

2.3 The Potential Energy Function

The force field chosen to describe a molecule provides a method for the calculation of the intramolecular (bonded) interactions and the intermolecular (non-bonded) interactions. Intramolecular parameters include the molecular geometry and the contributions to the potential energy of the molecule that come from the interactions between the atoms that make up the molecule. This includes bond length and bond angle fluctuations, and torsional vibrations. Intermolecular interactions are those between atoms in the same molecule that are several atoms apart, and between atoms in different molecules. These include dispersion (van der Waals) and electrostatic (Coulombic) interactions. The total potential energy of the system is calculated as a sum of all the intramolecular and intermolecular potential energy contributions from all the particles in the system, as shown in Eqn. (8):

$$\begin{aligned} V(r) &= \left\{ V_b\left(\mathbf{r}_i,\ldots,\mathbf{r}_N\right) \right\} + \left\{ V_{nb}\left(\mathbf{r}_i,\ldots,\mathbf{r}_N\right) \right\} \\ &= \left\{ \sum_{molecules} \left[\sum_{i,j\in bonds} V_{ij}\left(\mathbf{r}_i,\mathbf{r}_j\right) + \sum_{i,j,k\in angles} V_{ijk}\left(\mathbf{r}_i,\mathbf{r}_j,\mathbf{r}_k\right) + \sum_{i,j,k,l\in torsions} V_{ijkl}\left(\mathbf{r}_i,\mathbf{r}_j,\mathbf{r}_k,\mathbf{r}_l\right) \right] \right\} + \\ &\quad \left\{ \sum_{i<j\in pairs} \left[V_{ij,\,\mathrm{VdW}}\left(r_{ij}\right) + V_{ij,\,\mathrm{electrostatic}}\left(r_{ij}\right) \right] \right\} \end{aligned} \tag{8}$$

where V_b is the total bonded interaction potential energy and V_{nb} is the total non-bonded interaction potential energy.

The methods by which the potential energy contributions in Eqn. (8) are calculated are explained in the following sections.

2.3.1 Bonded Parameters

The first and major intramolecular parameter that must be explicitly described by the force field is the molecular geometry. This is extremely crucial, and always has a very significant effect on the outcomes of the simulation. Molecular geometries are often simplifications of the physical reality, wherein the molecule is treated as a rigid or semi-rigid unit, with fixed bond lengths, bond angles, and torsional angles. This assumption is made possible by the fact that bond vibrations are of very high frequency, making them very difficult to account for in classical simulations, and low amplitude, making them relatively unimportant for many liquid properties. Thus, molecules are commonly represented as a collection of several sites, each with mass, charge, or both. In order to develop the models, a general molecular geometry is first predicted in a manner that resembles the known molecular geometry. The distance and angles between the sites, as well as the appropriate charge on each site are then found by trial-and-error, such that the final model accurately predicts some experimental properties of interest (such as fluid density or saturation conditions). As such, models that are often built for the replication of certain experimental data in a certain range of pressure and temperature may not always accurately predict other experimental data that were not accounted for in the fitting. For this reason, for most common molecules many different models have been proposed, each developed to predict certain target properties very accurately.[79]

In some cases, the modeling of the bonded vibrations is necessary to achieve accuracy in the calculation of particular properties. For MD simulations, it is often sufficient to approximate the bond and angle vibrations as harmonic oscillations about an equilibrium bond length or bond angle, respectively. Hooke’s law is often used for this purpose, as shown in Eqn. (9) for bond length vibrations, and Eqn. (10) for bond angle vibrations:

$$\sum_{i,j\in bonds} V_{ij}\left(\mathbf{r}_i,\mathbf{r}_j\right) = \sum_{i,j\in bonds} \frac{1}{2} k_{ij}^{b}(r_{ij} - r_{ij}^{0})^2 \tag{9}$$

$$\sum_{i,j,k\in angles} V_{ijk}\left(\mathbf{r}_i,\mathbf{r}_j,\mathbf{r}_k\right) = \sum_{i,j,k\in angles} \frac{1}{2} k_{ijk}^{\theta}(\theta_{ijk} - \theta_{ijk}^{0})^2 \tag{10}$$

where k_{ij}^{b} and k_{ijk}^{θ} are Hooke's constants for the bond and angle vibrations, respectively, r_{ij}^{0} and θ_{ijk}^{0} are the equilibrium bond length and angle, respectively, and r_{ij} and r_{ijk} are the instantaneous bond length and angle respectively. Hooke's constants and the equilibrium bond length and angle are adjustable parameters that are fitted to maximize the accuracy of the model in predicting certain spectroscopic data.

2.3.2 Non-Bonded Parameters

For a system of N particles, the true, total non-bonded interaction potential energy is the sum of the contributions from all the possible particle pairs (v_2), triplets (v_3), and higher order multiplets, plus the potential energy associated with any external forces (such as a gravitational field) acting on each particle within the system (v_1), as shown in Eqn. (11).[79]

$$V_{nb}\left(\mathbf{r}_i,\ldots,\mathbf{r}_N\right) = \sum_{i} v_1(\mathbf{r}_i) + \sum_{i}\sum_{j>i} v_2(\mathbf{r}_i,\mathbf{r}_j) + \sum_{i}\sum_{j>i}\sum_{k>j} v_3(\mathbf{r}_i,\mathbf{r}_j,\mathbf{r}_k) + \ldots \tag{11}$$

Several simplifications are often made in computer simulations in order to increase the calculation speed and efficiency. First, it is important to note that two-body interactions have the most significant contribution towards the total potential energy. While triplets and higher order multiplets can also have a significant contribution to the total potential energy, especially for dense systems, the identification of all high-order multiplets within any system, and the evaluation of the many-body potential energy functions is very computationally expensive. For this reason, “effective” two-body potentials are usually used with fitted parameters that incorporate the effects from three-body and higher order interactions. Since the contribution from the different multiplets is often a function of density but the parameters for the effective two-body potential models are not, the models may not be very accurate in predicting all the properties at all conditions.

This results in many models for each component, each performing very well for certain properties. For an appreciation of the variety of models available for different molecules, the reader should refer to section 3.2.1, where some of the available models for water, methane, and carbon dioxide are outlined.

In the next two sections, the specific treatment of dispersion and electrostatic interactions is described.

2.3.2.1 Dispersion Interactions

Several known potential energy functions can be used for the calculation of intermolecular dispersion interaction potential energies, such as the Lennard-Jones or Kihara potentials. The most commonly used is the Lennard-Jones (12,6) pair potential, given by Equation (12):

$$V_{ij,\mathrm{dispersion}}(r_{ij}) = 4\varepsilon_{ij}\left[\left(\frac{\sigma_{ij}}{r_{ij}}\right)^{12} - \left(\frac{\sigma_{ij}}{r_{ij}}\right)^{6}\right] \tag{12}$$

The function relates the potential energy between two particles i and j to their separation distance r_{ij} using two parameters: an energy parameter ε_{ij} that gives the minimum energy corresponding to equilibrium separation, and a size parameter σ_{ij} that is equal to the distance between the particles where the potential energy is zero. The function is plotted in Fig. 3.[76]

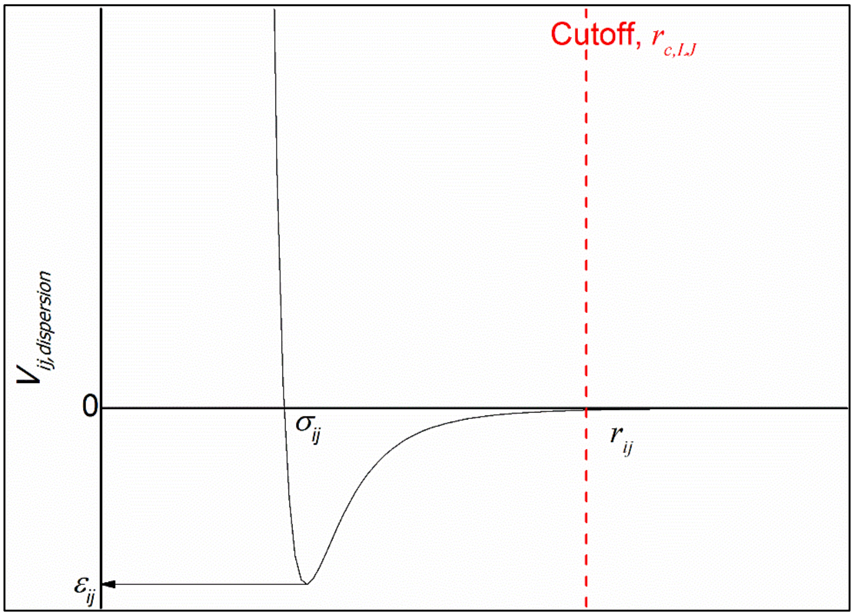

FIG. 3. Lennard-Jones (12-6) potential.[76] The red, dashed line illustrates the concept of truncation beyond a cutoff length, $r_{c,LJ}$.

As was mentioned in section 2.2.3, due to the use of periodic boundary conditions to model an artificially infinite system, the potential energy must be truncated at a certain, user-defined cutoff length $r_{c,LJ}$. The value of $r_{c,LJ}$ is typically chosen to be at least $2.5\sigma_{ij}$,[79] which is the separation distance beyond which the attractive potential typically drops to around $\frac{1}{60}\varepsilon_{ij}$ (see red line in Fig. 3). While this may seem very small, assuming that the potential energy is zero beyond this point can sometimes lead to a systematic error in the calculation of the total dispersion potential. In addition, this assumption results in a discontinuity in the potential energy that may cause issues when calculating the first derivative of the potential energy for computation of the forces. For this reason, it is often necessary to estimate the magnitude of error in the dispersion tail. The error can be accounted for by estimating and adding the tail correction to the truncated potential, as shown in Eqn. (13):

$$V_{dispersion}^{tot} = \sum_{i,j>i} V_{ij,\mathrm{dispersion}}^{C}\left(r_{ij}\right) + \frac{N\rho}{2}\int_{r_C}^{\infty} 4\pi r^2 V_{ij,\mathrm{dispersion}}\left(r\right)\mathrm{g}\left(r\right)\mathrm{d}r \qquad (13)$$

In this equation, $V_{ij,\mathrm{dispersion}}^{C}\left(r_{ij}\right)$ is the function used for the calculation of the dispersion potential [such as Eqn. (12)] where the maximum distance between two particles is $r_{c,LJ}$, ρ is the average number density, $V_{ij,\mathrm{dispersion}}\left(r_{ij}\right)$ is the potential energy function, and $g(r)$ is the radial distribution function. The full derivation of Eqn. (13) is provided in references 71 and 79.

For homogeneous systems, it can be assumed that $g(r)$ is 1 beyond the cutoff distance, which significantly simplifies the calculation of the integral in Eqn. (13). Making this assumption and correcting for the long range dispersions using Eqn. (13) is therefore the most frequently used approach in MD simulations.

2.3.2.2 Electrostatic Interactions

The total electrostatic intermolecular interaction potential energy is a function of the separation distance between every particle pair, and the charges, q, of each of the two particles. This is given in Equation (14):[76]

$$V_{ij,\mathrm{electrostatic}} = \sum_{i,j>i} \frac{q_i q_j e^2}{4\pi\varepsilon_0 r_{ij}} \tag{14}$$

where e is the electronic charge and ε_0 is the dielectric permittivity of a vacuum.

Evaluation of the function within the sum in Eqn. (14) would give the specific interaction between two charged particles i and j, and is positive if both particles have the same sign (repulsion), and negative if the two particles have different signs (attraction).

While the decay of dispersion forces is proportional to $1/r^6$ [Eqn. (12)], decay of the electrostatic interactions is proportional to $1/r$, making these interactions much stronger at longer distances than the dispersion interactions. For this reason, using a mean-field approach to account for the long-range electrostatic interactions such as that used for dispersion interactions [Eqn. (13)] will not yield an accurate solution. Therefore, in systems where charged particles exist, accounting explicitly for particle pairs that are far apart is necessary to achieve accuracy.

The most commonly used method to account for the long-range electrostatic interactions is known as the Ewald summation.[80] A detailed description of the Ewald summation method can be found in references 71 and

79. As an overview, the method separates the electrostatic potential into two parts: a short-range part and a long-range part. The short-range part consists of all the particle pairs that have a separation distance below the user-defined cutoff for the electrostatic potential, $r_{c,\mathrm{electrostatic}}$. In the short-range, the summation is performed in a similar manner as that used for calculation of short-range dispersion forces, wherein the particle pairs are identified and the electrostatic interaction potential between any two particles is calculated using Eqn. (14). At further separation distances, the charges are mathematically treated by performing a Fourier transformation that represents all the charges that exist in $\boldsymbol{n}$ images of the unit cell as a Gaussian charge distribution, where $\boldsymbol{n}$ is defined by the user and is usually between 5 and 7 images in each direction.

The final equation for calculating the total electrostatic potential energy for a cubic unit cell is provided in Eqn. (15), where V is the unit cell volume, $\rho(\mathbf{k})$ is the charge distribution defined by Eqn. (16) as a function of the Fourier transformed position $\mathbf{k}$, and α is the width of the Gaussian distribution.

$$\begin{aligned} V_{\mathrm{electrostatic}} = & \frac{1}{2V}\sum_{k\neq 0}\frac{4\pi}{k^2}\left|\rho(\mathbf{k})\right|^2 \exp\left(-k^2/4\alpha\right) \\ & -(\alpha/\pi)^{\frac{1}{2}}\sum_{i=1}^{N} q_i^{\,2} \\ & +\frac{1}{2}\sum_{i\neq j}^{N}\frac{q_i q_j \operatorname{erfc}\left(\sqrt{\alpha}\, r_{ij}\right)}{r_{ij}} \end{aligned} \tag{15}$$

where $$\rho(\mathbf{k}) \equiv \sum_{i=1}^{N} q_i \exp\left(\mathrm{i}\mathbf{k}\cdot r_i\right) \tag{16}$$

The first summation in the right-hand-side of Eqn. (15) is the total long-range electrostatic interactions including the interaction of any particle i with itself, the second term is the subtraction of the self-interaction contribution, and the third term is the total short-range interaction potential energy obtained by generalizing Eqn. (14).

2.4 Leap-Frog Integration

Once the intermolecular potential energy has been evaluated for a given configuration, the MD simulation proceeds by integration of Newton's equations of motion [Eqns. (1) and (2)] to find the new positions of all particles at time $t + \Delta t$, where Δt is a user-defined time step. The chosen algorithm for performing the numerical integration should ideally preserve energy over short and long times, and should be efficient such that the simulation speed is not hindered. In addition, the use of large time steps greatly improves the simulation speed, so the chosen algorithm should allow for the use of large time steps without loss of accuracy.

Among the most commonly used algorithms for the integration are the Verlet[81] and Leap-Frog[82] algorithms. Both these algorithms yield identical trajectories but different velocities at each time step. The Leap-Frog algorithm is the default integrator in the MD simulation package Gromacs,[83–85] and is the algorithm used in this work. In order to derive the position, $\boldsymbol{r}(t + \Delta t)$**,** for all particles at time $t + \Delta t$, a Taylor series expansion (TSE) of the coordinates at the updated time step is performed around time t, as shown in Eqn. (17):

$$\begin{aligned}\mathbf{r}(t+\Delta t) &= \mathbf{r}(t)+\frac{\mathbf{r}'(t)}{1!}\Delta t+\frac{\mathbf{r}''(t)}{2!}\Delta t^2+\frac{\mathbf{r}'''(t)}{3!}\Delta t^3+f\left(\Delta t^4\right)\\ &= \mathbf{r}(t)+\mathbf{v}(t)\Delta t+\frac{\mathbf{F}(t)}{2m}\Delta t^2+\frac{\mathbf{r}'''(t)}{3!}\Delta t^3+f\left(\Delta t^4\right)\end{aligned} \tag{17}$$

where $\boldsymbol{v}(t)$ is the velocity vector for all particles at time t, $\mathbf{F}(t)$ is the force on all particles at time t, m is the mass of each particle, and $\mathbf{r}'(t)$, $\mathbf{r}''(t)$, and $\mathbf{r}'''(t)$ are the first, second, and third derivatives of the position with respect to time, respectively. Similarly, a TSE of the coordinates at the previous time step $t - \Delta t$ yields Eqn. (18):

$$\mathbf{r}(t-\Delta t)=\mathbf{r}(t)-\mathbf{v}(t)\Delta t+\frac{\mathbf{F}(t)}{2m}\Delta t^2-\frac{\mathbf{r}'''(t)}{3!}\Delta t^3+f\left(\Delta t^4\right) \tag{18}$$

By summing Eqns. (17) and (18), and solving for $\mathbf{r}(t + \Delta t)$**,** we obtain the estimate for the new position given by Eqn. (19). This estimate has an error of order Δt^4.

$$\mathbf{r}(t+\Delta t)\approx 2\mathbf{r}(t)-\mathbf{r}(t-\Delta t)+\frac{\mathbf{F}(t)}{m}\Delta t^2 \tag{19}$$

In the Leap-Frog algorithm, the velocity at half a time step before a time t is approximated as the derivative of the straight line connecting the positions at time $t - \Delta t$ and t, as shown in Eqn. (20). The same approach is used to approximate the velocity half a time step after a time t, as shown in Eqn. (21).

$$\mathbf{v}\left(t-{\Delta t}/{2}\right)=\frac{\mathbf{r}(t)-\mathbf{r}(t-\Delta t)}{\Delta t} \tag{20}$$

$$\mathbf{v}\left(t+{\Delta t}/{2}\right)=\frac{\mathbf{r}(t+\Delta t)-\mathbf{r}(t)}{\Delta t} \tag{21}$$

By solving Eqn. (21) for $\boldsymbol{r}(t+\Delta t)$, and equating this to the right-hand of Eqn. (19) we obtain an expression for updating the velocity at time $t+\Delta t/2$, as shown in Eqn. (22).

$$\mathbf{v}\left(t+\Delta t/2\right)=\mathbf{v}\left(t-\Delta t/2\right)+\frac{\mathbf{F}(t)}{m}\Delta t \tag{22}$$

It can be seen from Eqns. (19) and (22) that the position vector at time $t-\Delta t$ and the velocity vector at time $t-\Delta t/2$ are needed in order to continue the simulation. At the beginning of the simulation, only an estimate for the position the previous time is needed, and is obtained simply by subtracting the product of the initial velocity (obtained using the method described in section 2.2.1) and the time step from the initial position, as shown in Eqn. (23).[71]

$$\mathbf{r}(-\Delta t)=\mathbf{r}(0)-\mathbf{v}(0)\Delta t \tag{23}$$

2.5 MD Simulations in the NPT Ensemble

In the preceding discussion, the algorithms discussed do not cause any modifications to the box volume, and maintain a constant average kinetic energy since the system is closed and no energy exchange between the box contents and any outside body occurs. Essentially, simulations performed using only the algorithms previously described proceed in the microcanonical ensemble [constant number of molecules, volume, and energy (NVE)]. However, in macroscopic laboratory experiments, the controlled variables are often the pressure and temperature, which makes it advantageous to be able to conduct MD simulations in the NPT ensemble. Control of the temperature and pressure of the simulated system in a MD simulation can be achieved by making use of artificial thermostats and barostats.

Before describing the methods used to control the temperature and pressure of any simulated system, these state variables must first be defined in the context of the known parameters within the simulation box. Eqn. (3) (section 2.2.1) provides the direct relationship between the kinetic energy of the system and the temperature of the system. This equation is used to define the temperature of the simulation. Thus, the temperature is a direct result of the average velocity, and increasing or decreasing the velocity of the particles will directly result in an increase or decrease in the temperature, respectively. The difference between the various existing algorithms for thermostats is the method by which the velocity is modified in order to achieve the desired temperature.

In a simulation, the pressure P is defined according to the Virial theorem using Eqn. (24).[71]

$$P = \frac{2}{3V}\left(E_k - \Xi\right) \tag{24}$$

where E_k is the total kinetic energy, V is the box volume, and Ξ is the inner Virial term for pairwise additive interactions, defined in Eqn. (25).

$$\Xi = \frac{1}{2}\sum_{i<j}\mathbf{r}_{ij}\cdot\mathbf{F}\left(\mathbf{r}_{ij}\right) \tag{25}$$

The first term of Eqn. (24) is a result of the kinetic energy, while the second term is a result of the potential energy that arises from particle interactions. As can be seen from Eqn. (24), an increase or decrease in the box volume results in a decrease or increase in the pressure, respectively. Therefore, control of the pressure in a simulation can be achieved by modifying the volume of the box. As was the case for the thermostat, the difference between the various existing barostats is the method by which the volume is modified to achieve the desired pressure.

In this work, the so-called Berendsen coupling scheme has been implemented to achieve pressure and temperature control.[86] The methodology for controlling the temperature involves coupling the system to a bath at the set-point temperature, T_{MD}, which “mathematically” exchanges energy with the contents of the simulation box in order to adjust the velocity of the particles to achieve the required temperature set-point. The temperature is modified according to Eqn. (26):

$$\frac{dT(t)}{dt}=\frac{T_{MD}-T(t)}{\tau_T} \tag{26}$$

where $T(t)$ is the instantaneous temperature at time t, and τ_T is the thermostat time-constant that describes how strongly the system is coupled with the temperature bath. Larger values of τ means the system is not very strongly coupled with the temperature bath such that the change in the velocity of all particles is not very violent. From the Berendsen thermostat the rate of change of the velocity of each particle, $\frac{dv(t)}{dt}$ is described by Eqn. (27).

$$\frac{d\mathbf{v}(t)}{dt}=\frac{\mathbf{F}(t)}{m}+\frac{1}{2\tau_T}\left(\frac{T_{MD}}{T(t)}-1\right)\mathbf{v}(t) \tag{27}$$

Similar to the Berendsen temperature coupling scheme, pressure control is achieved in the Berendsen barostat by coupling the system to a “pressure bath”. The coordinates and box dimensions are scaled at every time step to achieve the desired pressure, P_{MD}, according to Eqn. (28):[86]

$$\frac{dP(t)}{dt} = \frac{P_{MD} - P(t)}{\tau_P} \tag{28}$$

where $P(t)$ is the instantaneous pressure at time t, and τ_P is the barostat time-constant that has the same role in the barostat as τ_T has in the thermostat. For isotropic pressure coupling, where changes in the box dimensions are made equivalently in all directions, the scaling factor, $\eta(t)$, is given by Eqn. (29):

$$\eta(t) = 1 - \frac{\Delta t}{\tau_P}\gamma\left(P_{MD} - P(t)\right) \tag{29}$$

where γ is the isothermal compressibility of the system. In this form, the volume is scaled by η and the coordinates of each particle and cell dimensions are scaled by $\eta^{1/3}$. Anisotropic pressure coupling can also be achieved where each direction is set to have a different compressibility, and a separate pressure bath is coupled to each of the three dimensions. This type of pressure coupling can result in simulation artifacts, but can be more appropriate for non-homogeneous or non-isotropic systems.

3. CLATHRATE HYDRATES LITERATURE REVIEW

In this section, an outline of the structures of clathrate hydrates and their three-phase equilibrium is first provided in section 3.1, with particular attention to methane and carbon dioxide hydrates. Second, a review of the MD simulation work that has been conducted on methane and carbon dioxide hydrates is presented in section 3.2. This involves a discussion of the models available for describing water, methane and carbon dioxide in molecular simulations in section 3.2.1, followed by a description of the procedures used by various authors to predict the three-phase coexistence of methane and carbon dioxide hydrates in section 3.2.2.

3.1 Hydrate Crystal Structures and Phase Equilibrium

The three-dimensional, hydrogen-bonded network of water molecules in a hydrate crystal is similar to that found in ice, with the main difference being the presence of a guest molecule in the cages of hydrates to stabilize the structure. The specific hydrate structure that forms is determined by the size of the guest molecule, as well as its interactions with water. The three most common hydrate crystal structures are cubic structure I (sI), cubic structure II (sII), and a hexagonal structure H (sH), which are illustrated in Fig. 4.[87] The structures differ in the number and size of the cavities that make a single unit cell of the crystal.

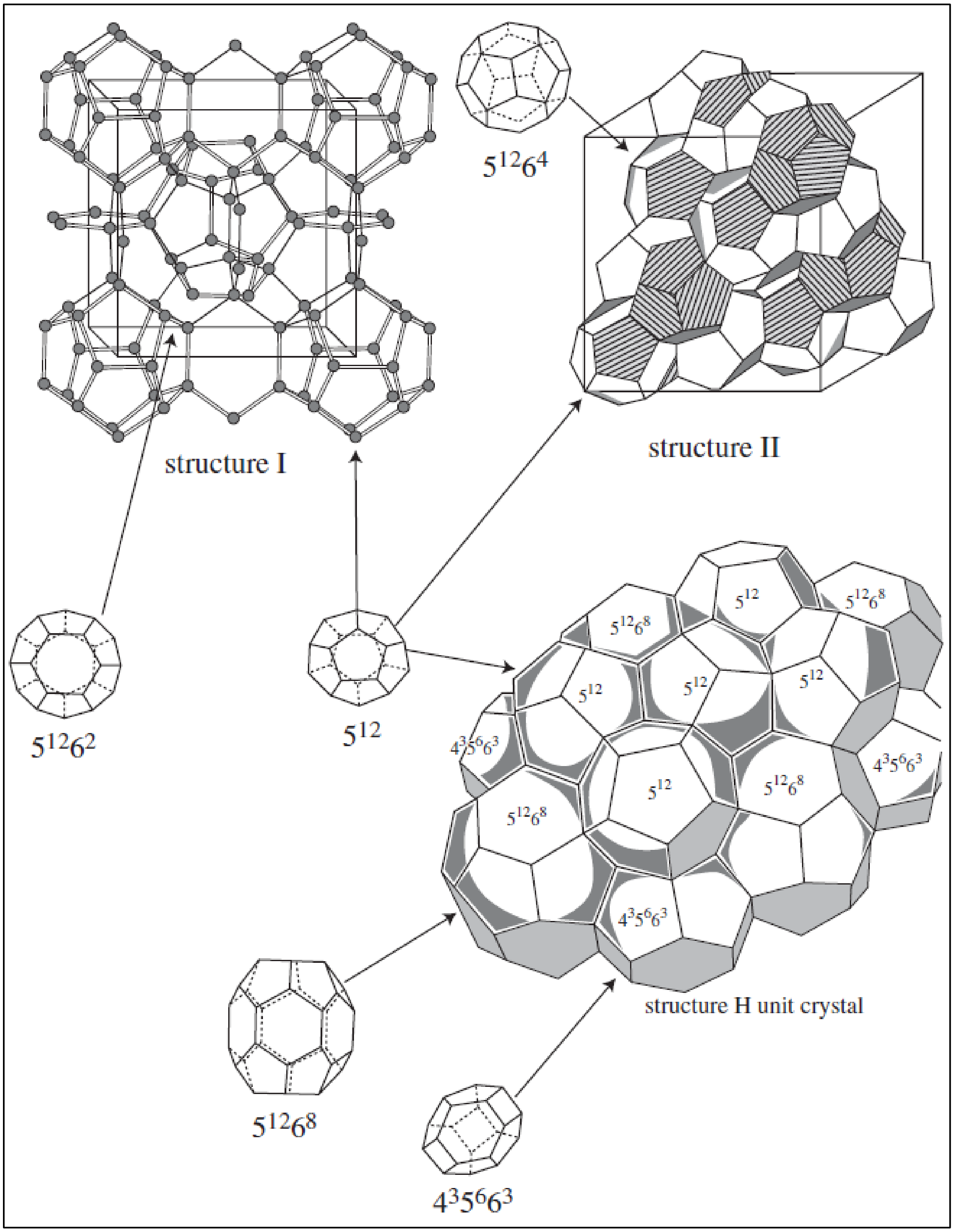
5^12 6^4
structure I
structure II
5^12 6^2
5^12
5^12 6^8
4^3 5^6 6^3
structure H unit crystal
5^12
5^12 6^8
5^12
5^12
5^12 6^8
5^12
4^3 5^6 6^3
4^3 5^6 6^3
5^12
5^12 6^8
5^12 6^8
4^3 5^6 6^3

FIG. 4. The three common hydrate unit crystal structures.[42]

Each unit cell of a sI crystal consists of 2 small pentagonal dodecahedron cavities (5^{12}) and 6 large tetrakaidecahedron cavities ($5^{12}6^{2}$), giving a total of 8 cavities (by convention, the notation x^{y} indicates a cage in which there are y units of x-sided polygons). This structure generally forms for guest molecules having diameters between 0.42 and 0.6 nm, such as methane, ethane, or carbon dioxide. Each unit cell of a sII crystal consists of 16 small 5^{12} cavities and 8 large hexakaidecahedron ($5^{12}6^{4}$) cavities. This structure forms for small guest molecules with diameter less than 0.42 nm, such as nitrogen or hydrogen, as well as larger guest molecules with diameters between 0.6 and 0.7 nm, such as propane or iso-butane. Each unit cell of a sH crystal consists of 3 small 5^{12} cavities, 2 medium irregular dodecahedron cavities ($4^{3}5^{6}6^{3}$), and 1 large icosahedron ($5^{12}6^{8}$) cavity. This structure forms for large guest molecules with diameters greater than 0.7 nm, such as iso-pentane or neohexane.[2]

In most cases, each cavity within a unit cell contains a single guest molecule. However, recent studies have indicated that three-dimensional hydrate structures can exist with metastable empty cages.[88–90] For this reason, a further characterization criterion used in the study of clathrate hydrates is the cage occupancy, which is defined as the fraction of cages that are occupied by a guest molecule. On the other hand, multiple cage occupancy for small guest molecules such as argon and hydrogen has recently been reported using both experimental and molecular simulation techniques.[7,10,91] Also, formed hydrates of particular guests may undergo structural transitions at different conditions of pressure and temperature. For example, methane hydrates undergo a sI-to-sII structural transition at 1000 bar, followed by a sII-to-sH transition at 6000 bar.[92] A detailed discussion of all the experimental studies that are related to structural transitions is presented in the review by Loveday and Nelmes.[93] A powerful predictive theory or technique must therefore be able to capture such anomalies in the general trends.

For a pure hydrate of any guest at a specified pressure, a single three-phase coexistence temperature (T_3) exists at which the hydrate phase (H) can coexist with a liquid water phase (L_W) and a vapor or liquid guest phase (G_V or G_L). This is a direct result of Gibbs phase rule which dictates that a system consisting of two components in three phases would only have one degree of freedom.[76] Therefore, the accurate prediction of T_3 is of great importance since it is the temperature boundary below which hydrate growth can proceed.

While this work focusses mainly on predicting an equilibrium property of clathrate hydrates, the MD simulation technique used is inherently dynamic. For this reason, a brief discussion of the kinetic processes that hydrates can undergo is provided here. Hydrates can undergo three kinetic processes: nucleation, growth, and dissociation. Hydrate nucleation is a process that occurs for systems that involve water and an appropriate guest molecule at conditions at or below T_3 at a given pressure. It is a microscopic phenomenon that involves tens of thousands of molecules, and includes the dispersion of clusters of water and guest molecules into the appropriate geometry for continued hydrate growth. The initially formed geometry from which hydrate growth can occur is known as the hydrate nucleus. The hydrate nucleation process is a stochastic process that can take very long times, so is difficult to observe using experimental techniques. Hydrate growth is the process by which more cages are developed on top of the hydrate nucleus, allowing the hydrate crystal to propagate in size. This process has a higher kinetic rate than hydrate nucleation, making it more suitable for experimental measurements, as well as molecular simulation studies. Finally, hydrate dissociation is the process that occurs at temperatures well above T_3 for the mixture, and involves the destabilization of the hydrate cages, causing the release of the enclathrated guest molecules.

3.1.1 Methane Hydrates Phase Equilibria

Methane has a critical temperature and pressure of 190.6 K and 46.0 bar, respectively. Therefore, methane is supercritical at most conditions that are relevant to hydrate applications. Two three-phase equilibrium regions exist for methane hydrates. At temperatures below the melting of ice, the three-phase equilibrium (I-H-V_{CH_4}) that exists involves a solid ice phase (I) in equilibrium with a H phase and a supercritical methane phase (V_{CH_4}). At the melting temperature of ice, a quaternary point exists (I-L_w-H-V) that marks the phase transition of ice to liquid water on the hydrate three-phase equilibrium line. Above this temperature, the H-L_w-V_{CH_4} equilibrium exists. The experimental three-phase equilibrium line is shown in Fig. 5, with the I-L_w-H-V_{CH_4} point marked at the melting temperature of ice. The data in the figure is obtained from the text by Sloan and Koh.[2]

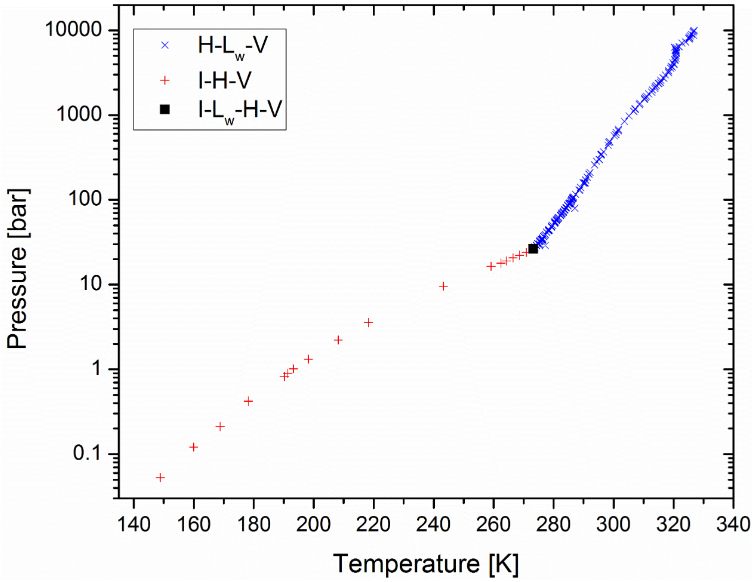

FIG. 5. Methane hydrate experimental three-phase diagram, showing the H-L_W-V_{CH4} equilibrium points (x), I-H-V_{CH4} equilibrium (+), and the I-L_W-H-V_{CH4} quaternary point (■).[2]

3.1.2 Carbon Dioxide Hydrates Phase Equilibria

Unlike methane, the vapor-liquid transition (VLE) of carbon dioxide lies well within the hydrate formation range which results in the presence of two additional, relevant three-phase equilibria. Similar to methane, at low pressures and temperatures below the melting temperature of ice, the I and H phases coexist with the vapor carbon dioxide phase (V_{CO2}). At pressures below the saturation line of carbon dioxide and temperatures above the melting of ice, the H-L_W-V_{CO2} equilibrium line exists. Starting on this line and increasing the pressure isothermally to the saturation pressure of carbon dioxide will result in a different three-phase equilibrium that does not exist in methane hydrates; namely, the H-V_{CO_2}-liquid CO_2 (L_{CO_2}) equilibrium line. At the intersection between the H-L_w-V_{CO_2} line and the H-L_{CO_2}-V_{CO_2}, a quaternary point (H-L_w-L_{CO_2}-V_{CO_2}) exists which involves the coexistence between a H phase, a L_w phase, and the VLE between V_{CO_2} and L_{CO_2}. At pressures above this intersection, a single three-phase equilibrium line exists (H-L_w-L_{CO_2}) that involves a H phase in equilibrium with L_w and L_{CO_2} phases. The experimental carbon dioxide hydrate phase diagram is presented in Fig. 6, showing the four three-phase equilibrium lines, the quaternary point, and the pure carbon dioxide saturation line.

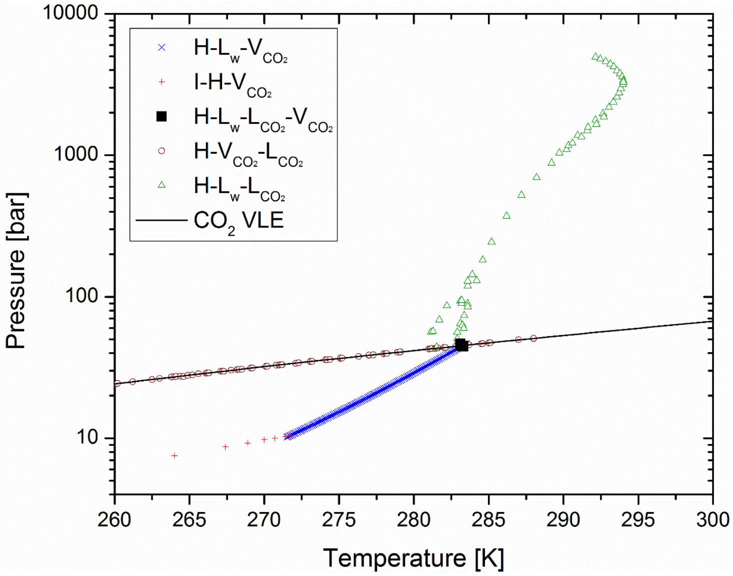

FIG. 6. Carbon dioxide hydrate experimental three-phase diagram, showing the H-L_w-V equilibrium points(x), I-H-VCO2 equilibrium (+),the I-L_w-H- V_{CO_2} quaternary point (■), the H- V_{CO_2}-L_{CO_2} equilibrium (○), and the H-L_w-L_{CO_2} (△) equilibrium.[2] The pure carbon dioxide saturation line is also shown.[94]

3.2 MD Simulations of Clathrate Hydrates

As was outlined in section 2, the ability of a simulation to accurately predict the properties of the system being studied is largely dependent on the force fields used to describe the constituent molecules. For the case of hydrates, a careful choice must be made for the model used to describe both water and the guest. It is therefore worthwhile to provide a brief outline of the available models for water and the two guest molecules used in this study; namely, methane and carbon dioxide. This is provided in section 3.2.1. A general overview of the studies involving molecular dynamics simulations of clathrate hydrates is then provided in section 3.2.2, with particular attention to the studies providing three-phase coexistence temperature predictions for methane (section 3.2.2.1) and carbon dioxide (section 3.2.2.2) hydrates, which is relevant to this work.

3.2.1 Water, Methane, and Carbon Dioxide Force Fields

3.2.1.1 Water Force Fields

Water is the most extensively studied molecule due to its relevance to a tremendous number of diverse fields. Yet, of the thousands of models available for water, not a single developed model can replicate all the compound's properties accurately. Water is a particularly challenging molecule to model due the complexity of its interactions, primarily due to its large dipole moment and ability to form hydrogen bonds. Most model parameters are derived in an empirical manner, wherein the geometry of the atoms and the charges, as well as the mathematical framework governing the intramolecular (e.g. rigid vs. flexible) and intermolecular (e.g. Lennard-Jones potential vs. Buckingham potential) are first hypothesized, followed by a parametrization procedure that provides values that replicate certain experimental properties. Common properties used for the fitting of the model parameters include the dipole moment or the dimer interaction energy if the model is intended for simulations of water in the vapor phase, or heat of vaporization and density if the model is intended for simulations of water in the liquid phase. Additionally, some models are fitted to give accurate phase equilibrium predictions. An alternative methodology used for developing models is through the use of *ab initio* calculations to calculate dimers, trimers or higher order clusters.[95]

A comprehensive review of the different models available for water has been reported by Guillot.[95] Three general types of models exist for water:

1) Rigid models, where the molecule is described as several fixed sites [e.g. Bernal-Fowler,[96] Simple-Point-Charge (SPC)[97] and its extended form (SPC/E),[98] TIP3P and TIP4P[99]].
2) Flexible models, which allow intramolecular vibrations [e.g. Matsuoka-Clementi-Yoshimine (MCY),[100] and SPC/Flexible (SPC/F)[101]].
3) Polarizable models, which include an explicit polarization term such as a charge distribution, in order to include complex effects like the dipole induced dipole mechanism in the simulations (e.g. SPCP,[102] and PTIP4P[103]).

Within each of these types, many models exist that offer different levels of accuracy for different properties. The most common type used is the rigid class due to the calculations for this class being the cheapest. The choice of model must therefore be made very carefully, with specific attention to the accuracy of the model in predicting the properties of interest in the study being conducted.

3.2.1.2 Methane Force Fields

Systems involving methane have been readily investigated using molecular simulation techniques. Methane is a simpler molecule to model than water since it does not undergo complex reactions, and interacts primarily through dispersion interactions. This results in only a few models that are commonly used to describe methane, and achieve very accurate predictions. Two types of models for the methane molecule exist:

1) All-Atom models, in which all the hydrogen atoms are explicitly represented [e.g. Optimized Potentials for Liquid Simulations–All Atom (OPLS-AA)[104]].
2) United-Atom models, where the entire molecule is described as a single, spherical Lennard-Jones interaction site [e.g. OPLS–United Atom (OPLS-UA),[105] and Transferrable Potentials for Phase Equilibria (TraPPE)[106]].

Despite the non-spherical geometry of the methane molecule, the description of the molecule using the United-Atom representation provides a reasonable description of the properties of methane, making it the favored representation used for methane simulations.

3.2.1.3 Carbon Dioxide Force Fields

The molecular simulation of carbon dioxide gained tremendous interest with the realization of global warming, and the need for predictions of the behavior of carbon dioxide in various mixtures. The main models that are used describe carbon dioxide as a three-site rigid linear model, where the partial charges are fixed on the axis of symmetry of the molecules. A positive partial charge is placed on the carbon site, and negative partial charges are placed on the oxygen sites [e.g. TraPPE,[107] Elementary Physical Model 2 (EPM2), Murthy-Singer-McDonald (MSM),[108–110] and Zhang and Duan (ZD)[111]]. The intermolecular interactions between the molecules are generally treated using the Lennard-Jones functional form, with the exception of the notable Exponential-6 (Exp-6) model[112] which describes both the repulsion and dispersion forces using an exponential functional form.

3.2.2 Three-Phase Coexistence from MD Simulations

Studies involving the molecular simulation of clathrate hydrates have been reviewed by Sum *et al.*,[91] Barnes and Sum,[114] and recently by English and MacElroy.[115] The first appearance in the literature of a study involving MD simulations on clathrate hydrates was reported by Tse *et al.* in 1983.[116] Ever since, there have been many MD studies reported that cover many different topics with regards to clathrate hydrates, mainly for methane and carbon dioxide guests.

These include studies on nucleation,[117–123] growth,[124,125] dissociation,[126–132] inhibition,[133–135] heat transfer effects,[136–138] the effect of hydrate contact with solid surfaces,[139–142] methane replacement by carbon dioxide,[60,143,144] and the calculation of transport properties such as thermal conductivity,[145–147] or thermodynamic properties such as three-phase equilibrium conditions.[148–153]

In order to predict T_3 using reasonable simulation lengths, it was found that starting from an initial system that consists of solid-fluid and fluid-fluid interfaces between the hydrate, water and guest is needed.[128,154] A commonly employed approach for the prediction of T_3 using MD simulations involves the setup of an initial multi-phase system consisting of slabs of all three phases in coexistence, then performing several simulations at the same pressure while varying the temperature. Each simulation will ultimately result in either the growth or the dissociation of the hydrate structure. The value of T_3 is then located to be between the maximum temperature at which hydrate growth is observed and the minimum temperature at which the hydrate melts. This method is known as the direct-phase coexistence method, and was first reported by Ladd and Woodcock for the three-phase coexistence of the Lennard-Jones system.[69] The direct-phase coexistence method has been used by several authors to determine T_3 of both methane and carbon dioxide hydrates.[148,153,155,156] These will be reviewed in section 3.2.2.

3.2.2.1 Methane Hydrate T_3 from MD Simulations

Fernandez *et al.* used the direct-phase coexistence method to predict the melting temperature of ice, T_m, at 1 bar using different force fields to model water, and found that different force fields predict different deviations, ΔT_m, from the experimental value of 273.2 K at 1 bar. The predicted values of T_m using the four-point models they investigated and the deviation from the experimental melting temperature for each model are shown in Table I.[154]

Table I. The melting temperature of ice, T_m, at 1 bar predicted using the four-point water models TIP4P[99], TIP4P/ice[157], TIP4P/2005[158], and TIP4P-Ew[159] as reported by Fernandez *et al.*[154] and the deviation from the experimental value of each model, ΔT_m.

Model	T_m [K]	ΔT_m [K]
TIP4P	230.5(3)	-42.7(3)
TIP4P/ice	270.0(3)	-3.2(3)
TIP4P/2005	250.5(3)	-22.7(3)
TIP4P-Ew	244.0(3)	-29.2(3)

Conde and Vega[148,155] studied the methane hydrate three-phase equilibrium with the direct-phase coexistence method. The authors showed that by varying the temperature for a given pressure, the three-phase coexistence temperature can be determined. Using a simple Lennard-Jones model for the methane molecule, they assessed the behavior of different water force fields and found that the determined coexistence temperature depends heavily on the predicted melting temperature of ice for each force field (Table I). In their simulations, they observed the formation of methane bubbles which was attributed to system size effects. Although their results exhibited significant uncertainty, they showed that the TIP4P/Ice force field[157] offers the best predictions.

Tung *et al.*[150] used the same methodology but with a different initial configuration and by using the TIP4P/Ew force field[159] for water with the OPLS-All Atom (OPLSAA)[104] force field for methane, with geometric combining rules, and using in particular for the C–O interaction, the parameters proposed by Cao *et al.*[160]

Jensen *et al.*[149] calculated the three phase equilibrium conditions using the Monte Carlo simulation method in order to calculate the chemical potential of water and methane in the hydrate phase and in the liquid and gas phase, respectively. They used the TIP4P/Ice force field for water with the OPLS-United Atom (OPLS-UA)[105] force field for methane. Their findings systematically over-predict the equilibrium temperature for a given pressure and disagree with Conde and Vega.[148]

Smirnov and Stegailov[152] followed a different approach for the determination of the equilibrium conditions of the methane hydrate. They focused mainly on the cases where the hydrate dissociates, a process which is much faster than growth. They investigated the TIP4P/Ice,[157] TIP4P/2005,[158] and SPC/E[98] force fields for water in combination with the Lennard-Jones model for methane proposed by Guillot and Guissani.[161] Their results using TIP4P/Ice agree with Jensen *et al.*,[149] and while they disagree with Conde and Vega[148] for the case of TIP4P/Ice, they agree for the case of TIP4P/2005.

3.2.2.2 Carbon Dioxide Hydrate T_3 from MD Simulations

Contrary to the case of methane hydrates,[148,153] the prediction of carbon dioxide hydrate phase equilibria with MD has attracted limited attention. In particular, Sarupria and Debenedetti[162] carried out an MD study of the dissociation rate of carbon dioxide hydrates as a function of hydrate occupancy, using the TIP4P/2005[158] and TraPPE[107] models for water and carbon dioxide, respectively. They used a system configuration of hydrate in contact with liquid water, without a carbon dioxide phase present, since they did not examine hydrate growth. They observed that the dissociation temperature is modestly dependent on the hydrate occupancy. Taking into consideration that ΔT_m for the TIP4P/2005 force field is 250.5 K,[154] they reported for the case of 30.5 bar a temperature difference between the melting of hydrate and the melting of ice of 4–8 K which is close to the experimental value of 7.15 K.

Tung *et al.*[163] used a three-phase molecular system to study the growth of carbon dioxide hydrate and to calculate the melting temperatures at different pressures using MD. The authors used TIP4P/Ew[159] and EPM2[164] models for the water and carbon dioxide, respectively, with Lennard-Jones cross interaction parameters obtained from Sun and Duan.[165] Their predictions agree with the experimental results up to 300 bar but as pressure is increased up to 1000 bar, the deviations become significant.

Miguez *et al.*[156] studied the $H\text{-}L_W\text{-}L_{CO_2}$ three-phase equilibria of carbon dioxide hydrate with MD from 20-5000 bar, and used the direct-phase coexistence method for the determination of *T_3*. First, they investigated the effect of cage occupancy on the prediction of *T_3* and observed no significant effect of cage occupancy on the prediction of *T_3* for occupancies above 75%, noting however that the presence of empty large cages can significantly affect the stability of the hydrate solid, while the presence of empty small cages has no effect. Second, they investigated the effect of the choice of water and carbon dioxide force fields on the prediction of *T_3*. To test the effect of the water force field, they used the TIP4P/Ice[157] and TIP4P/2005[158] force fields for water with the TraPPE[107] force field for carbon dioxide, and found that both water force fields give an accurate representation of the slope of the T_3 line, but have systematic deviations of -15 K for TIP4P/ice and -37 K for TIP4P/2005 from the experimental measurements.

To test the effect of the carbon dioxide force field, they found the coexistence line using TIP4P/ice water with three different force fields for carbon dioxide: the MSM force field,[108–110] the EPM2 force field,[164] and the ZD force field.[111] The authors found no significant difference in the coexistence lines predicted using the different carbon dioxide force fields. Finally, the authors hypothesized that a probable remedy for the deviation in the prediction of *T_3* from the experimental data could be the implementation of positive deviations from the Lorentz–Berthelot combining rule. They introduced a modification factor (χ) to the cross interaction energy parameter for both the oxygen in water – oxygen in carbon dioxide and the oxygen in water – carbon in carbon dioxide combining rules for the TIP4P/ice with TraPPE force field combination, and found that by using a value of 1.13 for χ, the predicted equilibrium line shifts and lands on top of the experimental coexistence line.

4. METHODOLOGY

In this work, the direct-phase coexistence methodology[69] was used for the prediction of T_3 of methane and carbon dioxide hydrates for pressure ranges of 40–600 bar for methane, and 20–1000 bar for carbon dioxide. In this method, a slab of each of the phases that take part in the equilibrium is separately prepared, and subsequently the slabs are placed in contact. The value of T_3 can be determined for each pressure by performing a temperature scan using a series of MD simulations in the NPT ensemble, and observing whether the system evolves by growth or dissociation of the hydrate phase (see Fig. 7).

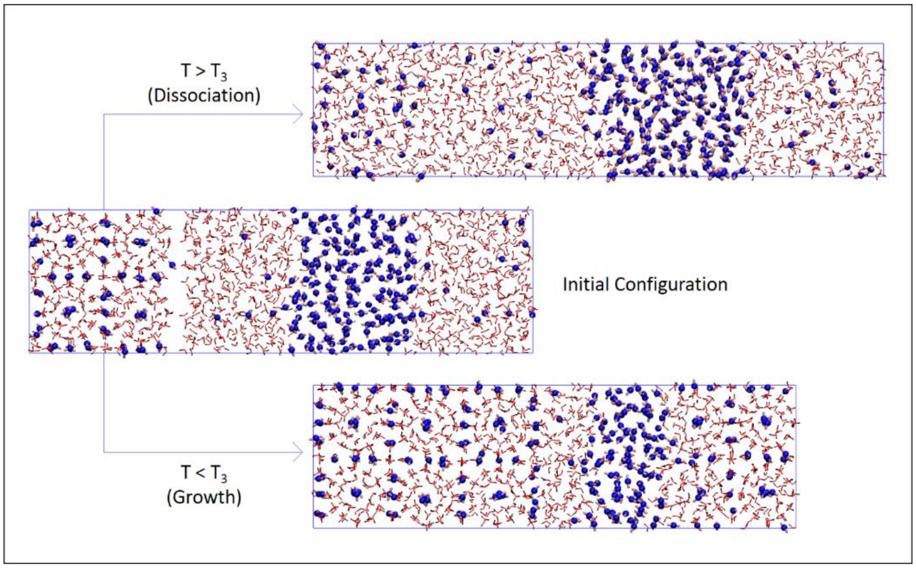

FIG. 7. Snapshots of the HWCW system at 1000 bar, showing the initial configuration, and two final states above and below T_3 that correspond to hydrate dissociation and growth, respectively. The water molecules are represented by the red and black lines. The carbon dioxide molecules are represented by the blue spheres (carbon) and pink cylinders (oxygen).

The coexistence temperature from a single temperature scan is identified as the average of the highest temperature at which hydrate growth occurs and the lowest temperature at which hydrate melting appears. Five independent temperature scans were carried out at each pressure, and the final coexistence temperature is determined as the average of the five T_3 values obtained for each pressure. The reasoning behind this statistical treatment is presented in section 5.1.2. This procedure was followed to first obtain the H-L_w-V_{CH4} coexistence line and allowed for insight into the appropriate simulation parameters needed to accurately predict hydrate phase equilibria. It was next applied to carbon dioxide hydrates, where both the H-L_w-V_{CO2} and H–L_w–L_{CO2} equilibria were predicted, and further insight into molecular level events were made, and are presented in section 5.2.

4.1 Initial Configuration Preparation

The three-phase configuration that was prepared in this study consisted of a slab of solid hydrate, a slab of the guest in the appropriate phase (i.e. liquid or vapor) under the conditions being studied, and two slabs of water on either side of the guest, giving a total of four slabs. The slabs were connected such that the interface between any two slabs was perpendicular to the x-axis.

The hydrate slab was prepared first. Both the methane and carbon dioxide hydrates form the sI hydrate structure for temperature and pressure conditions that are relevant to most industrial applications.[166,167] The positions of the oxygen atoms in a unit cell of the sI hydrate were obtained from the XRD data reported by McMullan and Jeffrey.[168] The hydrogen atoms were then placed on each oxygen atom while respecting the geometry dictated by the chosen water force field. A single guest molecule was placed at the center of each cage in a random orientation, corresponding to the case of 100% cage occupancy. A 2x2x2 supercell was subsequently created by duplicating the unit cell in the x, y, and z directions to give a hydrate slab that consists of 368 water molecules and 64 guest molecules (since a single unit cell of the hydrate sI crystal with 100% cage occupancy contains 46 water molecules and 8 guest molecules).

The initial positions of the hydrogen atoms were found by minimizing the energy of the supercell using the steepest descent algorithm (section 2.2.2), while keeping the position of all the oxygen atoms fixed. This approach results in a structure that obeys the Bernal and Fowler rules,[96] and is an alternative to the use of dipole moment minimization.[162] A short NPT simulation was then performed to equilibrate the solid slab and find its dimensions.

Two water slabs, each consisting of 368 molecules, and one guest slab was then prepared with the same y and z dimensions as those of the equilibrated hydrate slab. The guest slab contains enough guest molecules to have a comparable length in the x dimension as that of the water slabs, so that the formation of a guest bubble inside the water slab is avoided (see section 5.1.1). The appropriate number of guest molecules depends on the density of the guest at the conditions being tested, and ranges from 64 methane molecules for pressures below 100 bar, to 200 carbon dioxide molecules at all pressures. Table

II shows the number of guest molecules used at each pressure for both the methane and carbon dioxide hydrate equilibrium studies.

Table II. Number of molecules in the guest slab for each studied pressure.

Pressure [bar]	Number of Guest Molecules
CH_4 guest	
40	64
100	64
400	128
600	128
CO_2 guest	
20	200
30	200
200	200
400	200
1000	200

The methane slabs consisted of gaseous methane for all the pressures tested. However, for carbon dioxide the guest slab was carefully prepared to match the experimental phase at the pressure being tested. The quaternary point (Q_2) that marks the vapor-to-liquid transition of carbon dioxide on the three-phase coexistence line of carbon dioxide hydrates has been experimentally determined to be 45 bar,[2] so a vapor or liquid carbon dioxide slab is prepared for investigations below or above this pressure, respectively.

For the case of carbon dioxide, it was found necessary to equilibrate the liquid water (W)–carbon dioxide (C)–liquid water (WCW) system prior to connecting this three-slab system to the hydrate slab, an issue which is addressed in detail in section 5.2.1. The three, individually equilibrated slabs were connected and a 20–50 ns NPT simulation was carried out while fixing the y and z dimensions of the system. Finally, the equilibrated WCW system was placed in contact with the equilibrated hydrate slab, forming the initial configuration which has the arrangement: solid hydrate (H)–WCW (HWCW). In methane hydrates, this extra equilibration step was not necessary, so the individually equilibrated slabs were directly placed in contact with the hydrate slab, giving the arrangement: WHW-methane (M) (WHWM).

It should be noted that due to the periodic boundary conditions, both the HWCW and the WHWM arrangements are equivalent. In Fig. 7, indicative snapshots of the system are shown for the case of liquid carbon dioxide guest at 1000 bar showing the initial configuration, and the final states of simulations above and below the predicted T_3, where hydrate dissociation and hydrate growth occurred, respectively.

4.2 Force Field Description

The water molecules were modelled using the well-known TIP4P[99] molecular geometry. The TIP4P/ice[157] force field was used for both the methane and carbon dioxide hydrate studies, while the TIP4P/2005[158] force field was also used in the carbon dioxide hydrate studies to make generalizations as to the effect of the water force field. Both water force fields are rigid, non-polarizable models where a Lennard-Jones interaction site is placed at the position of the oxygen atom, while positive charges are positioned on the hydrogen atoms. The negative charge is placed on a virtual site M which lies along the bisector of the H–O–H angle.

The two force fields differ in the values of the Lennard-Jones parameters, the position of M, and the magnitude of the charges. The TIP4P/ice model was developed in order to reproduce the melting temperature of ice (Ih), with only a -3.2 K deviation in the melting temperature prediction from the experimental value, making this model a reasonable choice for the study of the phase equilibrium of the ice-like hydrate structures.

While the TIP4P/2005 model predicts a deviation of -22.7 K, it offers the advantage of having the same geometry as the TIP4P/ice force field, and is still more accurate than all the other tested rigid water models for predicting the melting of ice (see Table I). The parameters of both the water force fields are provided in Table III.

Methane was modelled using the OPLS-UA[105] force field parameters, which represents the methane molecule as a single, neutral Lennard-Jones sphere. This representation is commonly used for methane, and has been shown to accurately describe the properties of methane over a wide range of conditions. In fact, several other parametrizations have been performed for describing the methane molecule using the same united atom geometry, including the TraPPE[106] model which provides identical values for the Lennard-Jones parameters as the OPLS-UA model, and the parameters proposed by Guillot and Guissani[161] who gave the same value of σ but a slightly lower value of 147.5 K for ε/k_B compared to 148 K in the OPLS-UA force field. Parameters for the OPLS-UA model for methane are presented in Table III.

Carbon dioxide was modelled using the TraPPE[105] force field, which represents the molecule as a linear chain of three partially charged Lennard-Jones sites. The model is rigid and non-polarizable. This molecular geometry is also popular for representing carbon dioxide, and parameters for this structure have been proposed by several authors including the MSM force field,[108–110] the EPM2 force field,[164] and the ZD force field,[111] all of which provide very similar Lennard-Jones parameters, carbon and oxygen charges, and geometric parameters. The parameters of the TraPPE carbon dioxide force field are provided in Table III.

Table III. Potential parameters of the TIP4P/Ice (water)[157], TIP4P/2005 (water)[158], TraPPE (carbon dioxide)[107], and OPLS-UA (methane)[105] models. The distance, in Å, between atoms A and B is denoted d_{AB}. The angle, in degrees, formed at a central atom B separating two A atoms is denoted $\angle A–B–A$. The charge is denoted q. The Lennard-Jones parameters are denoted σ (size parameter) and ε/k_B (energy parameter, with k_B the Boltzmann constant).

Force Field	Atom	σ (Å)	ε/k_B (K)	q (e)	Geometry	
TIP4P/Ice H_2O						
	O	3.1668	106.1	0.0	d_{OH} (Å)	0.9572
	H	0.0	0.0	0.5897	$\angle H–O–H$	104.5°
	M	0.0	0.0	-1.1794	d_{OM} (Å)	0.1577
TIP4P/2005 H_2O						
	O	3.1589	93.2	0.0	d_{OH} (Å)	0.9572
	H	0.0	0.0	0.5564	$\angle H–O–H$	104.52°
	M	0.0	0.0	-1.1128	d_{OM} (Å)	0.1546
TraPPE CO_2						
	C	2.800	27.0	0.700	d_{CO} (Å)	1.16
	O	3.050	79.0	-0.350	$\angle O–C–O$	180°
OPLS-UA CH_4						
	CH4	3.73	147.5	0.0		

In the methane hydrate studies, calculating the cross-interaction Lennard-Jones parameters (interactions between the unlike molecules) was done using the Lorentz-Berthelot (LB) combining rules, given by Eqn. (30) and (31):[79]

$$\sigma_{ij} = \frac{\sigma_i + \sigma_j}{2} \tag{30}$$

$$\varepsilon_{ij} = \left(\varepsilon_i \varepsilon_j\right)^{1/2} \tag{31}$$

where σ_{ij} and ε_{ij} are the distance and energy parameters, respectively, for the interaction between atoms i and j which belong to two different molecules.

For carbon dioxide, two sets of runs were conducted. In the first, all the cross-interaction parameters were calculated using the Lorentz–Berthelot (LB) combining rules. In the second, all the cross-interaction parameters were calculated using the LB combining rules with the exception of the cross-interaction energy parameter between the oxygen in water and the oxygen in carbon dioxide ($\varepsilon_{O(CO_2)-O(H_2O)}$). An empirical modification factor (χ) was used to correct the LB cross-interaction energy parameter according to Eqn. (32):

$$\varepsilon_{O(CO_2)\text{–}O(H_2O)} = \chi\left(\varepsilon_{O(CO_2)}\varepsilon_{O(H_2O)}\right) \tag{32}$$

where $\varepsilon_{O(CO_2)}$ and $\varepsilon_{O(H_2O)}$ are the Lennard-Jones energy parameters for oxygen in carbon dioxide and water, respectively.

4.3 Simulation Details

All simulations were run using the GROMACS MD simulation package (version 4.6.5).[83–85] Periodic boundary conditions were applied in all directions. The Berendsen temperature and pressure coupling schemes[86] were applied with time constants of 1 ps for methane hydrates and 0.5 ps for carbon dioxide hydrates. Anisotropic pressure coupling was used with equal compressibility in all directions such that each dimension can fluctuate independently, in order to avoid inducing stresses to the hydrate crystal.

It should be noted that the correct interfacial tension between the slabs can be more accurately obtained by performing a semi-isotropic pressure coupling wherein the dimensions parallel to the interface (y and z dimensions) are fixed, and only the dimension perpendicular to the interface (x dimension) is allowed to fluctuate. However, upon testing the influence of such semi-isotropic pressure coupling on the predictions of T_3, and comparing the results with those obtained using the anisotropic coupling, it was found that no significant difference in the predictions is observed.

In order to conduct five independent temperature scans at each pressure, different random seeds were used for the initial velocity of the molecules at each temperature. The integration was carried out using the leap-frog algorithm using a time step of 2 fs. The simulation time was chosen to be sufficiently long to allow for clear conclusions about the final state of the system (growth or dissociation), and depended on the system being simulated, as well as the pressure and temperature conditions.

The required simulation time for methane hydrates was in the range of 1000-4000 ns, due to the very low solubility of methane in the aqueous phase. For carbon dioxide, the simulation time was in the range of 300–1000 ns for the high-pressure runs where carbon dioxide is in the liquid phase, and 500–2000 ns for the low-pressure runs where carbon dioxide is in the vapor phase. Dispersion corrections were not applied in this study due to the nature of the system being anisotropic and inhomogeneous (see section 5.1.4). A cut-off distance of 11 Å was used for both the Lennard-Jones interaction potential and the short-range part of the Coulombic interactions. The long-range Coulombic interactions were treated with the Particle-Mesh-Ewald (PME) method.[169]

5. RESULTS AND DISCUSSION[*]

The value of T_3 for methane and carbon dioxide hydrates at any pressure is obtained by performing many simulations at different temperatures for the same pressure. Two methods are used in order to determine the final state of the system (hydrate melting or growth):

1) Visual inspection of the trajectory (Fig. 7)
2) Plot of total potential energy as a function of simulation time

The results of the studies on methane and carbon dioxide hydrates are presented in this section in chronological order. First, methane hydrate coexistence was studied, and the results of this work are presented in section 5.1.[153] The results from this work provided insight into the stochasticity of the hydrate growth and dissociation processes, the necessity of long simulations, the potential for supersaturated conditions to appear and the effect of such conditions on the accuracy of the coexistence temperature predictions. Accounting for this information, the coexistence conditions of methane hydrates was predicted with high accuracy.

Next, the information gained from the study of methane hydrate coexistence was used for studying carbon dioxide hydrates, and the results of this study are presented in section 5.2. New information was gained from this work regarding the relative effect of the water-water interactions compared to the guest-water interactions on the predictions of T_3, the effect of guest solubility in the aqueous phase, and the limitations of this approach for the study of T_3.

---

[*] Parts of this chapter are reproduced with permission from “Prediction of the phase equilibria of methane hydrates using the direct phase coexistence methodology” by Michalis VK, Costandy J, Tsimpanogiannis I, Stubos AK, Economou IG, 2015. The Journal of Chemical Physics, 142, 044501, http://dx.doi.org/10.1063/1.4905572. Copyright 2015, AIP Publishing LLC.

It should be noted here that snapshots from the simulations of both the methane and carbon dioxide hydrates are presented in this work. For ease of reading, all snapshots of the methane hydrate system are presented with a black background, while snapshots from the carbon dioxide hydrate study are given a white background.

5.1 Application of the Direct Phase Coexistence Method to Methane Hydrates

5.1.1 Hydrate Growth Characteristics

In Fig. 8, three different snapshots are presented that depict the initial (0 ns), an intermediate (600 ns), and the final state (1500 ns) of a typical methane hydrate run at 294 K and 600 bar. Fig. 9 presents the time evolution of the potential energy for the case of 294 K and 600 bar for five independent runs for a simulation time of 1500 ns each. This temperature corresponds to hydrate growth conditions and is 7.7 K below the experimental equilibrium value.[170] Growth is indeed observed in all the five cases which is also clear from the decrease of the potential energy up to the equilibrium value that corresponds to the transition of the whole system to the hydrate phase.

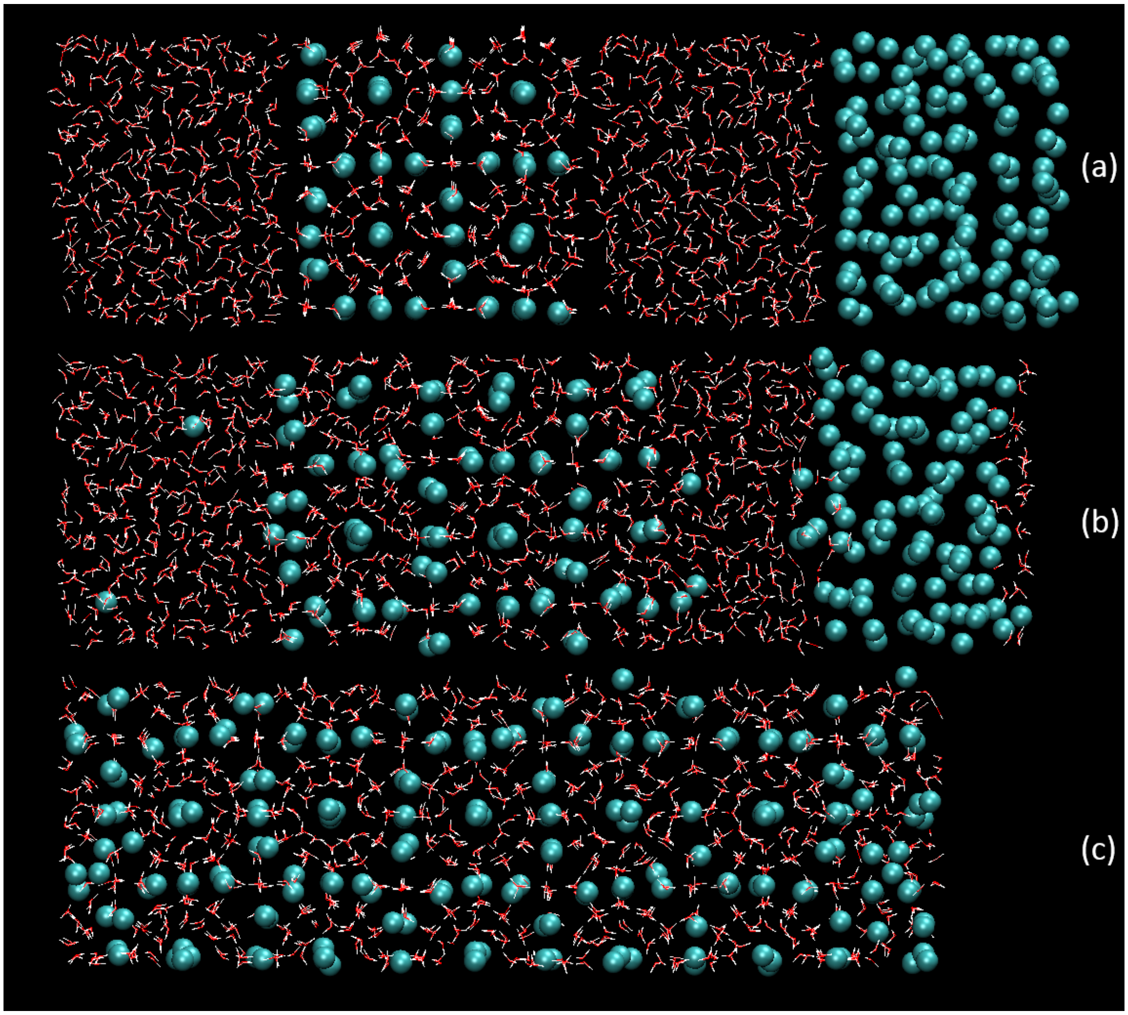

FIG. 8. Three snapshots of a typical trajectory of the WHWM system at 294 K and 600 bar (run no. 4 of Fig. 9): (a) initial configuration at t = 0 ns,(b) intermediate step at t = 600 ns, and (c) final state at t = 1500 ns. The red and white lines represent the water molecules and the blue spheres represent the methane molecules.[153]

The decrease of the potential energy in this case can be separated in two distinct stages which are characterized by different growth rates. The first one, starting from the beginning of the simulation until the onset of the second stage is the “normal” growth stage, where the methane molecules of the gas phase initially dissolve, subsequently slowly diffuse through the liquid water slabs, and eventually reach the water‐hydrate interface, where hydrate growth takes place. The beginning of the second stage is characterized by a sudden decrease of the potential energy (as is clearly indicated in the inset of Fig. 9 for the case of run no. 2) and it ends with the full conversion of the system to the hydrate phase. After this point, the potential energy of the system remains practically constant. This accelerated growth rate is due to the formation of a methane bubble which leads to locally supersaturated conditions.

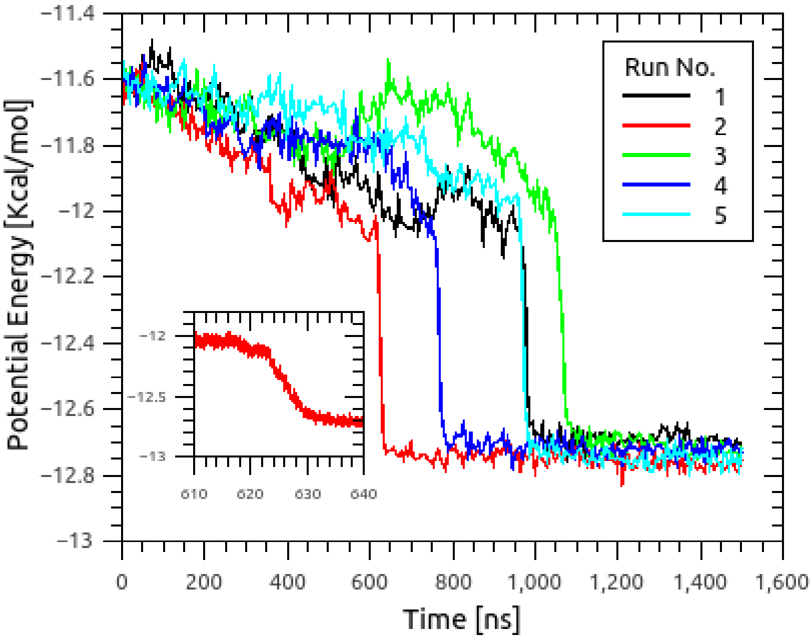

FIG. 9. Potential energy vs time for five independent NPT simulation runs of 1500 ns at 294 K and 600 bar. The inset figure focuses on the second stage of hydrate growth for the case of run no. 2.[153]

When enough methane and water molecules are removed from the gas and liquid phase, respectively, by being incorporated in the hydrate phase, then two separate possible phenomena may occur: (1) either the width of the water phase is diminished allowing the presence of the methane molecules in the vicinity of the hydrate-water interface or (2) the width of the methane slab becomes small enough and comparable to the width of the fluctuations of the water-methane interface, thus allowing the methane slab to enter the liquid phase in the form of a bubble. This bubble can be either spherical or cylindrical depending on its position with respect to the periodic boundaries. An illustrative example of a formed methane bubble is given in Fig. 10.

Similar behavior has been observed in a number of studies.[117,148] It should be noted that under the conditions of the particular example, the methane is in the supercritical state [Pc = 45.992 bar, Tc = 190.564 K (Ref. 94)] and the term “gas” is used to distinguish it from the liquid water slab.

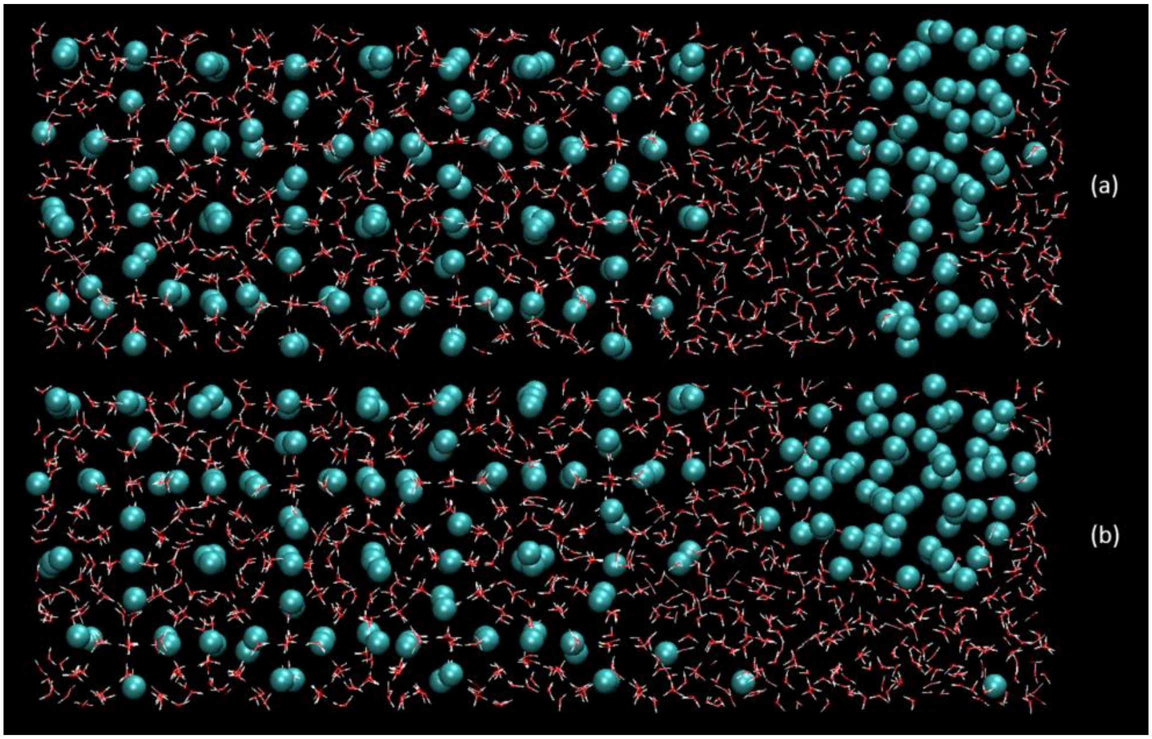

FIG. 10. Snapshots of a trajectory of the WHWM system at 290 K and 400 bar where (a) a thin methane slab is shown at t = 972.6 ns, and (b) 0.7 ns later a methane bubble has been formed. The red and white lines represent the water molecules and the blue spheres represent the methane molecules.[153]

When supersaturated conditions are present, the hydrate growth rate is significantly higher than in the case of the first stage where the methane concentration in the water is close to or at the solubility limit. In any case, in all of our simulations, due to the choice of the initial configuration, the “normal” growth stage was always present and it offered enough indication for the existence of hydrate growth, without the need of supersaturated conditions.

5.1.2 Stochastic Nature of Hydrate Growth and Dissociation

It is apparent from Fig. 9 that the “normal” growth rates of the five different runs are not equal, as indicated by the different slopes of the potential energy, a fact that must be attributed to the stochastic nature of the hydrate growth. Apart from the short-term potential energy fluctuations, there are fluctuations that expand over hundreds of nanoseconds. This case corresponds to alternating phenomena of hydrate growth and dissociation, although in the long term the system can be on average moving to one of the two final states. A direct consequence of this fact is that for the calculation of growth rates through MD simulations, averages should be used over an adequate number of runs. Additionally, the “induction” time for the bubble formation is not equal between different runs.

The effect of stochasticity that is inherent to the direct-phase coexistence methodology is more pronounced near the three-phase equilibrium conditions. Indicative results for the case of 100 bar and 283 K are presented in Fig. 11. For the given pressure of 100 bar, the experimental three-phase coexistence temperature is $T_{3,experimental}$ = 286.2 K. The temperature of 283 K is very close to expected equilibrium temperature and in line with the work of Conde and Vega.[148] These authors showed by comparing different water models that the deviation of the predicted T_3 by each model from the experimental values is correlated with the deviation of the predicted melting temperature of ice by each model from the respective experimental value (ΔT_m).

In particular, in the case of TIP4P/Ice, the predicted melting temperature of ice is 270(3) K (see Table I)[154] and thus $T_{3,expected} = T_{3,experimental} - 3.15$ K. The potential energy graphs in Fig. 11 correspond to different runs at the same pressure and temperature and show that the system for the given conditions near the equilibrium can either dissociate or form hydrate. Slightly different initial velocities in combination with the fluctuations imposed by the temperature and pressure coupling can lead to different final states (i.e., growth, dissociation). This behavior is persistent within a few Kelvin around the equilibrium temperature and it was found in all of our simulations. Additionally, it can be observed that the hydrate dissociation rate is different between the different runs in an analogous manner with that of hydrate growth that was discussed previously.

It should be noted that Espinosa *et al.*,[171] who studied the direct coexistence of a solid phase with a liquid-like phase of a pseudo hard-sphere fluid, observed a similar stochastic behavior close to coexistence conditions and additionally showed that the range of this behavior depends on the system size. Nevertheless, a very large system for the case studied in this work is computationally intractable.

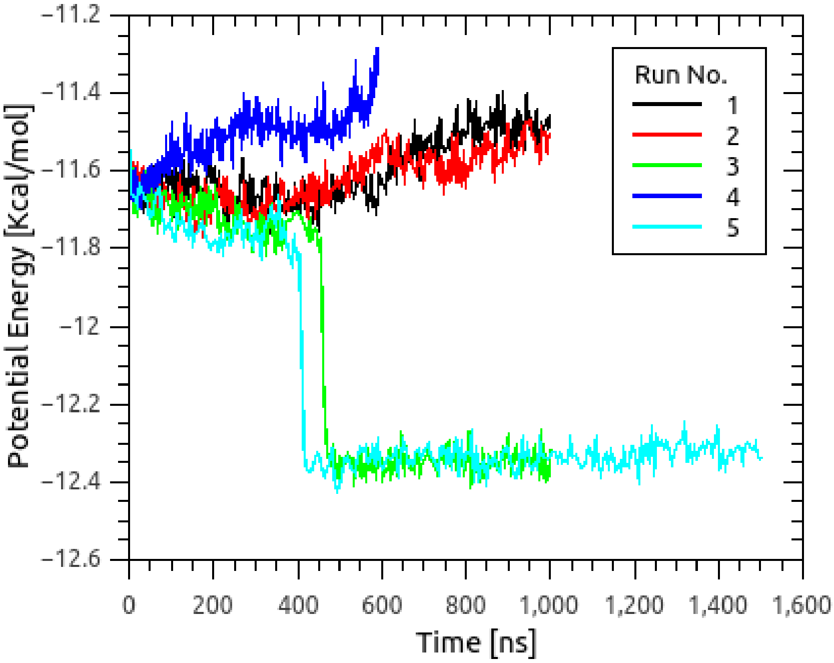

FIG. 11. Time evolution of the potential energy of five different runs at 283 K and 100 bar near equilibrium conditions.[153]

This stochastic behavior poses a severe problem in the determination of the coexistence temperature if only one run is used. Figs. 12(a) and 12(b) present two variations of temperature scans for the determination of T_3 at 100 bar. For the first case, shown in Fig. 12(a), given the information provided by the potential energy curves, the calculated T_3 is 280 K. For the second scenario, presented in Fig. 5b, a different set of runs has been used, resulting in a calculated T_3 value of 286 K. This discrepancy originates from the use of a limited (in this case just one) number of runs for each temperature and the stochastic nature of this kind of simulations.

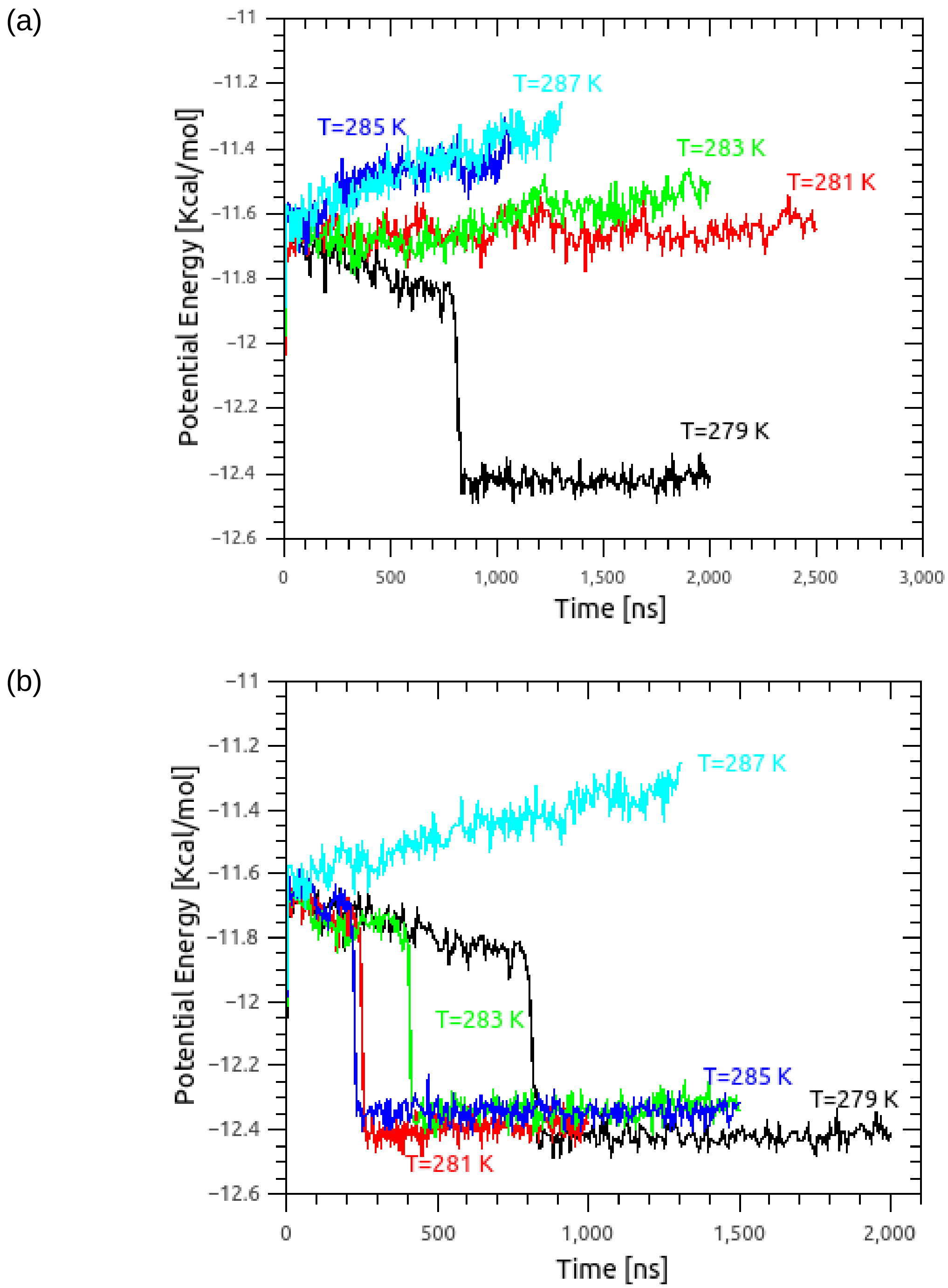

FIG. 12. Time evolution of the potential energy of two variations of temperature scans at 100 bar. Although the pressure and temperatures are the same for both figures (a) and (b), different independent runs have been selected in each scenario. In the case of figure (a) the calculated T_3 is 280 K while in the case of figure (b) it is 286 K.[153]

An additional implication which is caused by the stochasticity of the hydrate growth and dissociation processes is that the simulation time that is needed in order to draw a clear conclusion on the final state of the system varies significantly between different runs. This can be problematic particularly for temperatures near the equilibrium value. In Fig. 13 five different runs are presented for the case of 296 K and 400 bar. Under these conditions all the runs lead to dissociation but the necessary simulation time ranges between 600–2500 ns. For example it would be misleading to end the simulation of run no. 5 at a time in the range of 1100 to 1200 ns as this would draw the erroneous conclusion of hydrate growth.

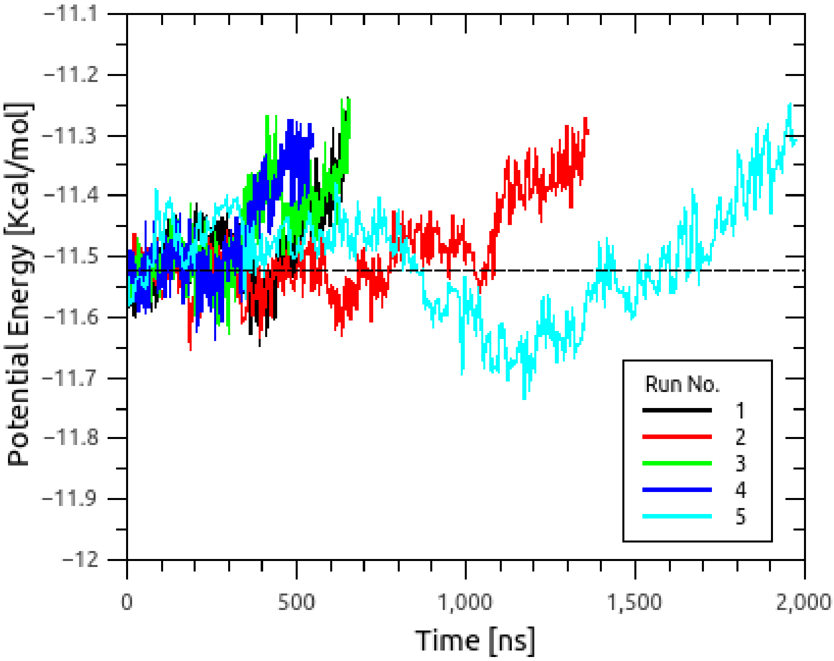

FIG. 13. Time evolution of the potential energy of five independent runs at 296 K and 400 bar. The dashed line denotes the value of the potential energy at three-phase equilibrium state.[153]

5.1.3 Calculation of T_3 of Methane Hydrates

Indicative temperature scans, as in the case of 100 bar, shown in Fig. 12, are presented for the remaining of the pressures examined in this work in Figs. 14(a), 14(b), and 14(c) for 40, 400 and 600 bar, respectively. Although, as already discussed, single run temperature scans cannot be used safely for the determination of T_3, a comparison between the different pressures reveals various trends. First, the higher the pressure, the less the required simulation time in order to draw a conclusion about the final state of the system, although for temperatures very close to T_3 this may not hold. Second, the hydrate growth rate increases by decreasing the temperature and this holds for all the pressures examined. An opposite conclusion can be drawn if a comparison is made between a limited number of runs; then due to stochasticity one could find a scenario where the higher temperatures correspond to higher rates. On average, nevertheless, the rate is increased by decreasing the temperature. Finally, in a similar manner, dissociation rate increases as temperature increases.

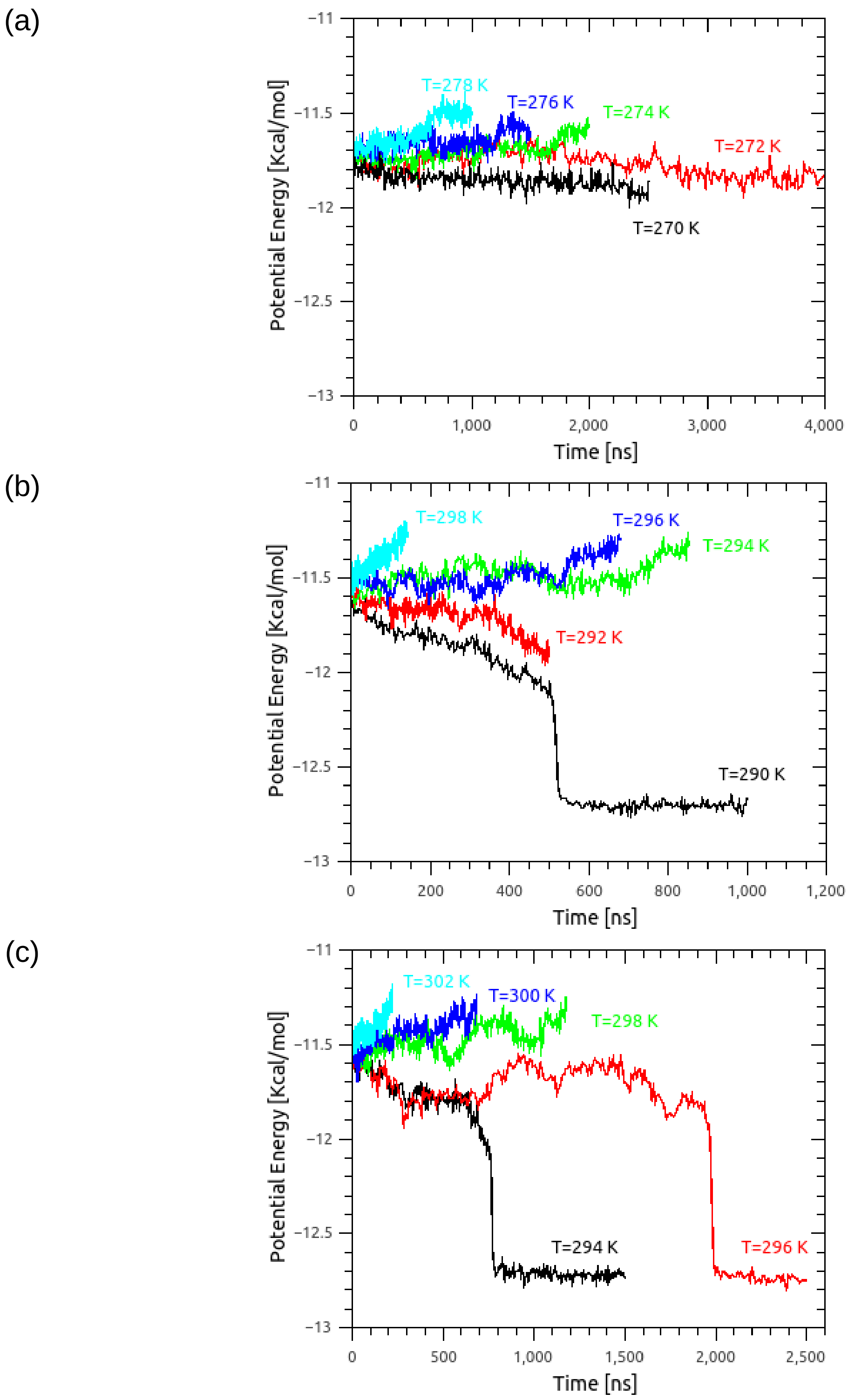

FIG. 14. Indicative temperature scans of time evolution of the potential energy for different pressure values of (a) 40, (b) 400 and (c) 600 bar.[153]

Based on the aforementioned observations and in order to determine T_3 of the methane hydrate system, we performed for each pressure a temperature scan of five different temperature values. For each temperature we performed five runs, resulting in 25 simulations per pressure. We examined four different pressure values, namely 40, 100, 400, and 600 bar, which cover a broad range of the three-phase coexistence curve of the methane hydrate. Each temperature scan was centered on the expected three-phase coexistence temperature with a step of 2 K. In line with the work of Conde and Vega,[148] we assumed that the expected T_3 is equal to the experimental value corrected by ΔT_m for the TIP4P/Ice water model. This prediction is 270(3) K,[154] and therefore, we considered a correction value of 3.15 K.

An example of the averaging method for the determination of T_3 for the case of 100 bar is presented in Table IV. The final state of each of the 25 runs is characterized as either resulting in hydrate growth (*g*) or hydrate dissociation (*d*) and the appropriate averages are calculated as the arithmetic mean of the closest temperature that corresponds to different final states. For this case of 100 bar, the calculated coexistence temperature is T_3=282.8 K with a standard deviation of 3.2 K. The experimental value of T_3 for the given pressure is 286.2 K and so there is a difference of 3.4 K, which is very close to the difference between the experimental and the expected value.

Table IV. Statistical averaging of 25 simulation runs for the determination of the T_3 at a pressure of 100 bar. The calculated temperature is T_3 = 282.8 K with a standard deviation of 3.2 K. The final state of each realization is denoted as (*g*) for hydrate growth or (*d*) for hydrate dissociation.[153]

T (K)	Number 1	Number 2	Number 3	Number 4	Number 5
279	*g*	*g*	*g*	*g*	*g*
281	*g*	*g*	*g*	*g*	*d*
283	*g*	*g*	*d*	*d*	*d*
285	*g*	*d*	*d*	*d*	*d*
287	*d*	*d*	*d*	*d*	*d*
T_3 (K)	286	284	282	282	280

The results for all the four different pressure values examined in this work are presented in tabulated form in Table V and plotted in Fig. 15 along with the experimental values,[170] the expected values, the results by Conde and Vega,[148] and the results by Tung *et al.*,[150] who also used the direct phase coexistence methodology. Additionally, the results by Jensen *et al.*[149] [85] and Smirnov and Stegailov have been included.[152]

Table V. Experimental and calculated T_3 along with standard deviations, and deviation of predictions from experimental values. Experimental values are taken from the polynomial fit reported by Moridis.[153,170]

P [bar]	$T_{3,\text{experimental}}$ [K]	$T_{3,\text{this work}}$ [K]	ΔT [K]
40	277.4	273.0(2.4)	-4.4
100	286.2	282.8(3.2)	-3.4
400	297.2	293.4(0.9)	-3.8
600	300.7	297.0(0.0)	-3.7

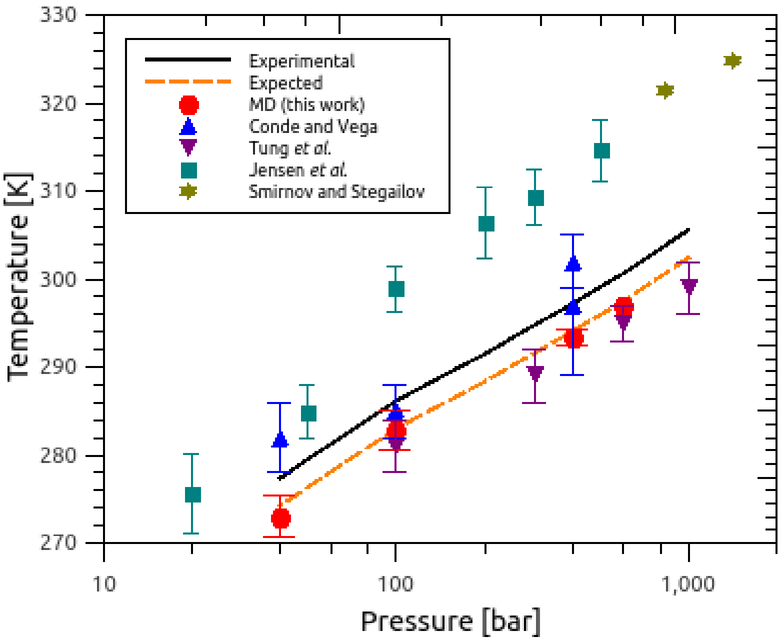

FIG. 15. Experimental[170] and calculated values from this work and from the literature for the three-phase coexistence temperature of the methane hydrate system (Conde and Vega,[148] Tung *et al.*,[150] Jensen *et al.*,[149] and Smirnov and Stegailov[152]). All authors used TIP4P/Ice except Tung *et al.* who used TIP4P/Ew. The expected values presented in the figure are defined as $T_{3,expected} = T_{3,experimental} - 3.15$ K.[153]

The results of the present work are in excellent agreement with the expected values ($T_{3,expected} = T_{3,experimental}$ – 3.15 K) in the examined range of 40 – 600 bar. The obtained results exhibit the capability of the specific methodology to offer a consistent prediction of the three-phase coexistence conditions with increased accuracy. The predictions by Conde and Vega, although in qualitative agreement, are not quantitatively consistent with the slope of the experimental values. On the other hand, the deviation of the results of Tung *et al.* are consistently on average 5.8 K lower than the experimental values. The predicted melting temperature of ice using the TIP4P/Ew water model is 244(3) K[150] which is approximately 29 K below the experimental value. This result is not in agreement with the conclusions of Conde and Vega[148] that the shift in the predicted T_3 follows the deviation of the predicted melting temperature of ice by the water model in use. A probable reason for this discrepancy could be the use by Tung *et al.* of modified cross-interactions parameters between the oxygen atom of water and the carbon atom of methane. The synergetic effect on the calculation of T_3 between the predicted melting temperature of a water force field and the methane-water interaction has been also pointed out by Conde and Vega.[155]

At this point, it is unclear whether such modifications of the cross-interaction parameters lead to different and probably increased solubility of methane in water and if this aspect is more important than the effect of the water model of choice on the calculation of the coexistence temperature. This question is addressed further in the work on carbon dioxide hydrates presented in section 5.2.

Jensen *et al.*,[149] who used a different methodology that is based on thermodynamic integration and MC simulations with TIP4P/Ice for the calculation of chemical potentials, systematically over-predicted T_3. On the other hand, the results of Smirnov and Stegailov[152] that appear to be in agreement with Jensen *et al.* are based on MD calculations of direct phase coexistence of methane hydrate with liquid water and without any methane gas phase.

It is clear from visual inspection of the trajectories of numerous runs that below a critical number of methane molecules in the gas phase in contact with the liquid water, methane is forming a gaseous bubble (see Fig. 10). This bubble is moving inside the liquid water and as soon as it comes in contact with the hydrate slab the hydrate growth becomes extremely fast. Locally, at the hydrate–water interface, the presence of the methane bubble corresponds to supersaturated conditions well above the solubility limit.

In order to directly test the effect of supersaturation, simulations have been carried out where the hydrate was placed in contact with liquid water artificially supersaturated with methane. A 2x2x2 hydrate slab was used with 368 water and 64 methane molecules and a supersaturated liquid water slab with 368 water and 32 methane molecules. In this case, it was observed that hydrate growth was occurring even for temperatures that were well above the experimental T_3. For example, at 400 bar, it was found that dissociation occurred for temperatures above 333 K, which is 36 K above the experimental value. This fact can provide a possible explanation for the over-prediction of T_3 in Conde and Vega's results at certain pressures. For example, at 400 bar they presented hydrate growth at 300 K [76] while in this work, where bubble formation was carefully avoided for as long as possible, only dissociation occurs at this temperature.

Additionally, this phenomenon can provide a possible explanation to the over-prediction of T_3 by Smirnov and Stegailov who did not use a methane gaseous phase in their methodology. In their case, it is possible that during the dissociation, the methane molecules from the hydrate locally increased the methane concentration in the liquid water over the solubility limit, contrary to the setup used in this work where the methane molecules that have been released from the dissociated hydrate cages diffuse through the liquid water and enter the gas phase.

5.1.4 Effect of Dispersion Tail Corrections

Although widely known, it is worthwhile mentioning that the direct contact of different phases *via* a finite interface renders the use of dispersion corrections inapplicable (see section 2.3.2.1 for details about dispersion corrections).[79] The dispersion corrections are customarily used in MD simulations due to the unavoidable calculation of the attractive dispersion potential up to a cut-off value as the size of the simulation box is finite. The truncation of the potential is compensated by the use of dispersion corrections, also named tail corrections, and it is based on the assumption that the simulated system is isotropic and homogeneous. This assumption means that the radial distribution function of the system for distances greater than the cut-off value is equal to one and thus an analytic expression for the corrections can be calculated.

In the case of the direct-phase coexistence method, as described in this work, it is clear that dispersion corrections cannot be used as the system is anisotropic and inhomogeneous. In particular, the use of tail corrections in combination with pressure coupling produces misleading results which are manifested mainly in erroneous values of the gas phase density.

In Fig. 16, the density profile is presented for a system of gaseous methane in equilibrium with liquid water at 100 bar and 280 K with and without dispersion corrections. The results presented here are for a methane – water – methane configuration with 64 – 368 – 64 molecules, respectively. The MD-calculated bulk density of the methane in the case where dispersion corrections are used is approximately 139 kg/m^3, while in the case without dispersion corrections the calculated density is 78 kg/m^3. The experimental density[94] for these conditions of the pure methane is 85.5 kg/m^3. Although the particular conditions of this example are within the hydrate growth regime, similar behavior is observed in a wide temperature and pressure range. Effectively, the dispersion corrections in combination with pressure coupling are causing compression of the gas phase, an effect which is more pronounced for lower values of pressure according to the observations made in this work.

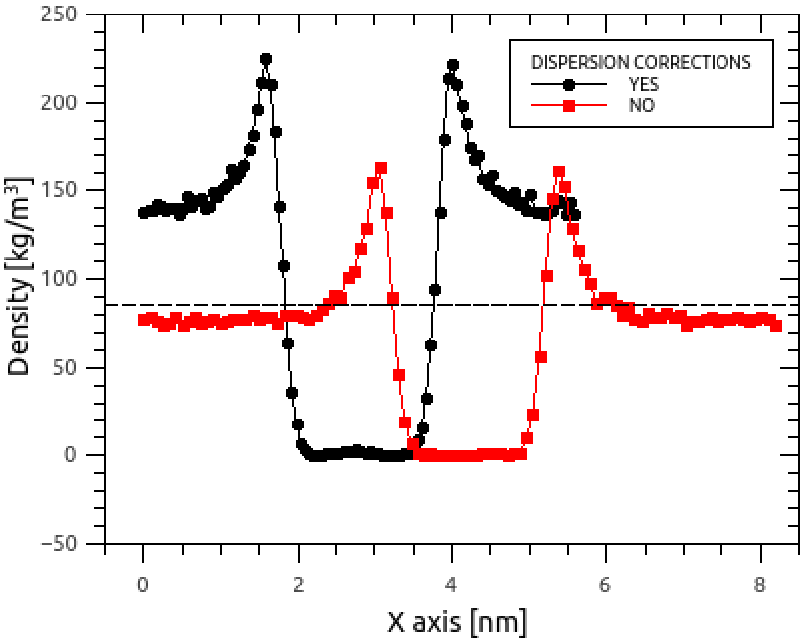

FIG. 16. Density of methane in a methane–water–methane configuration at 280 K and 100 bar, with and without dispersion corrections. The dashed line depicts the experimental value of the pure methane reported by NIST.[94,153]

Without the use of dispersion corrections, which is the case for all the simulations presented in this work for the determination of T_3, there is a persistent error in the calculated densities of the order of approximately 5–10 % for the gas phase and 1 % for the liquid water phase. Nevertheless, it appears that the magnitude of these deviations does not affect the calculation of the three-phase hydrate equilibrium conditions.

5.1.5 Calculation of Methane Solubility in the Aqueous Phase

The solubility of methane in the aqueous phase along the H-L_W-V_{CH_4} equilibrium curve, as calculated by the current MD simulations, has also been estimated for the cases of the four pressures that were considered in the current study. The calculated MD results are shown in Fig. 17 where the solubility of methane is plotted as a function of T_3 as calculated in this work. Shown also are the solubility calculations by two different continuum-scale models[2,172] as a function of the equilibrium temperature as calculated by those models. A detailed discussion on the performance of such thermodynamic models in predicting methane solubility in water has been reported recently by Tsimpanogiannis *et al.*[173] One should recall that the T_3 of the MD simulations consistently deviates by 3.5 K form the experimental values for each given pressure.

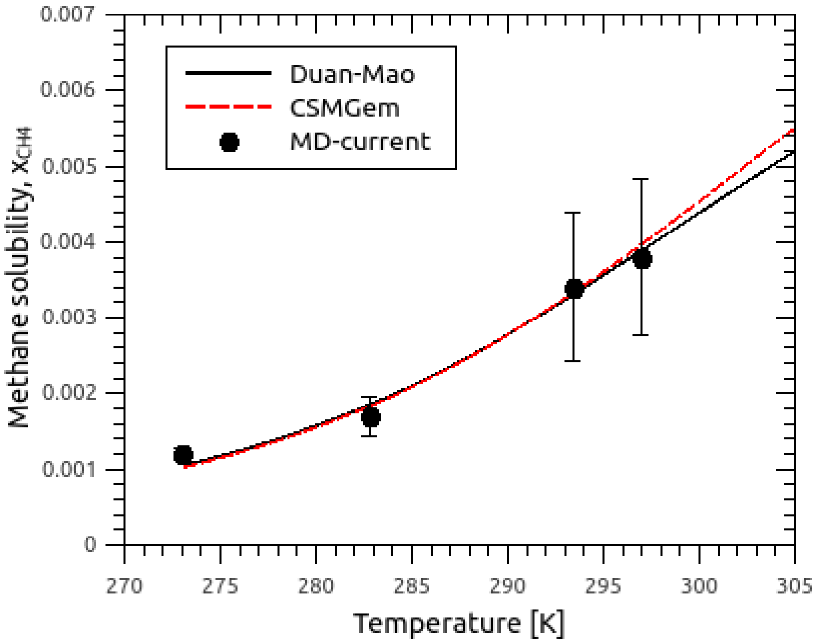

FIG. 17. Methane solubility in water as a function of the three-phase coexistence temperature. Circles denote MD calculations and lines denote continuum-scale models.[2,153,172]

We observe that good agreement between the MD simulations and the two thermodynamic models is obtained. Such behavior should be expected for the TIP4P/Ice water model based on the findings by Docherty *et al.*,[174] and the discussion presented by Conde and Vega.[148] In particular, Docherty *et al.* reported that in order to describe correctly the excess chemical potential of methane in water, a positive deviation from the energetic Lorentz–Berthelot combining rule needs to be introduced for the cross-interaction parameters of water and methane for the case of the TIP4P/2005[158] model for water in combination with the Lennard–Jones parameters reported by Guillot and Guissani[161] for methane. In that particular case, the deviation is 7 %. As discussed by Conde and Vega,[148] such an approach produces, essentially, the same cross-interaction energy parameter as in the case of TIP4P/Ice with the Guillot and Guissani methane model using standard Lorentz–Berthelot rules. Additional discussion related to methane dissolved in water can be found in the work of Reed and Westacott.[175]

5.1.6 Summary of Findings of Methane Hydrate Study

First, it was found that the inherent stochasticity of the direct-phase coexistence method can cause the prediction of erroneous results. This problem was rectified by performing a statistical analysis of multiple independent runs at each pressure and temperature. Second, it was shown that the occurrence of a supersaturated aqueous phase is likely if the number of gas molecules is small, and this leads to a large over-prediction of T_3. It was therefore found necessary to include a sufficient number of gas molecules in the gas-rich phase in order to allow for an accurate conclusion to be made about the final state of the system. Third, it was found that the use of the TIP4P/ice force field in combination with the OPLS-UA model for methane provides an excellent prediction for the value of T_3 with a consistent deviation of approximately -3.5 K from the experimental value of T_3, in agreement with the deviation of the prediction of the TIP4P/ice force field for the melting of ice. Fourth, this force field combination also gives an accurate prediction of the solubility of methane in water. Finally, it was confirmed that a large error in the gas density is caused if dispersion tail corrections are used for this anisotropic and inhomogeneous system.

5.2 Application of the Direct Phase Coexistence Method to Carbon Dioxide Hydrates

5.2.1 Equilibration of the WCW Configuration

As was mentioned in section 4.1, an additional step was found necessary in the preparation of the four-slab configuration for the carbon dioxide system; namely, the equilibration of the WCW configuration prior to its attachment to the hydrate slab for the determination of T_3 using the direct-phase coexistence method. Contrary to the case of methane hydrates[153] where each phase was individually equilibrated and then brought in contact with the other phases, for conditions below the quadruple point where the carbon dioxide is in the vapor phase it was found that the equilibration of the vapor carbon dioxide with the liquid water must be done in a separate stage as it requires careful handling. This is due to the fact that the carbon dioxide molecules, under the conditions examined in this work, are strongly “adsorbed” on the water surface creating a liquid-like film.

Since the y and z dimensions of the box are practically constant at the values dictated by the dimensions of the 2x2x2 hydrate supercell, and due to the low density of carbon dioxide in the vapor phase, the removal of carbon dioxide molecules from the bulk vapor, and into the adsorbed film at the interface, results in a severe reduction of the box size in the x dimension. The equilibration of this adsorption process requires a relatively long time, in the range of 20 – 50 ns, and thus it must be done separately for each pressure and temperature in order to avoid any complications during the simulations when the hydrate phase is also present.

In order to illustrate this issue, a snapshot of the equilibrated liquid water – vapor carbon dioxide interface is presented in Fig. 18 for a typical simulation at 30 bar and 274 K. The existence of an adsorbed carbon dioxide layer is apparent. Additionally, the inset figure shows the full WCW system before and after equilibration to illustrate the reduction of the simulation box size. The respective densities of carbon dioxide and water for the aforementioned case, in the equilibrated WCW configuration, are presented in FIG. 19. While the density of the bulk vapor carbon dioxide is very close to the experimental value of 76.7 kg/m^3,[94] the carbon dioxide density at the interface is close to 600 kg/m^3 which is about 8 times higher than the vapor density (and still approximately 2/3 of the liquid carbon dioxide density at the corresponding saturation conditions).

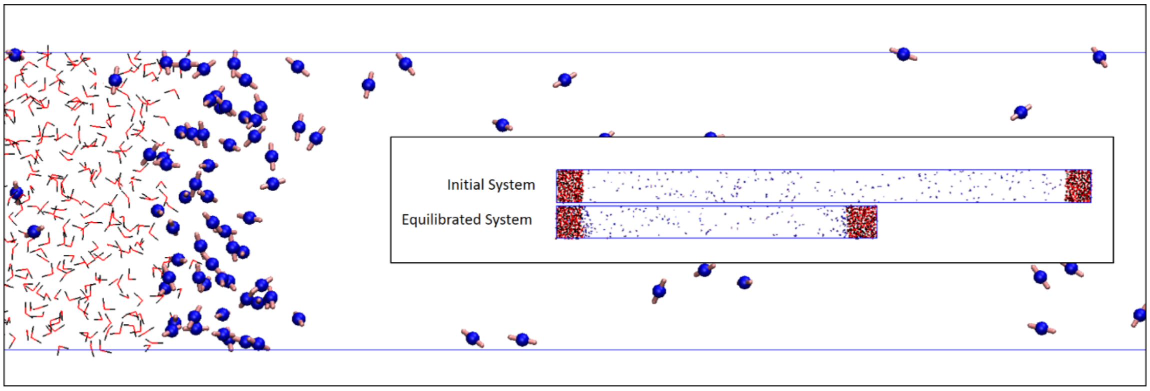

FIG. 18. Snapshot of the liquid water – vapor carbon dioxide interface after equilibration of the WCW system at 30 bar and 274 K, showing the film of carbon dioxide on the water surface. The water molecules are represented by the red and black lines, while the carbon dioxide molecules are represented by the blue spheres (carbon) and pink cylinders (oxygen). The inset figure shows the full system before and after equilibration.

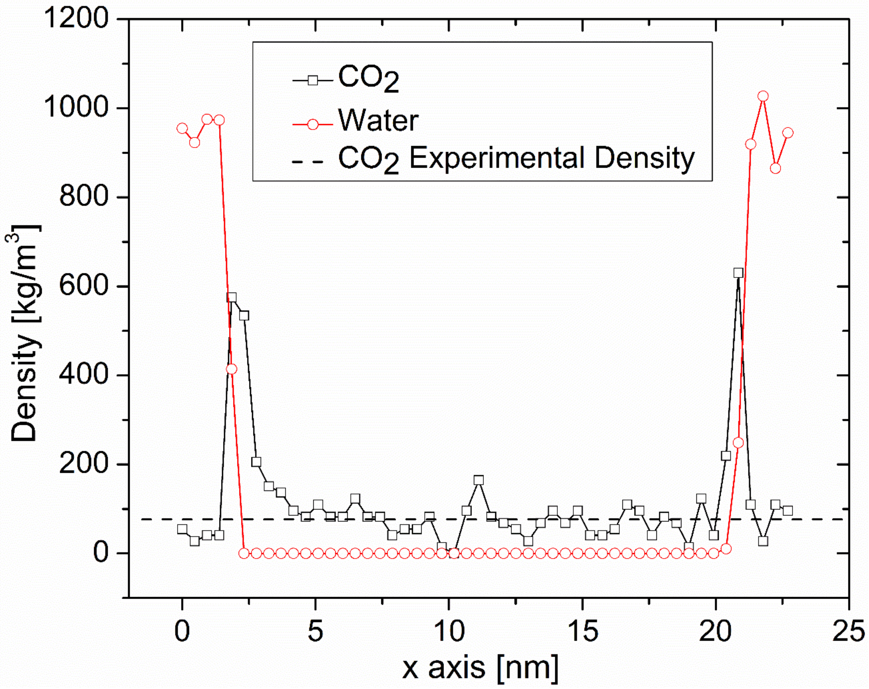

FIG. 19. Density of carbon dioxide (black squares) and water (red circles) along the direction normal to the interface (x axis) in the WCW system at 30 bar and 274 K (vapor carbon dioxide). The dashed line represents the experimental value of the density of pure carbon dioxide [94]. The solid lines are a guide to the eye only.

The existence of an adsorbed carbon dioxide layer is in agreement with the work of Lehmkuhler *et al*.[176] who studied the water – carbon dioxide interface by X-ray diffraction and reflectivity at hydrate-forming conditions. Reflectivity measurements at 273.3 K from low pressures up to the condensation pressure of 35 bar indicated the adsorption of gas molecules on the water surface with a thickness varying from a few Å up to 40 Å at the condensation pressure of 34.99 bar. Additionally, our observations are in agreement with the observations of Zhang and Singer[177], who performed an extensive MD study on the water – vapor carbon dioxide interface and reported the development of a carbon dioxide film at the interface. Using the SPC[98] and EPM2[164] models for water and carbon dioxide respectively, they carried out NPT simulations at 300 K from the low density limit to near-critical pressures and they found a similar enhancement factor of the density at the interface with respect to the bulk density.

The authors also concluded that although the water density profile hardly changes with pressure, the enhancement factor of the carbon dioxide density at the water interface is quite pronounced for the low pressures where carbon dioxide exists in the vapor phase.

5.2.2 Calculation of T_3 Using LB Combining Rules

After the equilibration of the WCW slabs, contact with the equilibrated carbon dioxide hydrate slab allows for the determination of T_3 by scanning the temperature at each target pressure and observing the evolution of the potential energy of the system. The combination of TIP4P/Ice with TraPPE forcefields for water and carbon dioxide, respectively, was examined first using the LB combining rules, given by Eqns. (30) and (31).

The coexistence temperature was calculated for 5 values of pressure; namely, 20, 30, 200, 400, and 1000 bar which cover both the vapor and liquid carbon dioxide regions. Indicative snapshots of the system at 1000 bar were presented in Fig. 7, showing the initial configuration, and the final states of simulations at 282 K and 277 K, where hydrate dissociation and hydrate growth occurred, respectively.

An indicative evolution of the potential energy of this system for four different temperatures is presented in Fig. 20. As was the case for methane, the value of T_3 was estimated as the average of the highest temperature at which hydrate growth occurs (280 K in Fig. 20), and the lowest temperature at which hydrate dissociation occurs (281 K in Fig. 20). For the temperature scan shown in the figure, T_3 would be estimated as 280.5 K.

By conducting five independent runs at each temperature and pressure condition investigated, in order to account for the stochastic behavior of the system, one can determine an average value of T_3 for any given pressure. In addition, the potential bubble formation that was discussed for the case of methane hydrates was avoided in this study by using a large carbon dioxide slab that consists of 200 carbon dioxide molecules.

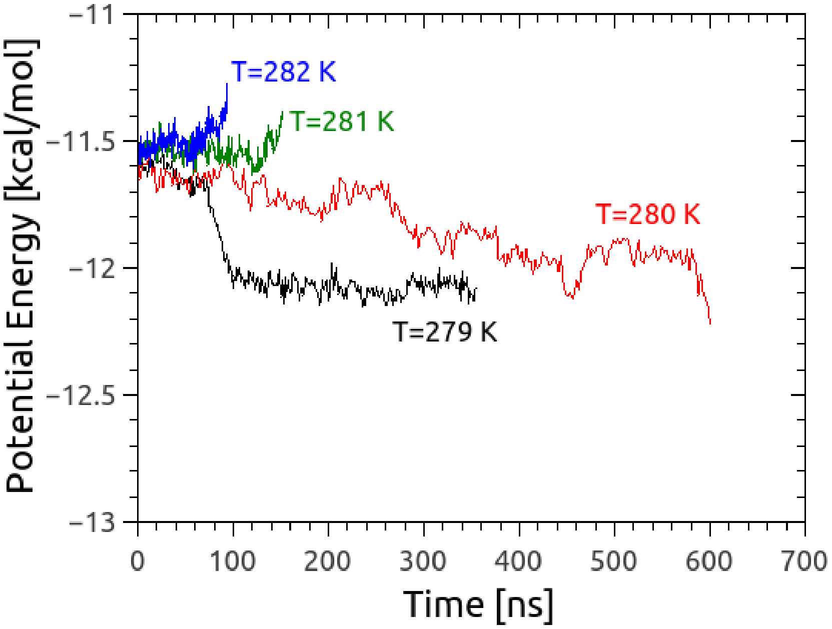

FIG. 20. Evolution of the potential energy with time of the HWCW system using the TIP4P/ice model for water and the LB combining rules at 1000 bar and four different temperatures.

The calculated T_3 values are presented in Table II. For the pressures examined, the use of TIP4P/Ice with the LB rules systematically underestimates T_3 by 9–12 K. Although for the case of methane hydrates the predictions of T_3 with TIP4P/Ice deviated from the experimental values only by the deviation of the predicted melting temperature of ice (3.15 K), the deviation in the case of carbon dioxide, described by the TraPPE force field, is much larger. These findings are in agreement with the work of Miguez *et al.*[156] who found a deviation of approximately 15 K by using the same force field combination.

Table VI. Experimental[2] and calculated three-phase coexistence temperatures (T_3; statistical uncertainty in parenthesis) using the TIP4P/Ice and TIP4P/2005 water forcefields for the cases where cross-interaction parameters are calculated using the LB combining rules (χ = 1.00) and where the modification parameter χ was applied with value optimized with respect to the carbon dioxide solubility in water.

Pressure [bar]	T_3 [K]				
	Experimental	TIP4P/ice		TIP4P/2005	
		χ = 1.00	χ = 1.08	χ = 1.00	χ = 1.115
20	277.1	270.0 (0.0)	279.0 (0.0)		
30	280.2	270.0 (0.0)	277.1 (0.5)		
200	284.7	274.2 (1.6)	281.5 (0.9)	250.9 (1.8)	261.2 (1.3)
400	286.2	276.0 (0.7)	283.5 (0.7)	252.5 (1.2)	262.5 (0.0)
1000	289.7	280.1 (1.7)	287.3 (0.8)	256.1 (1.1)	265.6 (0.5)
2000	293.0		289.9 (1.7)		
3000	293.9		290.9 (1.3)		
4000	293.6		289.7 (0.8)		
5000	292.1		288.7 (1.3)		

5.2.3 Optimizing the Cross-Interaction Parameters

The large deviation in the prediction of T_3 of 9 – 12 K that was reported in the previous section could be due to the simplicity of the two-body potentials used to describe the complex dipole-quadrapole interactions between water and carbon dioxide. It was hypothesized that the cause for this deviation in the measurement of T_3 is the under-prediction of the solubility of the carbon dioxide guest in the aqueous phase. If this is true, the concentration of carbon dioxide at the hydrate-water interface would be lower than the experimental value, which would disable the growth of the hydrate solid and ultimately reduce the measurement of T_3.

In order to correct this large deviation in the predicted T_3, the interactions between the water and carbon dioxide molecules were modified, with the target of minimizing the error in the prediction of carbon dioxide solubility in water. The cross-interaction Lennard-Jones energy parameter between the oxygen of water and the oxygen atoms of carbon dioxide was chosen for modification.

This choice was based on the findings of Orozco *et al*.,[178] who carried out an optimization of the intermolecular potential parameters in order to describe the phase behavior of the water–carbon dioxide system. Although the authors concluded that for the potentials they examined there is no combination of unlike interactions that can provide a satisfactory description of both phases, they noted that variations in the Lennard-Jones interactions between unlike molecules have an important effect on the solubility of carbon dioxide in the water-rich phase, and additionally that the stronger quantitative response comes from variations in the oxygen in water–oxygen in carbon dioxide unlike interactions. Furthermore, the authors found that the solubility of carbon dioxide in water is much more sensitive to changes in the Lennard-Jones energy parameter compared to changes in the size parameter. For this reason, of the two Lennard-Jones cross-interaction parameters, only the cross-interaction energy term was modified in this work.

Thus, a modification factor χ was introduced as described by Eqn. (32), and the solubility of carbon dioxide in water was calculated for various values of

χ. For the solubility calculations, a large water slab consisting of 2000 water molecules was placed at the center of a box and was surrounded on either side by a slab of 125 carbon dioxide molecules, with the interfaces normal to the x direction, giving a carbon dioxide – water –carbon dioxide (CWC) slab arrangement. The size of water slab was chosen such that a bulk water phase with sufficient distance away from the interface was available, in order to make the solubility measurements.

We selected to calculate the solubility dependence on χ at an experimental equilibrium point, namely at 400 bar and 286 K. It was assumed that a single value of χ was needed for the entire pressure range. The reason for making this assumption is that it is expected that the increase in affinity between the water and carbon dioxide that is needed to obtain the correct solubility should not be a function of pressure for the same phase equilibrium line.

After an equilibration period of 5 ns, 100 ns-long NPT simulations were performed for each value of χ. A snapshot of the configuration after the 100 ns NPT simulation of the LB case is shown in Fig. 21. The number density profile for water and carbon dioxide across the x axis was plotted every 2 ns, giving a total of 50 measurements of carbon dioxide solubility in water for each value of χ used, in order to reduce the statistical uncertainty. A representative density profile is shown in Fig. 22. The solubility for any snapshot was found using Eqn. (33):

$$x_{CO_2} = \frac{\text{No. of CO}_2\text{ molecules in control volume within water slab}}{\text{Total No. of molecules in control volume within water slab}} = \frac{\cancel{yz}\int_{x_1}^{x_2}\left(\rho_{CO_2}\right)dx}{\cancel{yz}\int_{x_1}^{x_2}\left(\rho_{CO_2}+\rho_{H_2O}\right)dx} \tag{33}$$

where ρ_{CO_2} and ρ_{H_2O} are the number densities of carbon dioxide and water, respectively, y and z are the lengths of the y and z dimensions of the box (approximately 2.4 nm for a 2x2x2 hydrate supercell), and the integration limits are two positions along the x dimension of the box that are within the water slab and far from the water–carbon dioxide interface. For example, in the representative density profile in Fig. 22, $x_1 = 3$ nm, $x_2 = 10$ nm, the numerator of Eqn. (33) is the area shaded in red, and the denominator of Eqn. (33) is the sum of the red and grey areas.

The results of this procedure are presented in Fig. 23. The classic LB combining rules correspond to a value of χ equal to one. The cross-interaction energy parameter of the oxygen atoms between the water and carbon dioxide molecules affects strongly the solubility of carbon dioxide in water, with a modification of 15% in χ corresponding to a change of approximately 80% in solubility. We found that for the TIP4P/Ice model, the deviation from the experimental value of solubility[179] is minimized with $\chi = 1.08$.

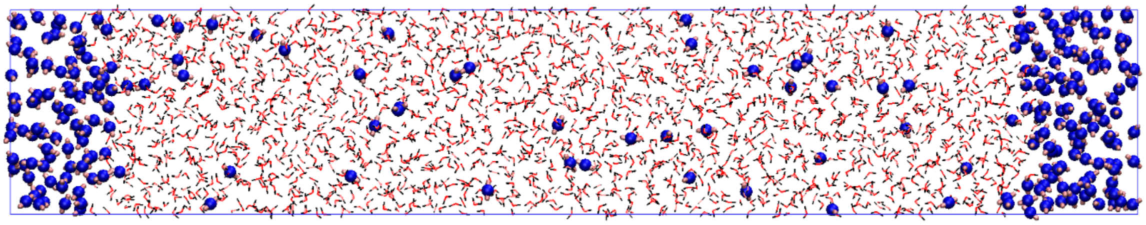

FIG. 21. Snapshot of the CWC configuration after 50 ns using the LB combining rules. Molecule representation is the same as Fig. 18.

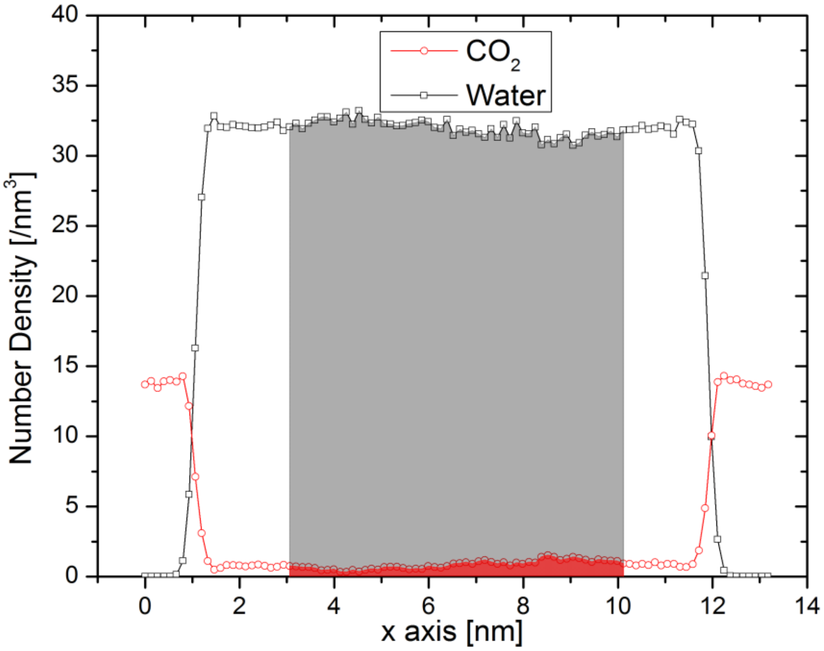

FIG. 22. Number density profile of carbon dioxide and water in the CWC system. The red area represents the number of carbon dioxide molecules in the volume between 3 and 10 nm of the x axis. The sum of the red and grey areas gives the number water molecules in the same region.

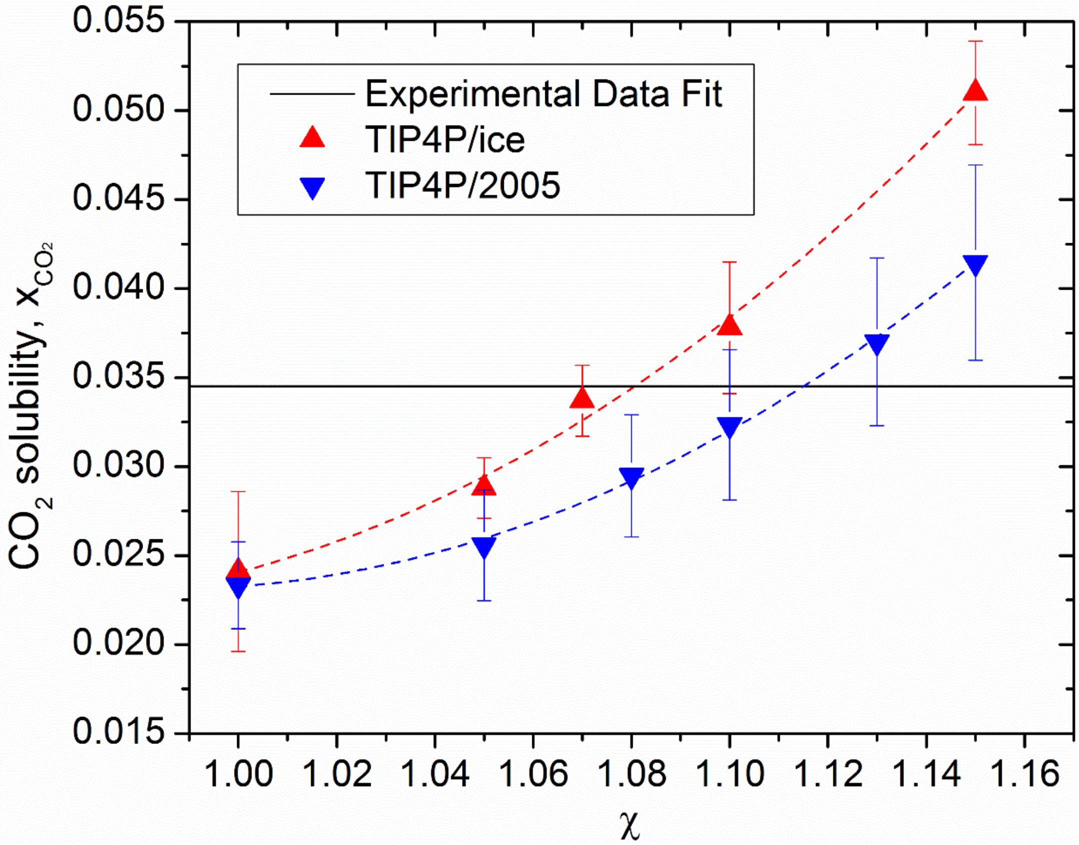

FIG. 23. Dependence of the carbon dioxide solubility (mole fraction) on the modification factor of the LB cross-interaction energy parameter for the case of TIP4P/ice (red up triangles) and TIP4P/2005 (blue down triangles) at 400 bar and 286 K. The solid black line depicts the experimental solubility.[179]

5.2.4 Calculation of T_3 Using Modified Parameters

Given this result, we repeated the calculations of T_3 of the carbon dioxide hydrate system for TIP4P/Ice using the modification parameter $\chi = 1.08$. The results are given in Table VI and are additionally presented in FIG. 24.

The correction of the carbon dioxide solubility has a pronounced effect on the calculated T_3 values, which shift towards the experimental ones. With the exception of the points at 20 bar (discussed in section 5.2.5), the deviations of the calculated T_3 after implementing the χ factor for the TIP4P/ice with TraPPE force field combination from the experimental values range from -3.2 K up to -2.2 K. This result is consistent with the finding of our earlier study for the methane hydrate system,[153] that the deviation of the T_3 is dictated by the deviation of the predicted melting temperature of ice of TIP4P/ice water force field.

In order to clarify the relative importance of the water – water and water – guest interactions in the determination of T_3, the procedure was repeated using the TIP4P/2005 water force field while keeping the TraPPE model for the carbon dioxide. TIP4P/2005 is a particularly popular water model since it provides a good description of many water properties.[180] Nevertheless, contrary to TIP4P/ice, it predicts a melting temperature for ice with a value of 250.5(3) K, which is 22.65 K below the experimental value. In this sense, the TIP4P/2005 can provide a quantitate assessment of the importance of the water–water interaction in the calculation of T_3. Thus, we calculated T_3 using the TIP4P/2005 with the standard LB rules, we subsequently found an optimized value of the cross-interaction energy parameter between the oxygen of water and the oxygen atoms of carbon dioxide targeting the experimental solubility of carbon dioxide in water, and finally, we used this optimized modification parameter to recalculate T_3. We restricted these simulations in the liquid carbon dioxide region since the expected values for the H-L_w-V_{CO_2} equilibrium using the TIP4P/2005 force field are to the right of the saturation curve of carbon dioxide (see FIG. 24), so the phase of the carbon dioxide will be erroneously liquid. The dependence of carbon dioxide solubility in water on the modification parameter is presented in Fig. 23 and the results of the T_3 calculations are presented in Table VI and in FIG. 24.

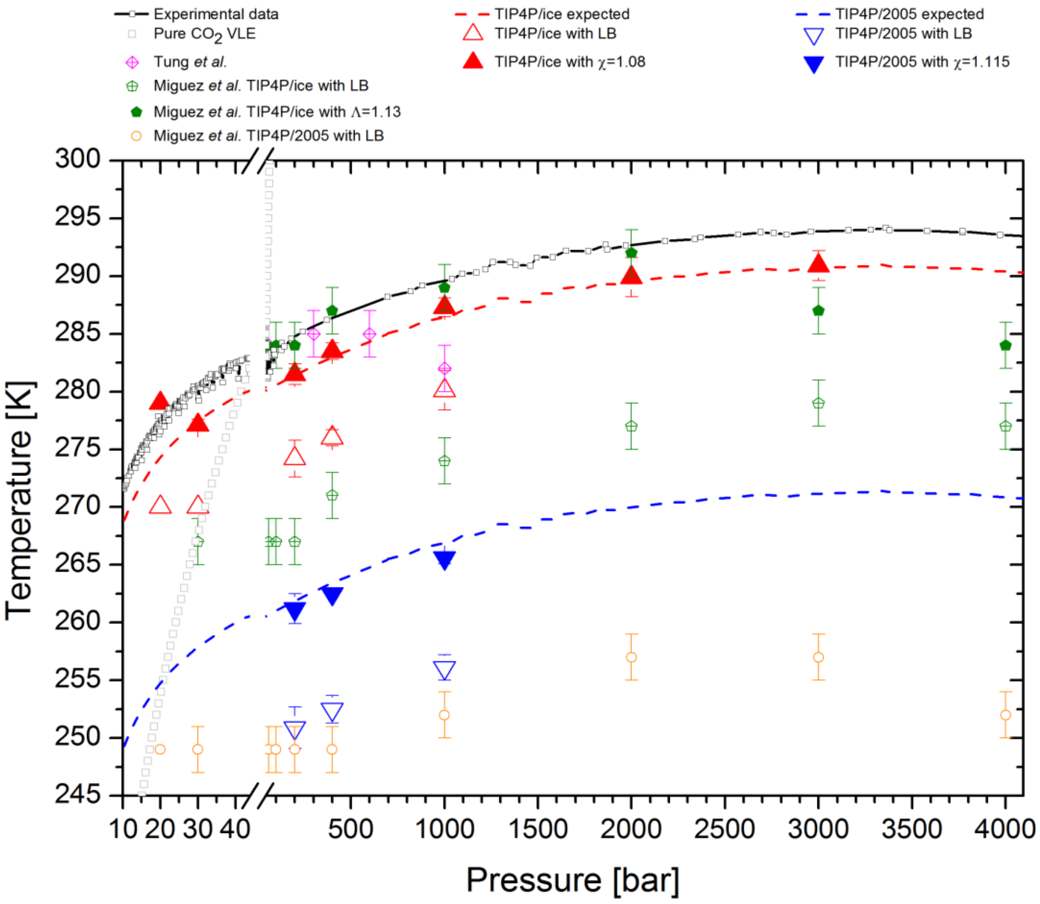

FIG. 24. Experimental and calculated values of T_3 for carbon dioxide hydrates from this work (triangles), from Tung *et al.*[163] (pink diamonds), and from Miguez *et al.*[156] (green pentagons (TIP4P/ice) and orange circles (TIP4P/2005)). The red upside-up triangles represent results obtained using the TIP4P/ice force field, and the blue, upside-down triangles represent results obtained using the TIP4P/2005 force field. Open points indicate the runs were conducted using the LB combining rules, while the filled points indicate that the appropriate modification factor for the force field was applied. The red and blue dashed lines represent the expected values of T_3 for the TIP4P/ice ($T_{3,expected} = T_{3,experimental}$ – 3.15 K) and TIP4P/2005 ($T_{3,expected} = T_{3,experimental}$ – 22.7 K) force fields, respectively. Experimental T_3 line obtained by polynomial fit from data collection of Sloan and Koh.[2] The pure CO_2 saturation points are shown using grey squares.[94]

The use of the TIP4P/2005 force field with the LB combining rules for the determination of T_3 results in systematic deviations with an average value of -33.7 K with respect to the experimental values. This larger deviation than in the case of TIP4P/Ice was expected since ΔT_m of TIP4P/2005 (-22.65 K) is significantly larger than that of TIP4P/Ice (-3.15 K). It is interesting to note that the sum of the deviation in T_3 of TIP4P/2005 is approximately equal to the sum of the deviation in T_3 of TIP4P/Ice and the deviation in melting temperature of TIP4P/2005.

As depicted in Fig. 23, the χ dependence of solubility for TIP4P/2005 is smaller, albeit of the same order of magnitude as in the case of TIP4P/Ice. The value of the modification parameter that minimizes the deviation of the predicted solubility from the experimental value is equal to 1.115. Using this value for the modification parameter for the TIP4P/2005 force field, T_3 was recalculated and the average deviation from the experimental values was found equal to -23.8 K, and thus approximately equal to ΔT_m of TIP4P/2005 (-22.65 K). This result strongly indicates that the accuracy of the prediction of T_3 cannot be improved solely on the grounds of correctly accounting for the water–guest interactions which is performed by correcting the guest solubility in water. In addition, the accuracy is bounded by the limits of the water force field to correctly describe the water–water interactions as these are exhibited macroscopically through the prediction of melting temperature of ice.

In FIG. 24, a comparison is also made between the results of the present study and the work of Tung *et al*.,[163] and Miguez *et al.*[156] The results of Tung *et* *al.*, who used the TIP4P/Ew and EPM2 models with the Lennard-Jones cross interaction parameters reported by Sun and Duan,[165] although close to the experimental values at intermediate pressures, appear to inconsistently deviate for larger pressures.

On the other hand, the results of Miguez *et al*. are in good agreement with the results of this work. The authors conducted a similar study and predicted first the values of T_3 using the TIP4P/ice and TIP4P/2005 force fields for water with TraPPE CO_2 using the LB combining rules, and found that the deviation in the predictions are close to the deviations predicted in this work. They then chose to introduce a modification parameter Λ with the major difference in its definition (compared to χ used in this work) of modifying both σ and ε cross-interactions between the oxygen in water and the oxygen atoms in carbon dioxide (Miguez *et al.* used the notation χ for the modification in their work, but the notation Λ has been used here in order to avoid confusion between the modification factors in their work and in this work, since the two factors are defined differently). They then varied Λ with the target being the correct prediction of T_3 rather than the correct solubility as was done in this work. They found that a value of $\Lambda = 1.13$ results in good agreement with the experimental data at pressures up to 2000 bar, but has a higher deviation from the experimental data at higher pressures.

Despite their work having a different approach in obtaining accurate predictions from ours, there are several key points that are in agreement with our work. First, the results of their work confirm the need for introducing a modification factor to increase the affinity between carbon dioxide and water. Second, their results predict the same slope of the experimental line as was predicted in this work, for both the TIP4P/2005 and TIP4P/ice model, up to 2000 bar. However, the effect of having a higher solubility than the experimental solubility may pose an issue in the future when the prediction of mixed gas hydrates is needed. If a higher solubility of one guest than the experimental value exists in the aqueous phase, preferential enclathration of the incorrect guest may be erroneously predicted. For this reason, in this work the modification of the cross-interaction parameters to achieve the correct solubility was made the target, rather than the modification to obtain the correct value of T_3.

In addition, the results of this work are consistently 3 K below the experimental coexistence temperature for the entire pressure range tested using the modification. In contrast, the work of *Miguez et al.* yields a higher deviation at higher pressures. This fact suggests that the optimization based on the solubility is applicable to a wider range of pressures than the optimization based on T_3.

5.2.5 Inconsistency in Prediction of T_3 at Low Pressure

Unlike the H-L_w-L_{CO_2} T_3 predictions which consistently had approximately -10 and -3 K deviations from the experimental T_3 values for the LB and the modified cross-interactions cases, respectively, the H-L_w-V_{CO_2} equilibrium predictions had inconsistent deviations from the experimental values. At 20 bar, deviations of -7 and +2 K for the LB and the modified cross-interactions cases, respectively, were found, while at 30 bar, deviations of -10 and -3 K for the LB and the modified cross-interactions cases, respectively, were found. While the exact reason for this inconsistency has not been determined in this work, this section outlines some possible reasons for these results.

5.2.5.1 Computational Expense and Box Anisotropy of Low Pressure Simulations

It is important to first clarify that performing simulations at low pressures, where carbon dioxide is in the vapor phase, has a much higher computational cost than the simulations at the higher pressures, where carbon dioxide is in the liquid phase. At low pressures, simulation times in the range of 600 – 2000 ns are required in order to accurately determine whether the system proceeds towards hydrate growth or dissociation, compared to a range of 300 – 1000 ns of simulation time needed for the high pressure runs.

This difference in the kinetic rates of growth and dissociation can be attributed to the large difference in the carbon dioxide solubility in water between low and high pressures and consequently in the concentration of carbon dioxide at the hydrate–water interface. Moreover, the pressure dependence of vapor carbon dioxide solubility in water is much steeper than that of liquid carbon dioxide solubility. As a result, we observed that the simulation time needed for the entire high pressure range (200–1000 bar) was very similar, but the simulations at 20 bar were significantly longer than those at 30 bar.

Additionally, while the y and z box dimensions are dictated by the hydrate supercell and practically remain constant and close to 2.4 nm, the x dimension varied from a range of 22.5 – 52.5 nm for the low pressure runs to a range of 8.5

– 9.0 nm for the high pressure runs. The larger box sizes and higher size range for the low pressure runs were due to the much lower density of the vapor carbon dioxide compared to liquid carbon dioxide, as well as the much stronger dependence of density on pressure and temperature for the vapor phase. The larger systems at the low pressure had a significant, negative effect on the simulation speed. The high computational cost of these simulations was therefore a significant hindrance to making predictions at the low pressures. Also, the very high degree of anisotropy in the box dimensions at the low pressures, with an x dimension that is up to approximately 20 times the y and z dimensions, can possibly cause simulation artifacts that have not been identified in this work.

5.2.5.2 Box Fluctuations at Low Pressures

The low density of vapor carbon dioxide, as well as the adsorption of the vapor carbon dioxide at the water interface (see Fig. 18), causes continuous, relatively large fluctuations of the box length. To illustrate this, Fig. 25 shows the box size in the x dimension as a function of time for the WCW system at 20 bar and 279 K for a 200 ns simulation of the equilibrated system. Due to the dynamic nature of the MD simulation method, carbon dioxide molecules are continuously being exchanged between the bulk vapor and the adsorbed layer. At such low pressures as 20 and 30 bar where the vapor density is very low, the removal of only a few molecules from the vapor phase results in a relatively large decrease in the box length. For example, at 20 bar and 279 K, pure carbon dioxide has a density of 44.0 kg/m^3.[94] At this condition, the exchange of only 10 carbon dioxide molecules from the bulk vapor into the adsorbed layer will cause a decrease of approximately 3 nm in the box length.

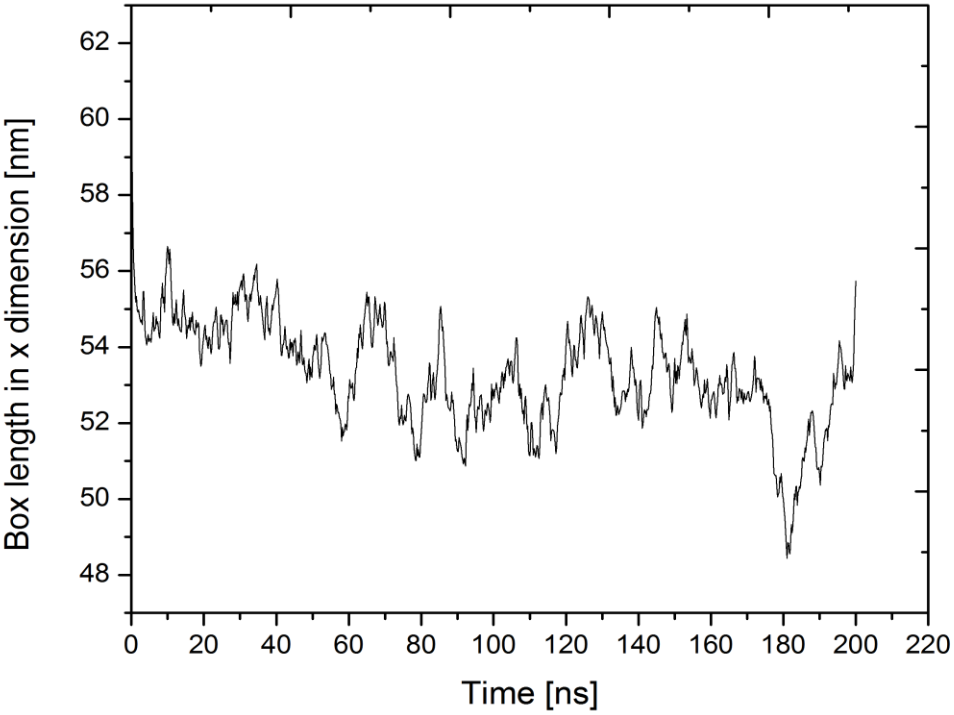

FIG. 25. Box x dimension as a function of time for the WCW system at 20 bar and 279 K.

Such large fluctuations of the box length can be problematic when the pressure coupling is applied. This is because the volume rescaling of the barostat is intended to act in a smooth manner with only minor, periodic adjustments of the box length. However, when such large volume fluctuations are inherent in the system, the use of the barostat can artificially impose large forces on the molecules, which would ultimately result in incorrect predictions. One possible method that may rectify this problem would be the use of a smaller value for τ_P [see Eqn. (28)], such that the coupling is performed at shorter intervals so that significant box length changes are not developed.

5.2.6 Summary of Findings of Carbon Dioxide Hydrate Study

First, it was found that an additional equilibration step is necessary for the WCW system in order to allow for the adsorption of a vapor carbon dioxide layer at the water interface. For this reason, the initial configuration used was modified from the WHWM used for the methane hydrate system, to the equivalent HWCW configuration used for the carbon dioxide hydrate system. Second, the use of the LB combining rules for the calculation of the cross-interactions yielded a consistent deviation for the predictions of T_3 between -9 and -12 K from the experimental values. In addition, the solubility of carbon dioxide in the aqueous phase using these combining rules was measured and found to be underestimated. Third, a modification factor χ was introduced in order to increase the affinity between carbon dioxide and water, and the value of χ was fit to obtain the experimental solubility at 400 bar and 286 K. Using a value of $\chi = 1.08$ for the TIP4P/ice – TraPPE force field combination, the calculation of T_3 was repeated and a consistent deviation of -3 K from the experimental T_3 was found, consistent with the expected deviation dictated by ΔT_m for the TIP4P/Ice water model.

Fourth, in order to generalize these findings, the procedure was repeated for the TIP4P/2005 water force field using a fitted value for $\chi = 1.115$, and a deviation of -23.8 K was found from the experimental T_3 values. This is also consistent with ΔT_m for the TIP4P/2005 water model. It can therefore be concluded that the water-guest interactions must correctly provide the solubility of the guest molecule in the aqueous phase. Once the solubility is correct, the predictions of T_3 are as accurate as the ability of the chosen water force field in predicting the melting of ice.

Finally, the results for the low pressure region, where carbon dioxide exists in the vapor phase, are inconsistent with the findings from the rest of this work. This is probably due to simulation artifacts that arise at such low pressures, as a result of the nature of carbon dioxide at these conditions. This includes the low carbon dioxide density which causes a high level of anisotropy in the box dimensions, as well as the violent fluctuations of the box that may induce unnatural forces that alter the predictions of T_3.

6. CONCLUSIONS AND FUTURE WORK

The direct-phase coexistence methodology was implemented in this work for the determination of the three-phase coexistence conditions of both the methane and the carbon dioxide hydrates using MD simulations. Experimental data exists for a wide range of conditions for both these pure hydrate systems, so the goal was not to simply reproduce existing data, but rather to develop an understanding of the mechanisms and problems involved in the modeling of gas hydrate systems using MD simulations in general. This is the first step towards a trustworthy MD simulation scheme that can be used to generate data for a wide range of clathrate hydrates at conditions where experimental data is scarce.

As such, several important insights have been discussed in this work. From the study of methane hydrates, the stochastic nature of the hydrate system became apparent. This necessitated the inclusion of a statistical analysis in the well-established direct-phase coexistence method. The statistical analysis involved performing multiple independent runs at every condition of temperature and pressure, in order to obtain consistent results for T_3. In addition, it was shown that a time length of 1000 – 4000 ns was needed in order to reach accurate conclusions about the final state of the system (i.e., growth or dissociation). It was additionally observed that the supersaturated conditions that can occur during this kind of simulations can affect the calculated T_3. For this reason in all the simulations for the determination of T_3 in this study, the instantaneous development of a methane bubble was avoided by using an adequate number of molecules in the guest slab.

The aforementioned procedure resulted in the determination of T_3 with a high level of accuracy. It was found that for the TIP4P/Ice water model that was used in the methane hydrate study in combination with the OPLS-UA force field for methane, the MD results follow the same trend as the experimental values and have excellent agreement with the expected T_3 which is consistently 3.15 K below the experimental. This difference was expected in accordance with the work of Conde and Vega and is attributed to the difference in the prediction by the TIP4P/Ice water force field of the melting temperature of ice from the respective experimental value.

Another problem that was explored in depth in this work is the effect of erroneously including dispersion tail corrections for such anisotropic and inhomogeneous systems in combination with the pressure coupling scheme. The work confirmed that including such corrections would result in a large error in the density of the guest slab, so dispersion tail corrections must be avoided for such systems.

Finally, the accuracy of the predictions of the water – methane interactions was confirmed by calculating the solubility of methane in the liquid water along the three-phase coexistence line and good agreement was found with two different continuum scale models.

All the lessons learned from the methane hydrates study were then applied to the calculation of the carbon dioxide hydrate three-phase coexistence line. Extensive MD simulations were carried out using the TraPPE model for the description of carbon dioxide and both the TIP4P/Ice and TIP4P/2005 models for the description of water.

By using the classic LB combining rules resulted, the calculation of T_3 yielded large deviations for both models. By correcting the solubility of carbon dioxide in water, through the modification of the cross-interaction Lennard-Jones energy parameter between the oxygen of water and the oxygen atoms of carbon dioxide, the calculated T_3 values shifted considerably in the correct direction. The deviations of T_3 for both cases were found to be equal to the respective deviation from the experimental values of the prediction of the melting temperature of ice for each water model, in agreement with the results obtained from the study of the methane hydrate.

These results strongly indicate that both water–water and water–guest interactions hold a prominent role in the determination of T_3 with the direct-phase coexistence methodology. This fact provides evidence to the statement that the value of T_3 can be successfully predicted with the direct-phase coexistence method using a water force field that correctly predicts the melting temperature of ice, and in combination with a guest force field that correctly accounts for the guest solubility in the water phase.

Having successfully obtained results for the pure hydrate systems, there are several directions that can be followed in the future in order to further our understanding of all the problems associated with the direct-phase coexistence method. First, a thorough investigation into the causes of the inconsistency in the prediction of the three-phase equilibrium line at low pressures for the carbon dioxide hydrate should yield information about other artifacts that must be accounted for when simulating clathrate hydrates. Second, the investigation of the methane – carbon dioxide mixed hydrate would be a reasonable starting point for understanding the factors that influence simulations of mixed guests. Third, the power of MD in studying dynamic systems was not exploited in this work through the quantitative measurement of the kinetic rates involved in hydrate growth and dissociation. It would therefore be interesting to calculate these rates for the simulated systems, and compare the measured rates with reported experimental data.

REFERENCES

(1) Davy, H. *Philos. Trans. R. Soc. London* **1811**, *101*, 1–35.

(2) Sloan, E. D.; Koh, C. A. *Clathrate hydrates of natural gases*; 3rd ed.; CRC Press, Taylor and Francis Group, 2008.

(3) Hammerschmidt, E. G. *Ind. Eng. Chem.* **1934**, *26*, 851–855.

(4) Kelland, M. A. *Energy & Fuels* **2006**, *20*, 825–847.

(5) Englezos, P. *Ind. Eng. Chem. Res.* **1993**, *32*, 1251–1274.

(6) Koh, C. A. *Chem. Soc. Rev.* **2002**, *31*, 157–167.

(7) Mao, W. L.; Mao, H. K.; Goncharov, A. F.; Struzhkin, V. V; Guo, Q.; Hu, J.; Shu, J.; Hemley, R. J.; Somayazulu, M.; Zhao, Y. *Science* **2002**, *297*, 2247–2249.

(8) Papadimitriou, N. I.; Tsimpanogiannis, I. N.; Papaioannou, A. T.; Stubos, A. K. *J. Phys. Chem. C* **2008**, *112*, 10294–10302.

(9) Papadimitriou, N. I.; Tsimpanogiannis, I. N.; Peters, C. J.; Papaioannou, A. T.; Stubos, A. K. *J. Phys. Chem. B* **2008**, *112*, 14206–14211.

(10) Mao, W. L.; Mao, H.-K. *Proc. Natl. Acad. Sci. U. S. A.* **2004**, *101*, 708–710.

(11) Papadimitriou, N. I.; Tsimpanogiannis, I. N.; Stubos, A. K. *Colloids Surfaces A Physicochem. Eng. Asp.* **2010**, *357*, 67–73.

(12) Khokhar, A. A.; Gudmundsson, J. S.; Sloan, E. D. *Fluid Phase Equilib.* **1998**, *150-151*, 383–392.

(13) Dabrowski, N.; Windmeier, C.; Oellrich, L. R. *Energy & Fuels* **2009**, *23*, 5603–5610.

(14) Zhong, D. L.; Daraboina, N.; Englezos, P. *Fuel* **2013**, *106*, 425–430.

(15) Kang, S. P.; Lee, H. *Environ. Sci. Technol.* **2000**, *34*, 4397–4400.

(16) Seo, Y. T.; Moudrakovski, I. L.; Ripmeester, J. A.; Lee, J.; Lee, H. *Environ. Sci. Technol.* **2005**, *39*, 2315–2319.

(17) Adeyemo, A.; Kumar, R.; Linga, P.; Ripmeester, J.; Englezos, P. *Int. J. Greenh. Gas Control* **2010**, *4*, 478–485.

(18) Eslamimanesh, A.; Mohammadi, A. H.; Richon, D.; Naidoo, P.; Ramjugernath, D. *J. Chem. Thermodyn.* **2012**, *46*, 62–71.

(19) Kubota, H.; Shimizu, K.; Tanaka, Y.; Makita, T. *J. Chem. Eng. Japan* **1984**, *17*, 423–429.

(20) Park, K. N.; Hong, S. Y.; Lee, J. W.; Kang, K. C.; Lee, Y. C.; Ha, M. G.; Lee, J. D. *Desalination* **2011**, *274*, 91–96.

(21) Sloan, E. D. *Am. Mineral.* **2004**, *89*, 1155–1161.

(22) Van der Waals, J. H.; Platteeuw, J. C. *Adv. Chem. Phys.* **1959**, *2*, 1–57.

(23) Bozhko, Y. Y.; Subbotin, O. S.; Fomin, V. M.; Belosludov, V. R.; Kawazoe, Y. *J. Eng. Thermophys.* **2014**, *23*, 9–19.

(24) Holder, G. D.; Zetts, S. P.; Pradhan, N. *Rev. Chem. Eng.* **1988**, *5*, 1–70.

(25) Ballard, A. L.; Sloan, E. D. *Fluid Phase Equilib.* **2004**, *218*, 15–31.

(26) Ballard, A. L.; Sloan, E. D. *Fluid Phase Equilib.* **2002**, *194*, 371–383.

(27) Parrish, W. R.; Prausnitz, J. M. *Ind. Eng. Chem. Process Des. Dev.* **1972**, *11*, 26–35.

(28) Dufal, S.; Galindo, A.; Jackson, G.; Haslam, A. J. *Mol. Phys.* **2012**, *110*, 1223–1240.

(29) Klauda, J. B.; Sandler, S. I. *Energy & Fuels* **2005**, *19*, 459–470.

(30) Kvenvolden, K. A. *Rev. Geophys.* **1993**, *31*, 173–187.

(31) Burwicz, E. B.; Rüpke, L. H.; Wallmann, K. *Geochim. Cosmochim. Acta* **2011**, *75*, 4562–4576.

(32) Milkov, A. V. *Earth-Science Rev.* **2004**, *66*, 183–197.

(33) Piñero, E.; Marquardt, M.; Hensen, C.; Haeckel, M.; Wallmann, K. *Biogeosciences* **2013**, *10*, 959–975.

(34) Lee, S.-Y.; Holder, G. D. *Fuel Process. Technol.* **2001**, *71*, 181–186.

(35) Makogon, Y. F.; Holditch, S. a.; Makogon, T. Y. *J. Pet. Sci. Eng.* **2007**, *56*, 14–31.

(36) Boswell, R.; Collett, T. S. *Energy Environ. Sci.* **2011**, *4*, 1206.

(37) Walsh, M. R.; Hancock, S. H.; Wilson, S. J.; Patil, S. L.; Moridis, G. J.; Boswell, R.; Collett, T. S.; Koh, C. a.; Sloan, E. D. *Energy Econ.* **2009**, *31*, 815–823.

(38) Moridis, G.; Collett, T.; Boswell, R.; Kurihara, M.; Reagan, M.; Koh, C.; Sloan, E. *SPE Reserv. Eval. Eng.* **2009**, *12*, 745–771.

(39) Kvenvolden, K. A. *Proc. Natl. Acad. Sci. U. S. A.* **1999**, *96*, 3420–3426.

(40) Archer, D.; Buffett, B.; Brovkin, V. *Proc. Natl. Acad. Sci. U. S. A.* **2009**, *106*, 20596–20601.

(41) Kukowski, N.; Greinert, J.; Henrys, S. *Mar. Geol.* **2010**, *272*, 141–153.

(42) Maslin, M.; Owen, M.; Betts, R.; Day, S.; Dunkley Jones, T.; Ridgwell, A. *Philos. Trans. A. Math. Phys. Eng. Sci.* **2010**, *368*, 2369–2393.

(43) Marchetti, C. *Clim. Change* **1977**, *1*, 59–68.

(44) Kvamme, B.; Tanaka, H. *J. Phys. Chem.* **1995**, *99*, 7114–7119.

(45) Ohgaki, K.; Takano, K.; Moritoki, M. *Kagaku Kogaku Ronbunshu* **1994**, *20*, 121–123.

(46) Ohgaki, K.; Takano, K.; Sangawa, H.; Matsubara, T.; Nakano, S. *J. Chem. Eng. Japan* **1996**, *29*, 478–483.

(47) Lee, H.; Seo, Y.; Seo, Y. T.; Moudrakovski, I. L.; Ripmeester, J. A. *Angew. Chemie - Int. Ed.* **2003**, *42*, 5048–5051.

(48) Takahashi, T.; Sato, T.; Inui, M.; Hirabayashi, S.; Brumby, P. E. *Chem. Eng. Technol.* **2012**, *35*, 1751–1758.

(49) Zhang, Y.; Xiong, L. J.; Li, X. Sen; Chen, Z. Y.; Xu, C. G. *Chem. Eng. Technol.* **2014**, *37*, 2022–2029.

(50) Zhao, J.; Xu, K.; Song, Y.; Liu, W.; Lam, W.; Liu, Y.; Xue, K.; Zhu, Y.; Yu, X.; Li, Q. *Energies* **2012**, *5*, 399–419.

(51) Ota, M.; Morohashi, K.; Abe, Y.; Watanabe, M.; Smith, R. L.; Inomata, H. *Energy Convers. Manag.* **2005**, *46*, 1680–1691.

(52) Ota, M.; Abe, Y.; Watanabe, M.; Smith, R. L.; Inomata, H. *Fluid Phase Equilib.* **2005**, *228*, 553–559.

(53) Komatsu, H.; Ota, M.; Smith, R. L.; Inomata, H. *J. Taiwan Inst. Chem. Eng.* **2013**, *44*, 517–537.

(54) Park, Y.; Kim, D. Y.; Lee, J. W.; Huh, D. G.; Park, K. P.; Lee, J.; Lee, H. *Proc. Natl. Acad. Sci. U. S. A.* **2006**, *103*, 12690–12694.

(55) Kvamme, B.; Graue, A.; Buanes, T.; Kuznetsova, T.; Ersland, G. *Int. J. Greenh. Gas Control* **2007**, *1*, 236–246.

(56) Kvamme, B.; Graue, A.; Aspenes, E.; Kuznetsova, T.; Granasy, L.; Toth, G.; Pusztai, T.; Tegze, G. *Phys. Chem. Chem. Phys.* **2004**, *6*, 2327–2334.

(57) Ning, F. L.; Glavatski, K.; Ji, Z.; Kjelstrup, S.; Vlugt, T. J. H. *Phys. Chem. Chem. Phys.* **2015**, *17*, 2869–2883.

(58) Bai, D.; Zhang, X.; Chen, G.; Wang, W. *Energy Environ. Sci.* **2012**, *5*, 7033–7041.

(59) Yi, L.; Liang, D.; Zhou, X.; Li, D. *J. Energy Chem.* **2014**, *23*, 747–754.

(60) Iwai, Y.; Nakamura, H.; Hirata, M. *Mol. Simul.* **2012**, *38*, 481–490.

(61) Tegze, G.; Pusztai, T.; Tóth, G.; Gránásy, L.; Svandal, A.; Buanes, T.; Kuznetsova, T.; Kvamme, B. *J. Chem. Phys.* **2006**, *124*, 234710.

(62) Qi, Y.; Ota, M.; Zhang, H. *Energy Convers. Manag.* **2011**, *52*, 2682–2687.

(63) Svandal, A.; Kuznetsova, T.; Kvamme, B. *Fluid Phase Equilib.* **2006**, *246*, 177–184.

(64) Wang, X.; Sang, D. K.; Chen, J.; Mi, J. *Phys. Chem. Chem. Phys.* **2014**, *16*, 26929–26937.

(65) Hatakeyama, T.; Aida, E.; Yokomori, T.; Ohmura, R.; Ueda, T. *Ind. Eng. Chem. Res.* **2009**, *48*, 4083–4087.

(66) Gupta, A.; Dimmel, B. C. *Carbon dioxide-hydrate product and method of manufacture thereof*; The Coca-Cola Company (Atlanta, GA), United States, 2005.

(67) Li, S.; Shen, Y.; Liu, D.; Fan, L.; Tan, Z. *Chem. Eng. Res. Des.* **2015**, *93*, 773–778.

(68) Bayraktar, E.; Kocapiçak, Ö.; Mehmetoğlu, Ü.; Parlaktuna, M.; Mehmetoğlu, T. *Chem. Eng. Res. Des.* **2008**, *86*, 209–213.

(69) Ladd, A. J. C.; Woodcock, L. V. *Chem. Phys. Lett.* **1977**, *51*, 155–159.

(70) Metropolis, N.; Rosenbluth, A. W.; Rosenbluth, M. N.; Teller, A. H. *J. Chem. Phys.* **1953**, *21*, 1087–1092.

(71) Frenkel, D.; Smit, B. *Understanding molecular simulation: from algorithms to applications*; Academic press, 2001; Vol. 1.

(72) Alder, B.; Wainwright, T. *J. Chem. Phys.* **1957**, *27*, 1208–1211.

(73) Rahman, A. *Phys. Rev. A* **1964**, *136*, 405–411.

(74) Verlet, L. *Phys. Rev.* **1967**, *159*, 98–103.

(75) Verlet, L. *Phys. Rev.* **1968**, *165*, 201–214.

(76) Prausnitz, J. M.; Lichtenthaler, R. N.; de Azevedo, E. G. *Molecular thermodynamics of fluid-phase equilibria*; Pearson Education, 1998.

(77) Lindahl, E.; van der Spoel, D.; Hess, B. 2007.

(78) Atkins, P.; de Paul, J. *Atkins' Physical Chemistry*; Oxford University Press, 2010.

(79) Allen, M. P.; Tildesley, D. J. *Computer simulation of liquids*; Oxford Science Publications, 1991; Vol. 57.

(80) Ewald, P. P. *Ann. Phys.* **1921**, *369*, 253–287.

(81) Verlet, L. *Phys. Rev.* **1967**, *159*, 98–103.

(82) Hockney, R. W.; Eastwood, J. W. *Computer simulation using particles*; McGraw-Hill: New York, 1981.

(83) Van der Spoel, D.; Lindahl, E.; Hess, B.; Groenhof, G.; Mark, A. E.; Berendsen, H. J. C. *J. Comput. Chem.* **2005**, *26*, 1701–1718.

(84) Hess, B.; Kutzner, C.; van der Spoel, D.; Lindahl, E. *J. Chem. Theory Comput.* **2008**, *4*, 435–447.

(85) Pronk, S.; Pall, S.; Larsson, P.; Bjelkmar, P.; Apostolov, R.; Shirts, M. R.; Smith, J. C.; Kasson, P. M.; van der Spoel, D.; Hess, B.; Lindahl, E. *Bioinformatics* **2013**, *29*, 845–854.

(86) Berendsen, H. J. C.; Postma, J. P. M.; van Gunsteren, W. F.; DiNola, A.; Haak, J. R. *J. Chem. Phys.* **1984**, *81*, 3684–3690.

(87) Sloan, E. D. *Nature* **2003**, *426*, 353–363.

(88) Jacobson, L. C.; Hujo, W.; Molinero, V. *J. Phys. Chem. B* **2009**, *113*, 10298–10307.

(89) Falenty, A.; Hansen, T. C.; Salamatin, A. N.; Kuhs, W. F. In *Proceedings of the International Conference on Gas Hydrates (ICGH8)*; Beijing, China; p. Paper No. T1–T123.

(90) Conde, M. M.; Vega, C.; Tribello, G. a.; Slater, B. *J. Chem. Phys.* **2009**, *131*.

(91) Papadimitriou, N. I.; Tsimpanogiannis, I. N.; Papaioannou, A. T.; Stubos, A. K. *Mol. Simul.* **2008**, *34*, 1311–1320.

(92) Chou, I. M.; Sharma, A.; Burruss, R. C.; Shu, J.; Mao, H.; Hemley, R. J.; Goncharov, a F.; Stern, L. A.; Kirby, S. H. *Proc. Natl. Acad. Sci. U. S. A.* **2000**, *97*, 13484–13487.

(93) Loveday, J. S.; Nelmes, R. J. *Phys. Chem. Chem. Phys.* **2008**, *10*, 937–950.

(94) Lemmon, E. W.; McLinden, M. O.; Friend, D. G. In *NIST Chemistry WebBook, NIST Standard Reference Database Number 69*; Linstrom, P. J.; Mallard, W. G., Eds.; National Institute of Standards and Technology: Gaithersburg MD, 2014.

(95) Guillot, B. *J. Mol. Liq.* **2002**, *101*, 219–260.

(96) Bernal, J. D.; Fowler, R. H. *J. Chem. Phys.* **1933**, *1*, 515–548.

(97) Berendsen, H. J. C.; Postma, J. P. M.; van Gunsteren, W. F.; Hermans, J. *Intermolecular Forces*; Pullman, B., Ed.; Reidel Publishing, 1981.

(98) Berendsen, H. J. C.; Grigera, J. R.; Straatsma, T. P. *J. Phys. Chem.* **1987**, *91*, 6269–6271.

(99) Jorgensen, W. L.; Chandrasekhar, J.; Madura, J. D.; Impey, R. W.; Klein, M. L. *J. Chem. Phys.* **1983**, *79*, 926.

(100) Lie, G.; Clementi, E. *Phys. Rev. A* **1986**, *33*, 2679–2693.

(101) Toukan, K.; Rahman, A. *Phys. Rev. B* **1985**, *31*, 2643–2648.

(102) Ahlstrom, P.; Wallqvist, A.; Engstrom, S.; Jonsson, B. *Mol. Phys.* **1989**, *68*, 563–581.

(103) Sprik, M. *J. Phys. Chem.* **1991**, *95*, 2283–2291.

(104) Jorgensen, W. L.; Maxwell, D. S.; Tirado-Rives, J. *J. Am. Chem. Soc.* **1996**, *118*, 11225–11236.

(105) Jorgensen, W. L.; Madura, J. D.; Swenson, C. J. *J. Am. Chem. Soc.* **1984**, *106*, 6638–6646.

(106) Martin, M. G.; Siepmann, J. I. *J. Phys. Chem. B* **1998**, *102*, 2569–2577.

(107) Potoff, J. J.; Siepmann, J. I. *AIChE J.* **2001**, *47*, 1676–1682.

(108) Murthy, C. S.; Singer, K.; McDonald, I. R. *Mol. Phys.* **1981**, *44*, 135–143.

(109) Moller, D.; Fischer, J. *Fluid Phase Equilib.* **1994**, *100*, 35–61.

(110) Murthy, C. S.; O'Shea, S. F.; McDonald, I. R. *Mol. Phys.* **1983**, *50*, 531–541.

(111) Zhang, Z.; Duan, Z. *J. Chem. Phys.* **2005**, *122*, 214507.

(112) Potoff, J. J.; Errington, J. R.; Panagiotopoulos, A. Z. *Mol. Phys.* **1999**, *97*, 1073–1083.

(113) Sum, A. K.; Wu, D. T.; Yasuoka, K. *MRS Bull.* **2011**, *36*, 205–210.

(114) Barnes, B. C.; Sum, A. K. *Curr. Opin. Chem. Eng.* **2013**, *2*, 184–190.

(115) English, N. J.; MacElroy, J. M. D. *Chem. Eng. Sci.* **2015**, *121*, 133–156.

(116) Tse, J. S.; Klein, M. L.; McDonald, I. R. *J. Phys. Chem.* **1983**, *87*, 4198–4203.

(117) Walsh, M. R.; Koh, C. A.; Sloan, E. D.; Sum, A. K.; Wu, D. T. *Science.* **2009**, *326*, 1095–1098.

(118) Moon, C.; Hawtin, R. W.; Rodger, P. M. *Faraday Discuss.* **2007**, *136*, 367–382.

(119) Radhakrishnan, R.; Trout, B. L. *J. Chem. Phys.* **2002**, *117*, 1786–1796.

(120) Jimenez-Angeles, F.; Firoozabadi, A. *J. Phys. Chem. C* **2014**, *118*, 11310–11318.

(121) Sarupria, S.; Debenedetti, P. G. *J. Phys. Chem. Lett.* **2012**, *3*, 2942–2947.

(122) Walsh, M. R.; Beckham, G. T.; Koh, C. A.; Sloan, E. D.; Wu, D. T.; Sum, A. K. *J. Phys. Chem. C* **2011**, *115*, 21241–21248.

(123) Guo, G. J.; Zhang, Y. G.; Liu, C. J.; Li, K. H. *Phys. Chem. Chem. Phys.* **2011**, *13*, 12048–12057.

(124) Vatamanu, J.; Kusalik, P. G. *J. Chem. Phys.* **2007**, *126*, 124703.

(125) Moon, C.; Taylor, P. C.; Rodger, P. M. *J. Am. Chem. Soc.* **2003**, *125*, 4706–4707.

(126) English, N. J.; Clarke, E. T. *J. Chem. Phys.* **2013**, *139*, 094701.

(127) Yan, K.; Li, X.; Chen, Z.; Li, B.; Xu, C. *Mol. Simul.* **2012**, *39*, 251–260.

(128) Myshakin, E. M.; Jiang, H.; Warzinski, R. P.; Jordan, K. D. *J. Phys. Chem. A* **2009**, *113*, 1913–1921.

(129) Bagherzadeh, S. A.; Alavi, S.; Ripmeester, J. A.; Englezos, P. *Fluid Phase Equilib.* **2013**, *358*, 114–120.

(130) Yagasaki, T.; Matsumoto, M.; Andoh, Y.; Okazaki, S.; Tanaka, H. *J. Phys. Chem. B* **2014**, *118*, 1900–1906.

(131) Alavi, S.; Ripmeester, J. A. *J. Chem. Phys.* **2010**, *132*, 144703.

(132) Rodger, P. M. *Ann. N. Y. Acad. Sci.* **2000**, *912*, 474–482.

(133) Anderson, B. J.; Tester, J. W.; Borghi, G. P.; Trout, B. L. *J. Am. Chem. Soc.* **2005**, *127*, 17852–17862.

(134) Duffy, D. M.; Moon, C.; Rodger, P. M. *Mol. Phys.* **2004**, *102*, 203–210.

(135) Moon, C.; Taylor, P. C.; Rodger, P. M. *Can. J. Phys.* **2003**, *81*, 451–457.

(136) Baghel, V. S.; Kumar, R.; Roy, S. *J. Phys. Chem. C* **2013**, *117*, 12172–12182.

(137) English, N. J.; Phelan, G. *J. Chem. Phys.* **2009**, *131*, 074704.

(138) English, N. J.; Tse, J. S. *Phys. Rev. Lett.* **2009**, *103*, 015901.

(139) Phan, A.; Cole, D. R.; Striolo, A. *J. Phys. Chem. C* **2014**, *118*, 4860–4868.

(140) Bagherzadeh, S. A.; Englezos, P.; Alavi, S.; Ripmeester, J. A. *J. Phys. Chem. B* **2012**, *116*, 3188–3197.

(141) Liang, S.; Rozmanov, D.; Kusalik, P. G. *Phys. Chem. Chem. Phys.* **2011**, *13*, 19856–19864.

(142) Cygan, R. T.; Guggenheim, S.; van Groos, A. F. *J. Phys. Chem. B* **2004**, *108*, 15141–15149.

(143) Geng, C.-Y.; Wen, H.; Zhou, H. *J. Phys. Chem. A* **2009**, *113*, 5463–5469.

(144) Qi, Y.; Ota, M.; Zhang, H. *Energy Convers. Manag.* **2011**, *52*, 2682–2687.

(145) Jiang, H.; Myshakin, E. M.; Jordan, K. D.; Warzinski, R. P. *J. Phys. Chem. B* **2008**, *112*, 10207–10216.

(146) English, N. J. *Mol. Phys.* **2008**, *106*, 1887–1898.

(147) Rosenbaum, E. J.; English, N. J.; Johnson, J. K.; Shaw, D. W.; Warzinski, R. P. *J. Phys. Chem. B* **2007**, *111*, 13194–13205.

(148) Conde, M. M.; Vega, C. *J. Chem. Phys.* **2010**, *133*, 064507.

(149) Jensen, L.; Thomsen, K.; von Solms, N.; Wierzchowski, S.; Walsh, M. R.; Koh, C. a; Sloan, E. D.; Wu, D. T.; Sum, A. K. *J. Phys. Chem. B* **2010**, *114*, 5775–5782.

(150) Tung, Y. T.; Chen, L. J.; Chen, Y. P.; Lin, S. T. *J. Phys. Chem. B* **2010**, *114*, 10804–10813.

(151) Finney, A. R.; Rodger, P. M. *Phys. Chem. Chem. Phys.* **2011**, *13*, 19979–19987.

(152) Smirnov, G. S.; Stegailov, V. V. *J. Chem. Phys.* **2012**, *136*, 044523.

(153) Michalis, V. K.; Costandy, J.; Tsimpanogiannis, I. N.; Stubos, A. K.; Economou, I. G. *J. Chem. Phys.* **2015**, *142*, 044501.

(154) García Fernández, R.; Abascal, J. L. F.; Vega, C. *J. Chem. Phys.* **2006**, *124*, 144506.

(155) Conde, M. M.; Vega, C. *J. Chem. Phys.* **2013**, *138*, 056101.

(156) Míguez, J. M.; Conde, M. M.; Torré, J.-P.; Blas, F. J.; Piñeiro, M. M.; Vega, C. *J. Chem. Phys.* **2015**, *142*, 124505.

(157) Abascal, J. L. F.; Sanz, E.; García Fernández, R.; Vega, C. *J. Chem. Phys.* **2005**, *122*, 234511.

(158) Abascal, J. L. F.; Vega, C. *J. Chem. Phys.* **2005**, *123*, 234505.

(159) Horn, H. W.; Swope, W. C.; Pitera, J. W.; Madura, J. D.; Dick, T. J.; Hura, G. L.; Head-Gordon, T. *J. Chem. Phys.* **2004**, *120*, 9665–9678.

(160) Cao, Z.; Tester, J. W.; Sparks, K. A.; Trout, B. L. *J. Phys. Chem. B* **2001**, *105*, 10950–10960.

(161) Guillot, B.; Guissani, Y. *J. Chem. Phys.* **1993**, *99*, 8075.

(162) Sarupria, S.; Debenedetti, P. G. *J. Phys. Chem. A* **2011**, *115*, 6102–6111.

(163) Tung, Y. T.; Chen, L. J.; Chen, Y. P.; Lin, S. T. *J. Phys. Chem. C* **2011**, *115*, 7504–7515.

(164) Harris, J. G.; Yung, K. H. *J. Phys. Chem.* **1995**, *99*, 12021–12024.

(165) Sun, R.; Duan, Z. H. *Geochim. Cosmochim. Acta* **2005**, *69*, 4411–4424.

(166) Manakov, A. Y.; Dyadin, Y. A.; Ogienko, A. G.; Kurnosov, A. V; Aladko, E. Y.; Larionov, E. G.; Zhurko, F. V; Voronin, V. I.; Berger, I. F.; Goryainov, S.

V; Lihacheva, A. Y.; Ancharov, A. I. *J. Phys. Chem. B* **2009**, *113*, 7257–7262.

(167) Hirai, H.; Komatsu, K.; Honda, M.; Kawamura, T.; Yamamoto, Y.; Yagi, T. *J. Chem. Phys.* **2010**, *133*, 124511.

(168) McMullan, R. K.; Jeffrey, G. A. *J. Chem. Phys.* **1965**, *42*, 2725–2731.

(169) Essmann, U.; Perera, L.; Berkowitz, M. L.; Darden, T.; Lee, H.; Pedersen, L. G. *J. Chem. Phys.* **1995**, *103*, 8577.

(170) Moridis, G. J. *SPE J.* **2003**, *8*, 359–370.

(171) Espinosa, J. R.; Sanz, E.; Valeriani, C.; Vega, C. *J. Chem. Phys.* **2013**, *139*, 144502.

(172) Duan, Z.; Mao, S. *Geochim. Cosmochim. Acta* **2006**, *70*, 3369–3386.

(173) Tsimpanogiannis, I. N.; Economou, I. G.; Stubos, A. K. *Fluid Phase Equilib.* **2014**, *371*, 106–120.

(174) Docherty, H.; Galindo, A.; Vega, C.; Sanz, E. *J. Chem. Phys.* **2006**, *125*, 074510.

(175) Reed, S. K.; Westacott, R. E. *Phys. Chem. Chem. Phys.* **2008**, *10*, 4614–4622.

(176) Lehmkuhler, F.; Paulus, M.; Sternemann, C.; Lietz, D.; Venturini, F.; Gutt, C.; Tolan, M. *J. Am. Chem. Soc.* **2009**, *131*, 585–589.

(177) Zhang, H.; Singer, S. J. *J. Phys. Chem. A* **2011**, *115*, 6285–6296.

(178) Orozco, G. A.; Economou, I. G.; Panagiotopoulos, A. Z. *J. Phys. Chem. B* **2014**, *118*, 11504–11511.

(179) Duan, Z.; Sun, R.; Zhu, C.; Chou, I. M. *Mar. Chem.* **2006**, *98*, 131–139.

(180) Vega, C.; Abascal, J. L. F. *Phys. Chem. Chem. Phys.* **2011**, *13*, 19663–19688.

APPENDIX A: METHANE HYDRATE TEMPERATURE SCANS

In this section, the potential energy evolution for the multiple seeds at each pressure and temperature condition tested for the methane hydrate system is presented. Each of the following pages includes the potential energy evolution through time of all the independent runs conducted at each temperature for a given pressure. This is followed by a table showing the final state of each independent run, which is denoted as (*g*) for hydrate growth, (*s*) for a stable potential energy, or (*d*) for hydrate dissociation. The title of each plot has the following format: “WHWM, pressure (P = …), temperature (T = …)”.

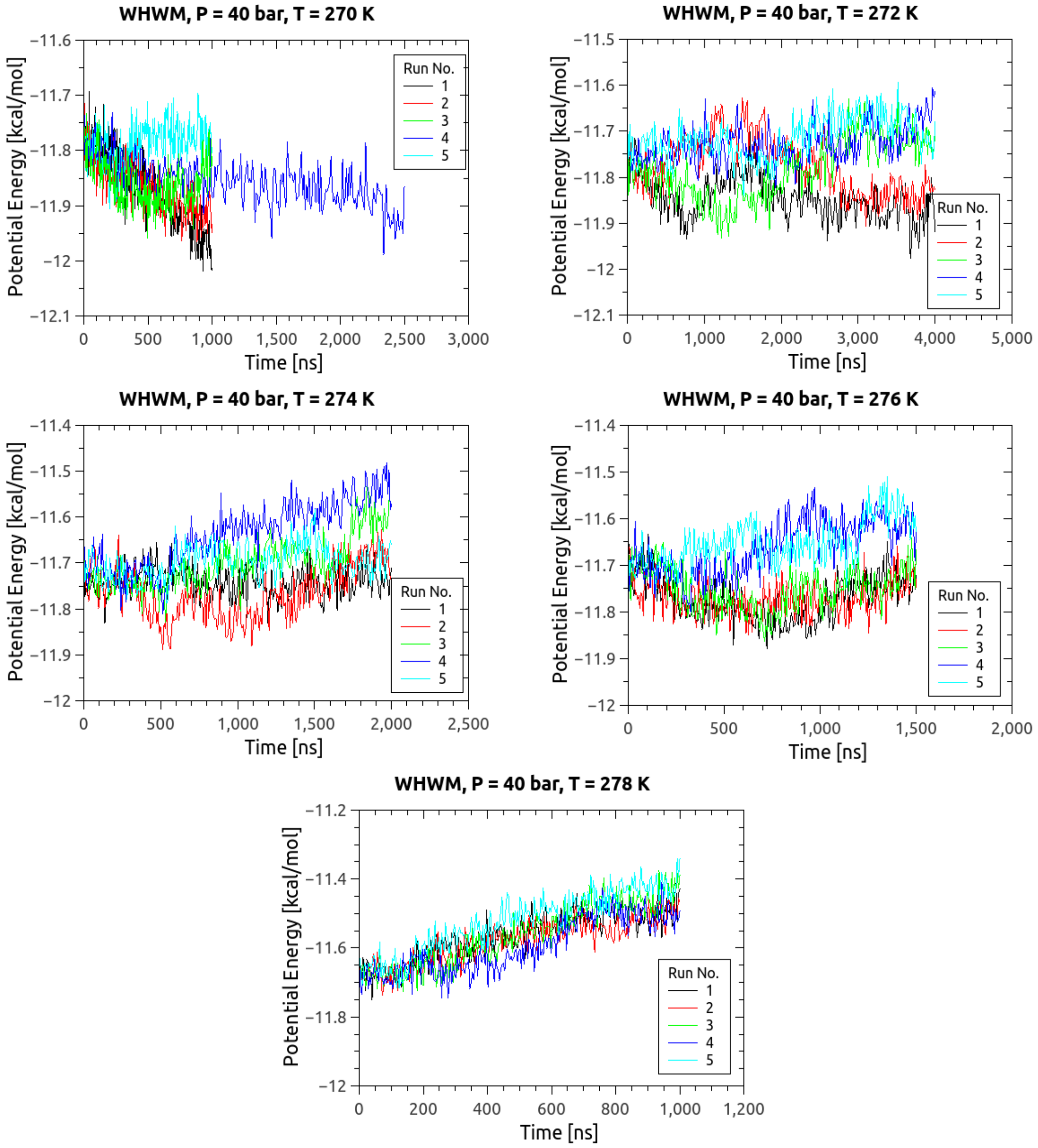

T (K)	Number 1	Number 2	Number 3	Number 4	Number 5
270	*g*	*g*	*g*	*g*	*g*
272	*g*	*g*	*g*	*d*	*d*
274	*g*	*d*	*d*	*d*	*d*
276	*g*	*d*	*d*	*d*	*d*
278	*d*	*d*	*d*	*d*	*d*
T_3 (K)	277	273	273	271	271

FIG. 26. Runs conducted at 40 bar. The calculated temperature is T_3 = 273.0 K with a standard deviation of 2.4 K.

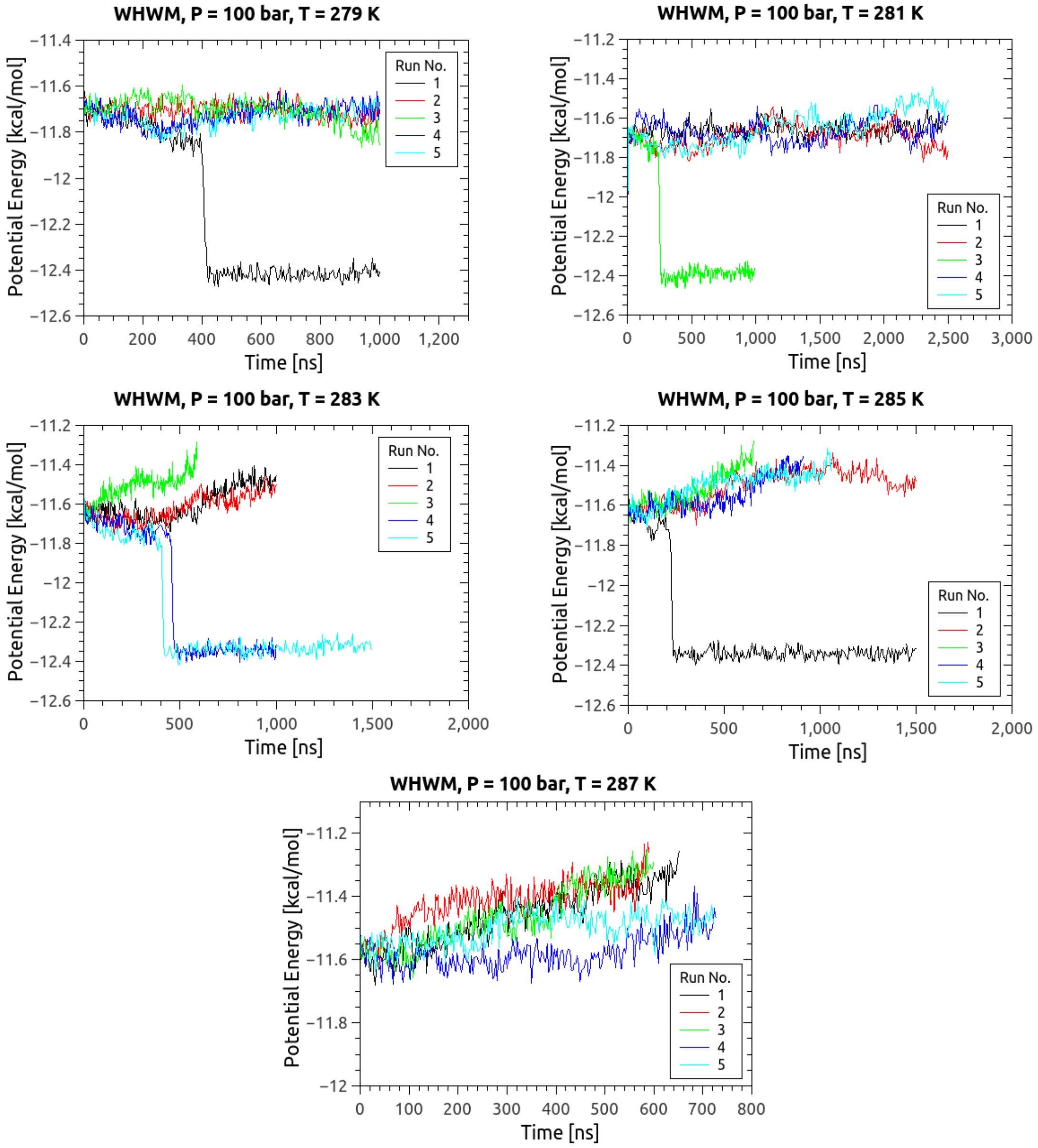

T (K)	Number 1	Number 2	Number 3	Number 4	Number 5
279	*g*	*g*	*g*	*g*	*g*
281	*g*	*g*	*g*	*g*	*d*
283	*g*	*g*	*d*	*d*	*d*
285	*g*	*d*	*d*	*d*	*d*
287	*d*	*d*	*d*	*d*	*d*
T_3 (K)	286	284	282	282	280

FIG. 27. Runs conducted at 100 bar. The calculated temperature is $T_3 = 282.8$ K with a standard deviation of 2.3 K.

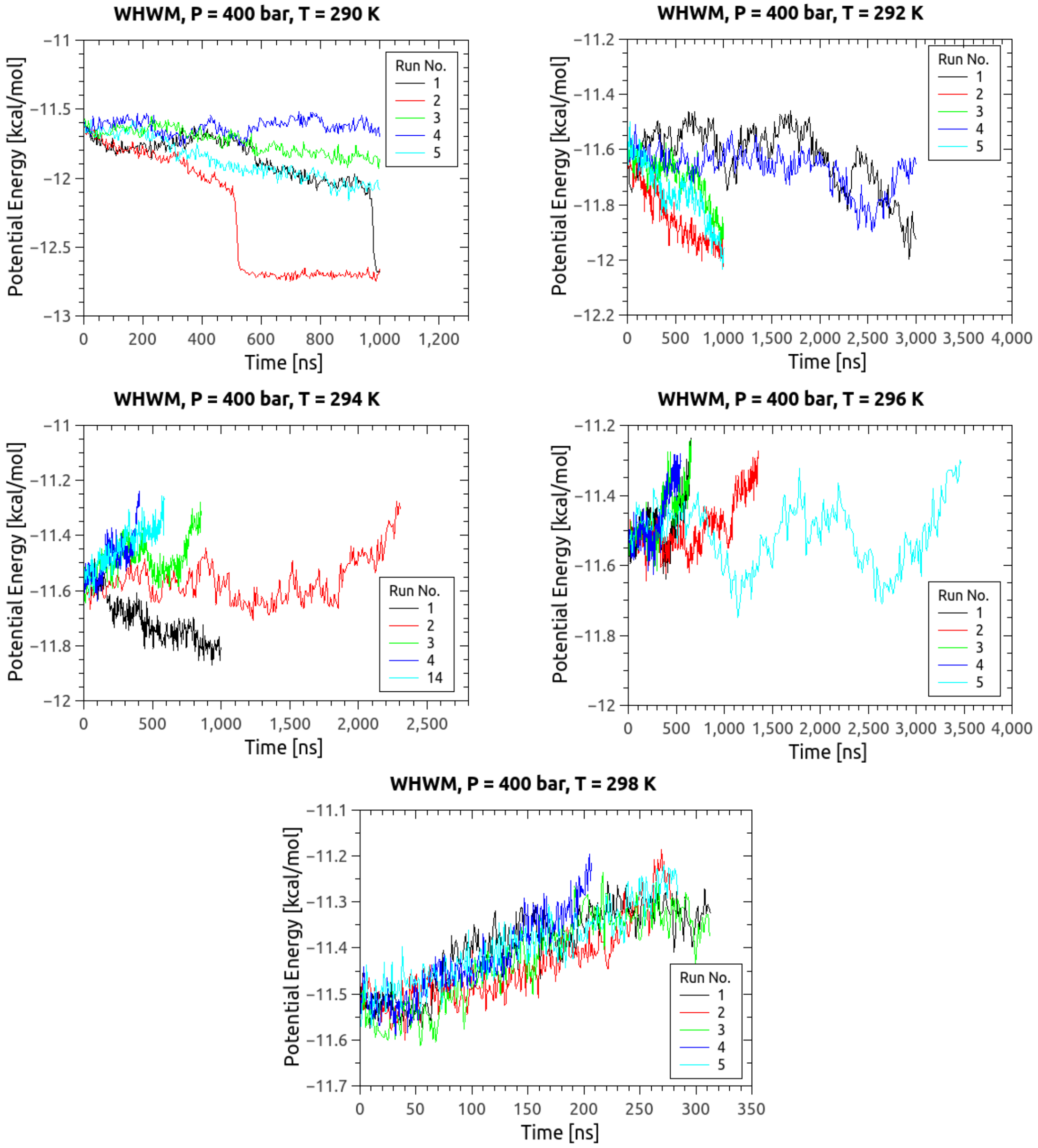

T (K)	Number 1	Number 2	Number 3	Number 4	Number 5
290	*g*	*g*	*g*	*g*	*g*
292	*g*	*g*	*g*	*g*	*g*
294	*g*	*d*	*d*	*d*	*d*
296	*d*	*d*	*d*	*d*	*d*
298	*d*	*d*	*d*	*d*	*d*
T_3 (K)	295	293	293	293	293

FIG. 28. Runs conducted at 400 bar. The calculated temperature is $T_3 = 293.4$ K with a standard deviation of 0.9 K.

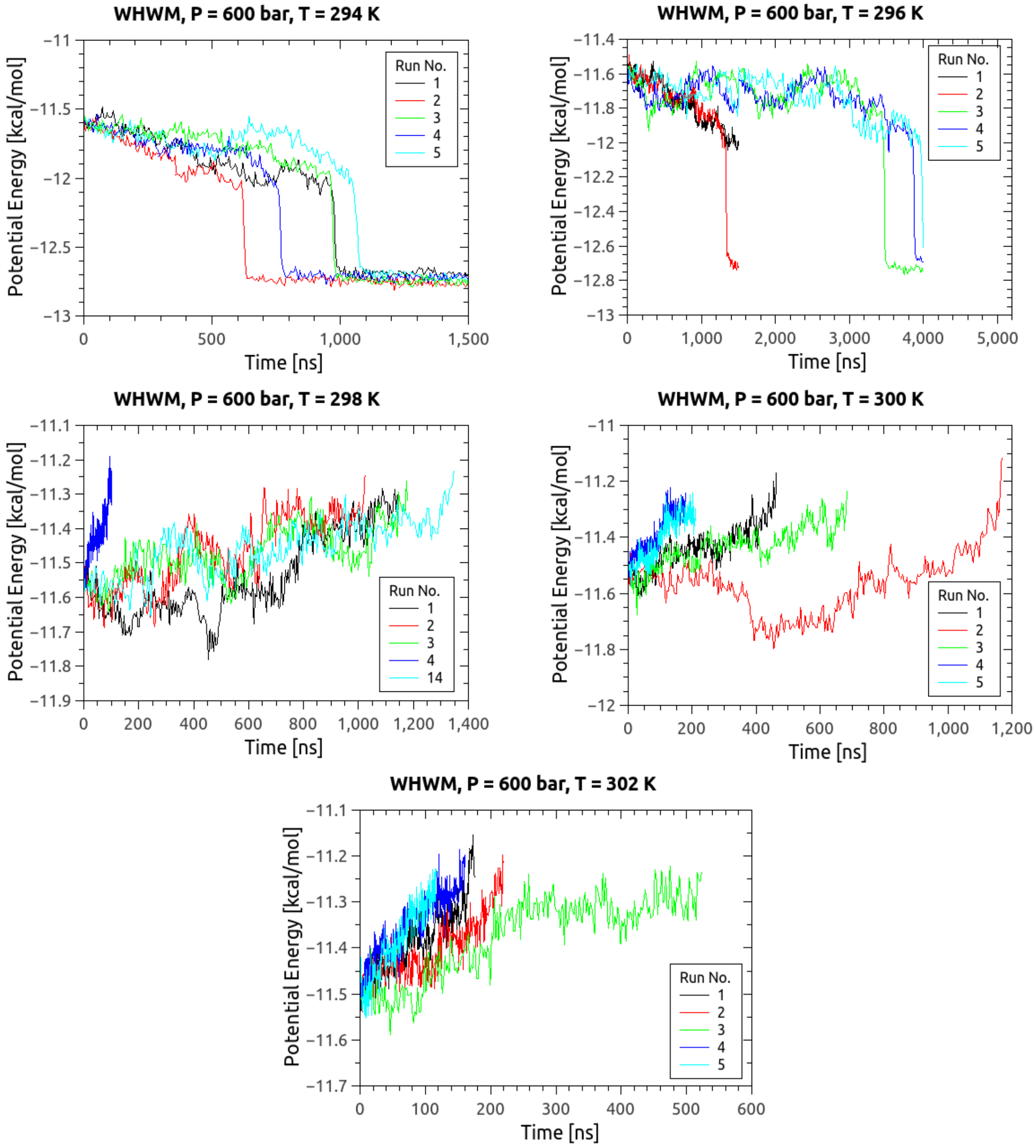

T (K)	Number 1	Number 2	Number 3	Number 4	Number 5
294	*g*	*g*	*g*	*g*	*g*
296	*g*	*g*	*g*	*g*	*g*
298	*d*	*d*	*d*	*d*	*d*
300	*d*	*d*	*d*	*d*	*d*
302	*d*	*d*	*d*	*d*	*d*
T_3 (K)	295	293	293	293	293

FIG. 29. Runs conducted at 600 bar. The calculated temperature is $T_3 = 297.0$ K with a standard deviation of 0.0 K.

APPENDIX B: CARBON DIOXIDE HYDRATE TEMPERATURE SCANS

In this section, the potential energy evolution for the multiple seeds at each pressure and temperature condition tested for the carbon dioxide hydrate system is presented. Each of the following pages includes the potential energy evolution through time of all the independent runs conducted at each temperature for a given pressure, water force field, and set of combining rules. This is followed by a table showing the final state of each independent run, which is denoted as (*g*) for hydrate growth, (*s*) for a stable potential energy, or (*d*) for hydrate dissociation. The title of each plot has the following format: “HWCW, water force field (TIP4P/ice or TIP4P/2005), combining rules (classic LB or modified LB), pressure (P = …), temperature (T = …)”.

The plots are organized in the order of the runs performed, as presented in section 5.2. First, the TIP4P/ice runs performed using the LB combining rules are presented. Second, the TIP4P/ice runs performed using the modification factor $\chi = 1.08$ are presented. Third, the TIP4P/2005 runs performed using the LB combining rules are presented. Last, the TIP4P/2005 runs performed using the modification factor $\chi = 1.115$ are presented.

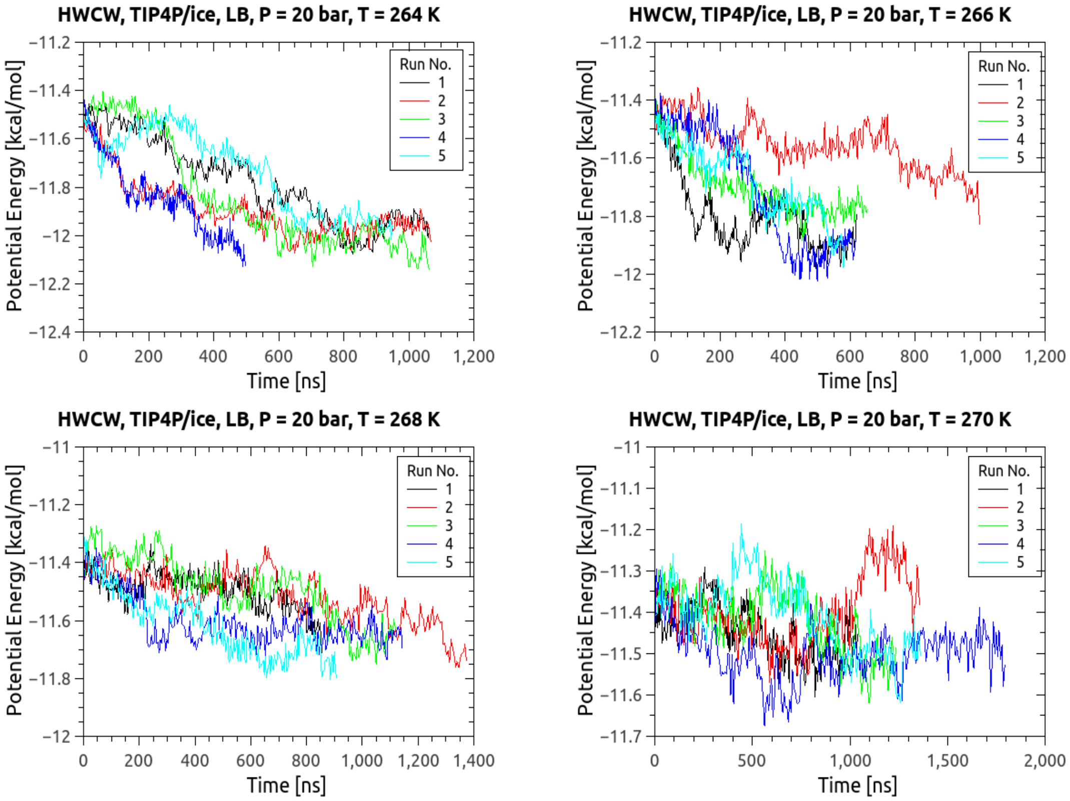

T (K)	Number 1	Number 2	Number 3	Number 4	Number 5
264	*g*	*g*	*g*	*g*	*g*
266	*g*	*g*	*g*	*g*	*g*
268	*g*	*g*	*g*	*g*	*g*
270	*s*	*s*	*s*	*s*	*s*
T₃ (K)	*270.0*	*270.0*	*270.0*	*270.0*	*270.0*

FIG. 30. Runs conducted at 20 bar using TIP4P/ice and LB combining rules. The calculated temperature is T_3 = 270.0 K with a standard deviation of 0.0 K.

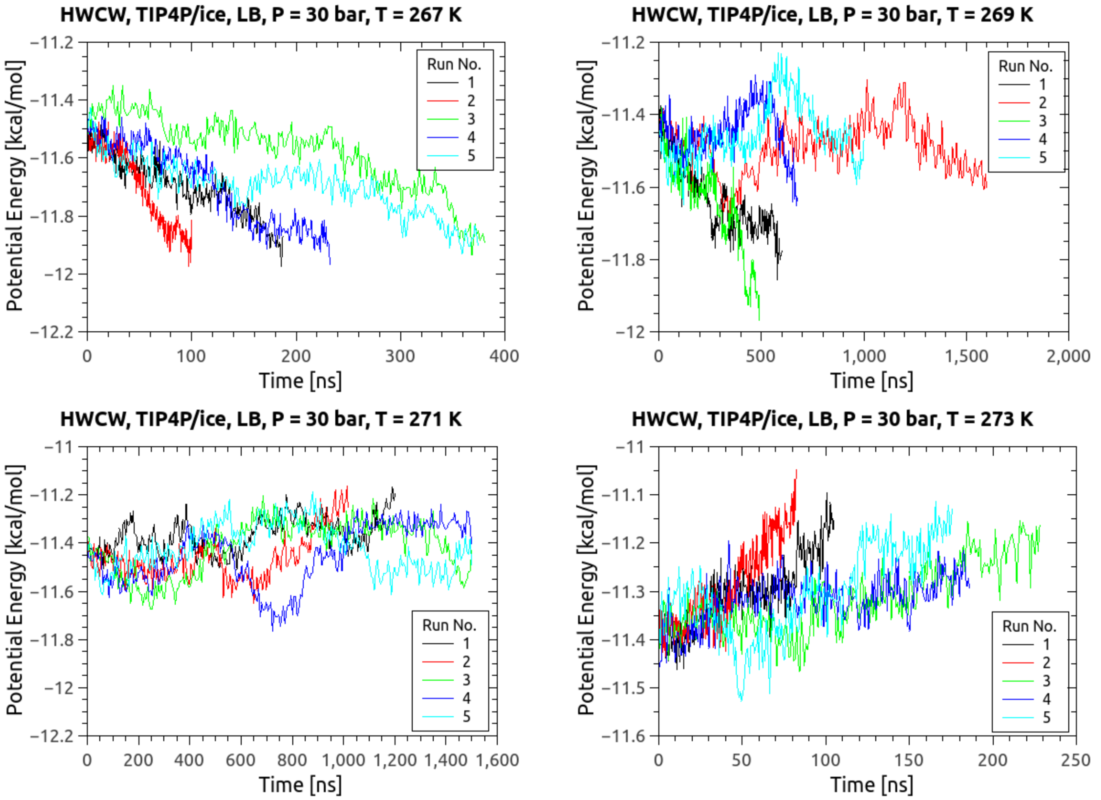

T (K)	Number 1	Number 2	Number 3	Number 4	Number 5
267	*g*	*g*	*g*	*g*	*g*
269	*g*	*g*	*g*	*g*	*g*
271	*d*	*d*	*d*	*d*	*d*
273	*d*	*d*	*d*	*d*	*d*
T_3 *(K)*	*270.0*	*270.0*	*270.0*	*270.0*	*270.0*

FIG. 31. Runs conducted at 30 bar using TIP4P/ice and LB combining rules. The calculated temperature is T_3 = 270.0 K with a standard deviation of 0.0 K.

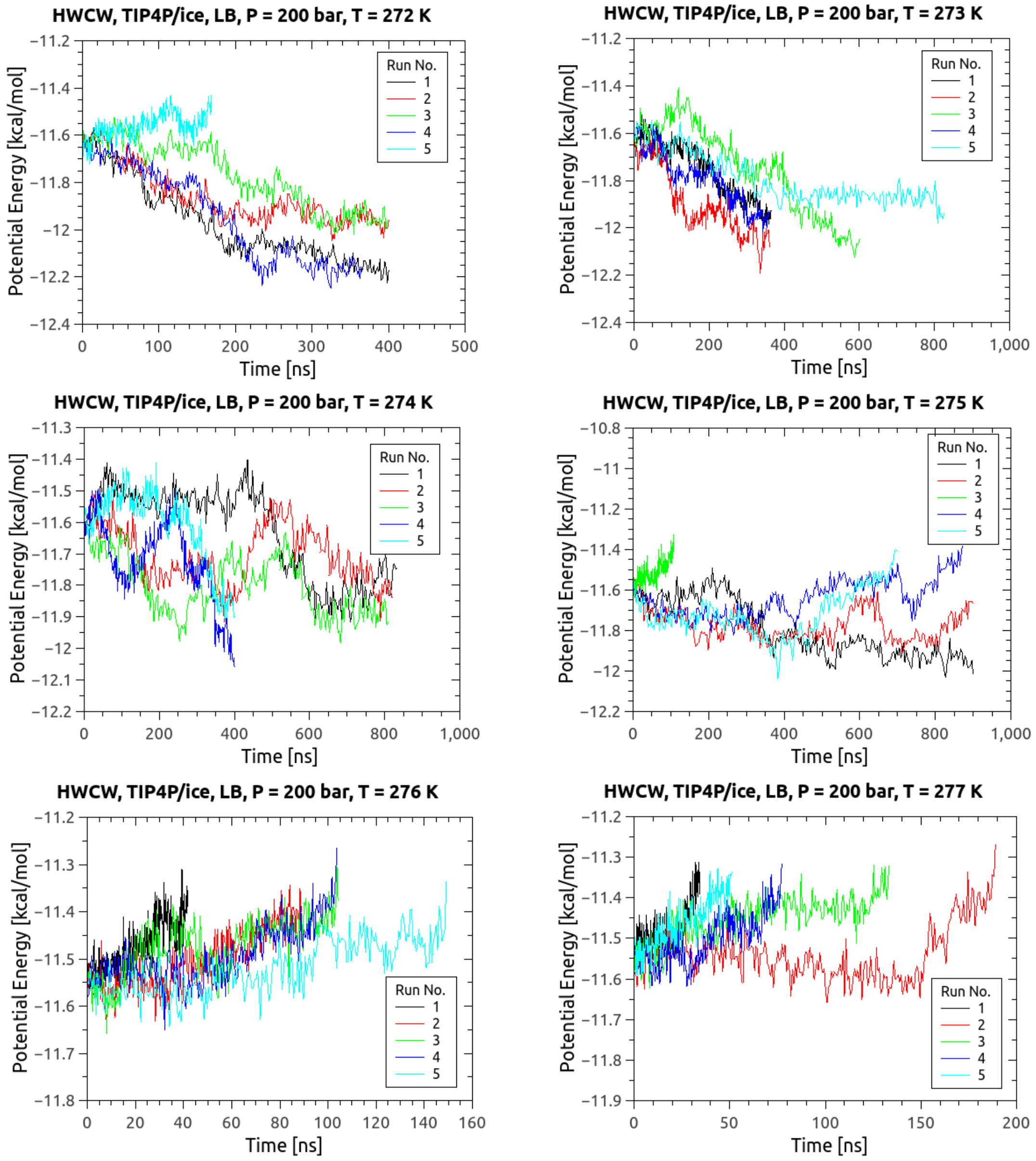

T (K)	Number 1	Number 2	Number 3	Number 4	Number 5
272	*g*	*g*	*g*	*g*	*d*
273	*g*	*g*	*g*	*g*	*g*
274	*g*	*g*	*g*	*g*	*g*
275	*g*	*s*	*d*	*d*	*d*
276	*d*	*d*	*d*	*d*	*d*
277	*d*	*d*	*d*	*d*	*d*
T_3 (K)	275.5	275	274.5	274.5	271.5

FIG. 32. Runs conducted at 200 bar using TIP4P/ice and LB combining rules. The calculated temperature is $T_3 = 276.1$ K with a standard deviation of 0.5 K.

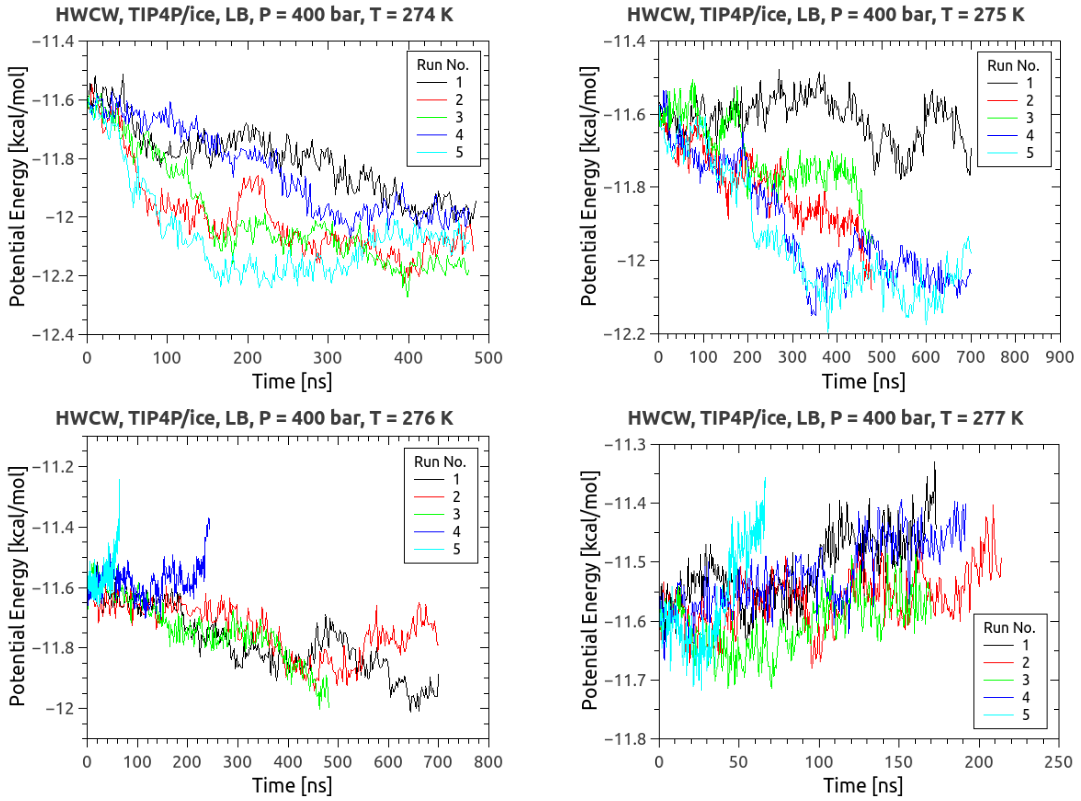

T (K)	Number 1	Number 2	Number 3	Number 4	Number 5
274	*g*	*g*	*g*	*g*	*g*
275	*g*	*g*	*g*	*g*	*s*
276	*g*	*g*	*g*	*d*	*d*
277	*d*	*d*	*d*	*d*	*d*
T_3 (K)	*276.5*	*276.5*	*276.5*	*275.5*	*275*

FIG. 33. Runs conducted at 400 bar using TIP4P/ice and LB combining rules. The calculated temperature is T_3 = 274.2 K with a standard deviation of 1.6 K.

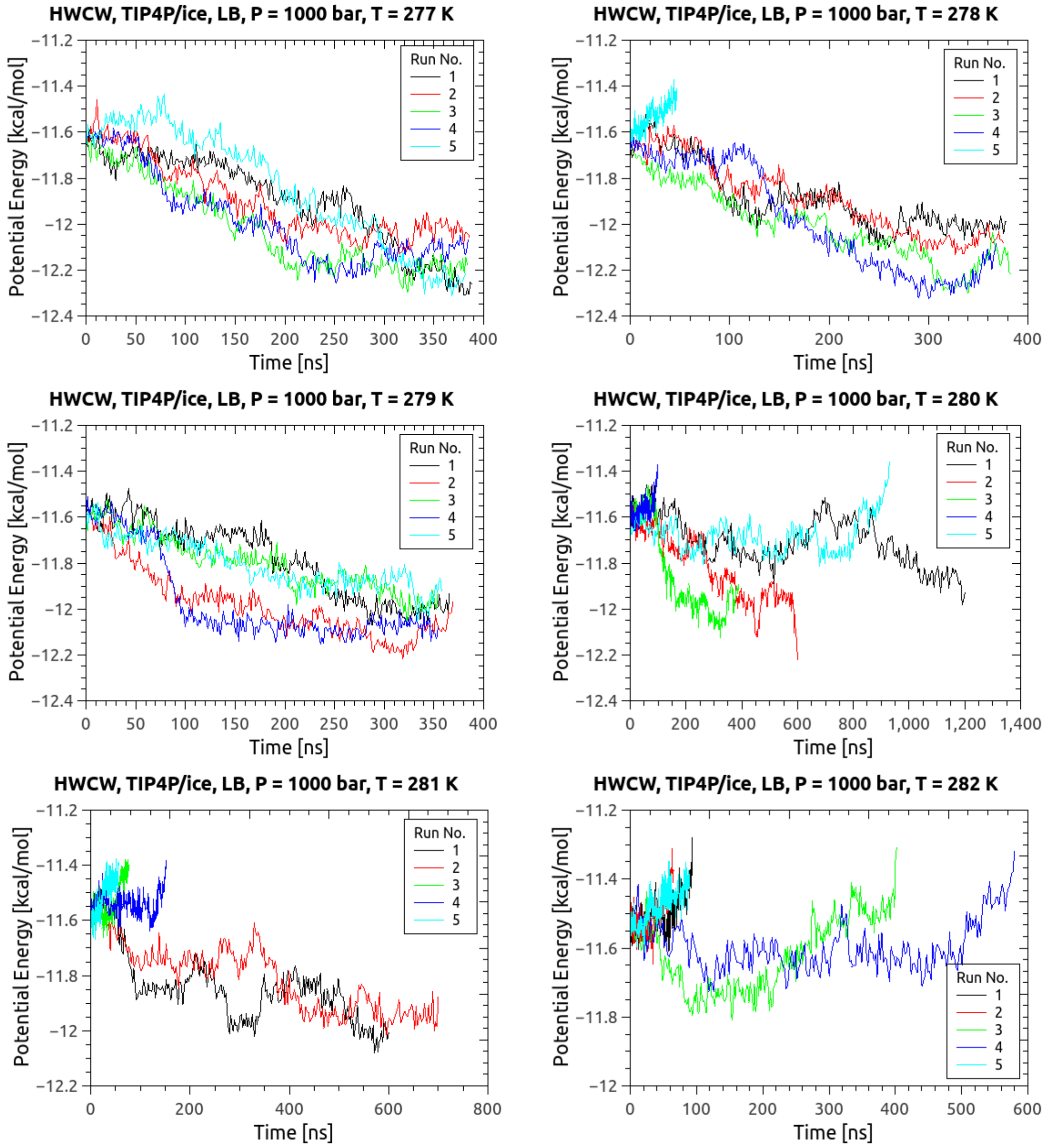

T (K)	Number 1	Number 2	Number 3	Number 4	Number 5
277	*g*	*g*	*g*	*g*	*g*
278	*g*	*g*	*g*	*g*	*d*
279	*g*	*g*	*g*	*g*	*g*
280	*g*	*g*	*g*	*d*	*d*
281	*g*	*g*	*d*	*d*	*d*
282	*d*	*d*	*d*	*d*	*d*
T3 (K)	*281.5*	*281.5*	*280.5*	*279.5*	*277.5*

FIG. 34. Runs conducted at 1000 bar using TIP4P/ice and LB combining rules. The calculated temperature is $T_3 = 280.1$ K with a standard deviation of 1.7 K.

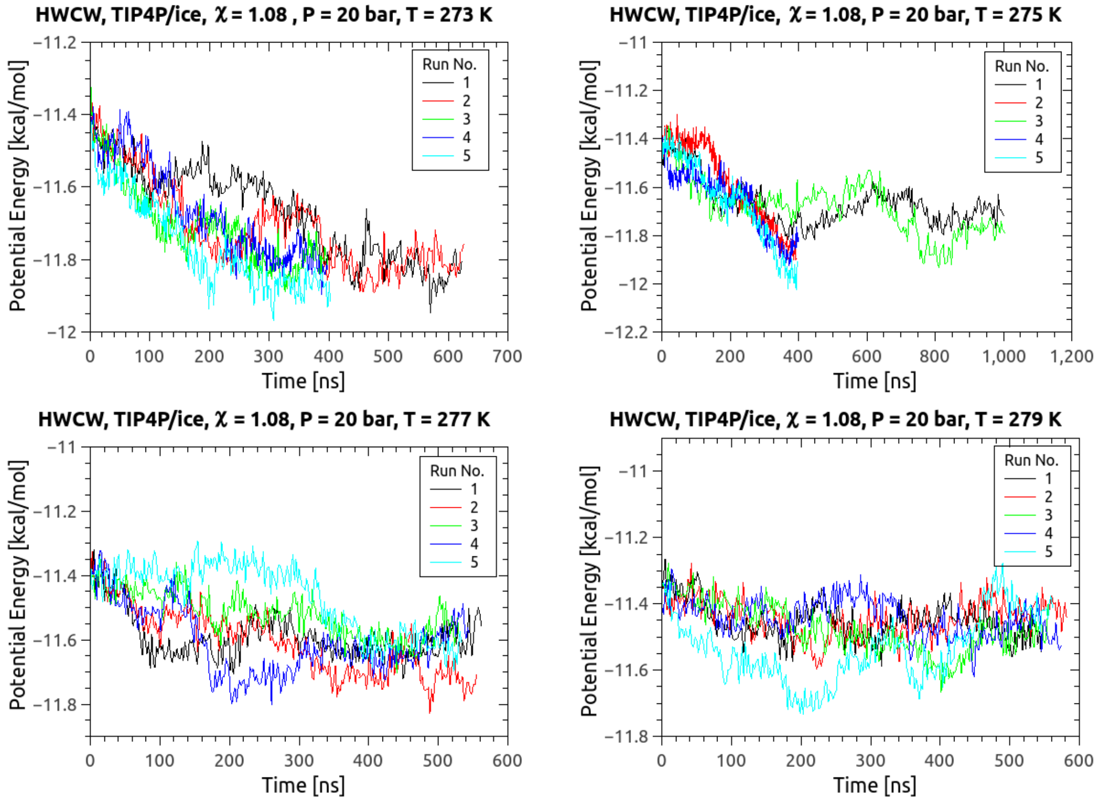

T (K)	Number 1	Number 2	Number 3	Number 4	Number 5
273	g	g	g	g	g
275	g	g	g	g	g
277	g	g	g	g	g
279	s	s	s	s	s
T3 (K)	279.0	279.0	279.0	279.0	279.0

FIG. 35. Runs conducted at 20 bar using TIP4P/ice and χ = 1.08 modification. The calculated temperature is T_3 = 279.0 K with a standard deviation of 0.0 K.

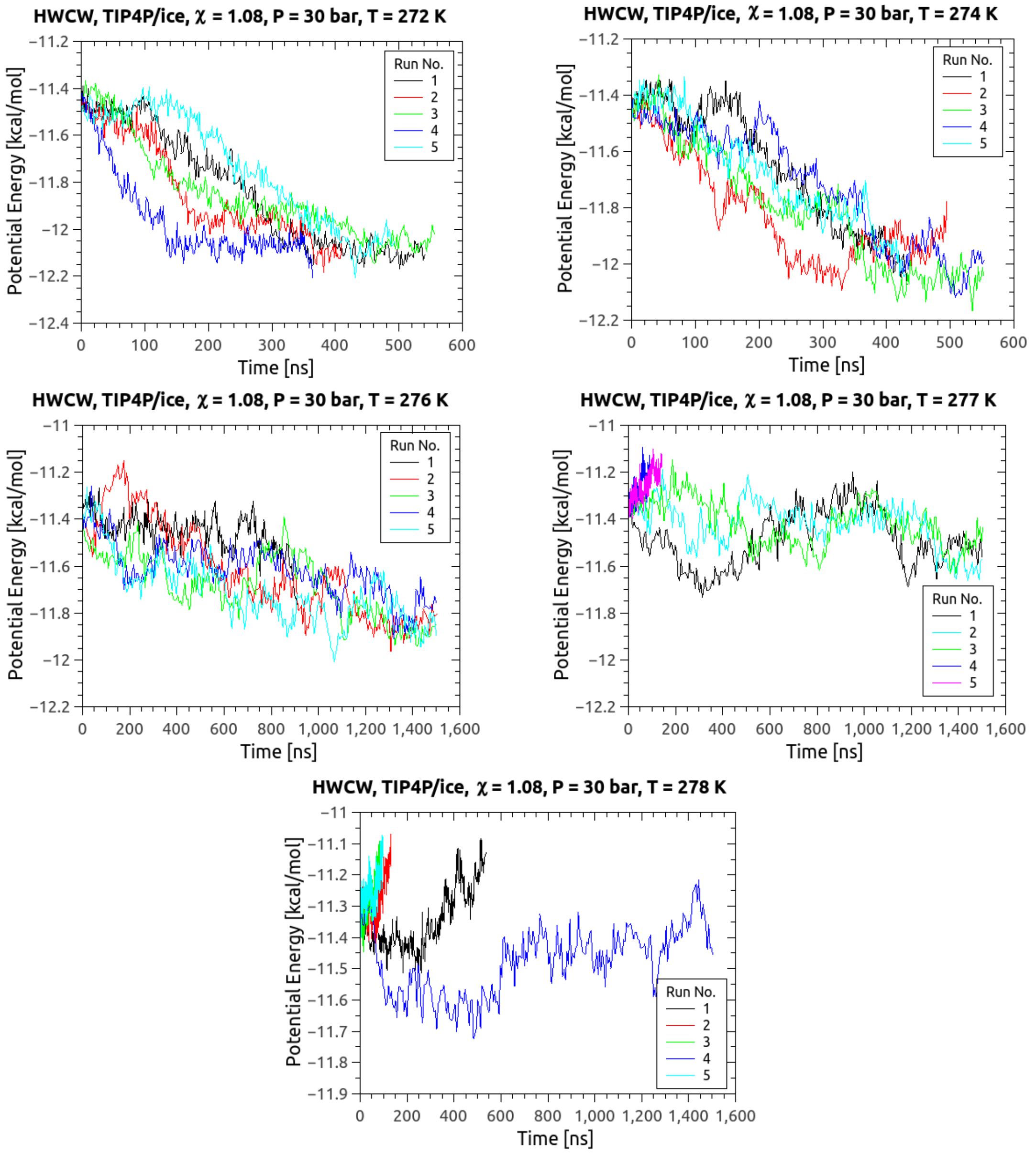

T (K)	Number 1	Number 2	Number 3	Number 4	Number 5
272	*g*	*g*	*g*	*g*	*g*
274	*g*	*g*	*g*	*g*	*d*
276	*g*	*g*	*g*	*g*	*g*
277	*g*	*g*	*g*	*d*	*d*
278	*d*	*d*	*d*	*d*	*d*
T_3 (K)	277.5	277.5	277.5	276.5	276.5

FIG. 36. Runs conducted at 30 bar using TIP4P/ice and χ = 1.08 modification. The calculated temperature is T_3 = 277.1 K with a standard deviation of 0.5 K.

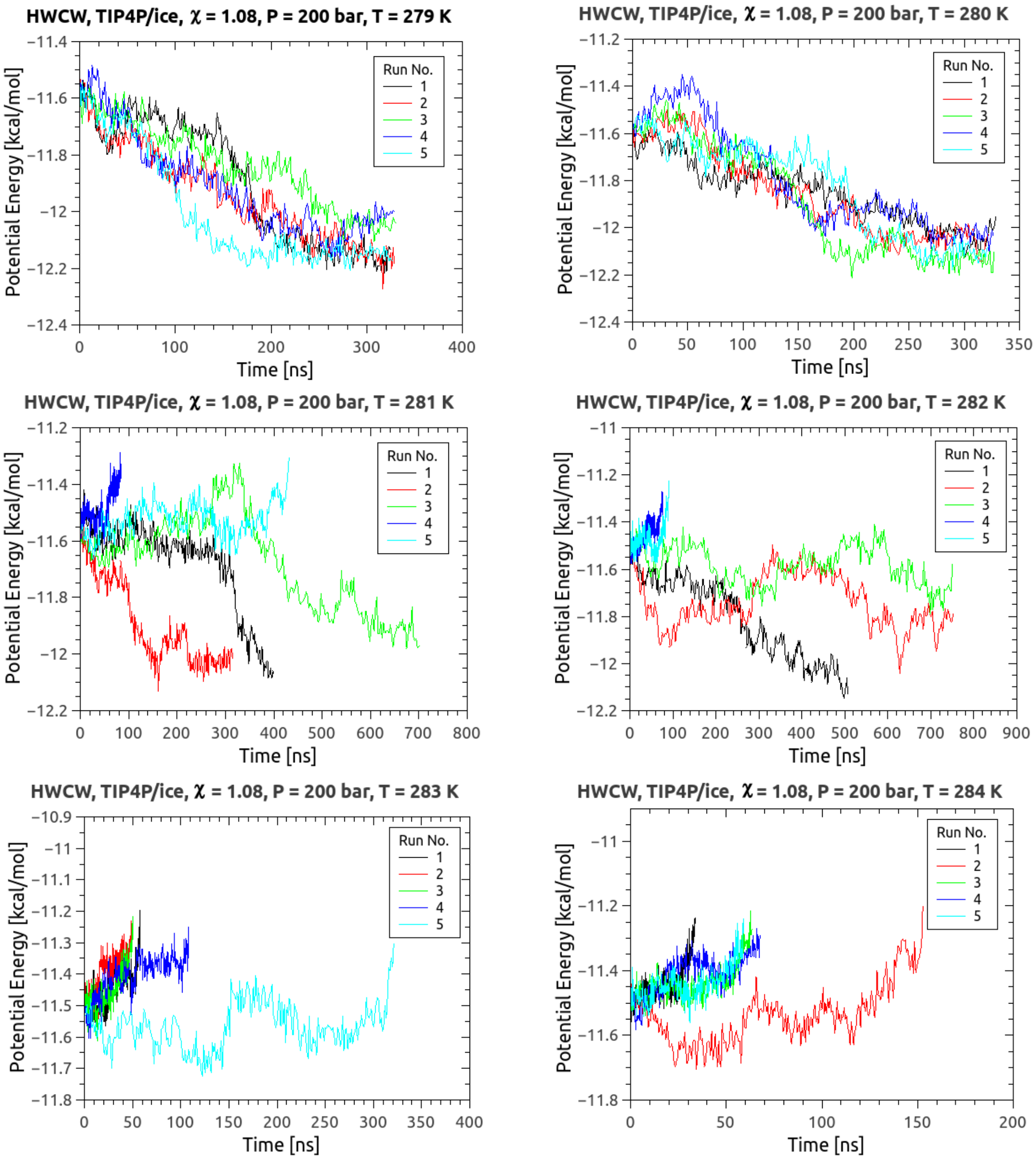

T (K)	Number 1	Number 2	Number 3	Number 4	Number 5
272	*g*	*g*	*g*	*g*	*d*
273	*g*	*g*	*g*	*g*	*d*
274	*g*	*g*	*g*	*g*	*g*
275	*g*	*s*	*d*	*d*	*d*
276	*d*	*d*	*d*	*d*	*d*
277	*d*	*d*	*d*	*d*	*d*
T_3 (K)	275.5	275	274.5	274.5	271.5

FIG. 37. Runs conducted at 200 bar using TIP4P/ice and χ = 1.08 modification. The calculated temperature is T_3 = 281.5 K with a standard deviation of 0.9 K.

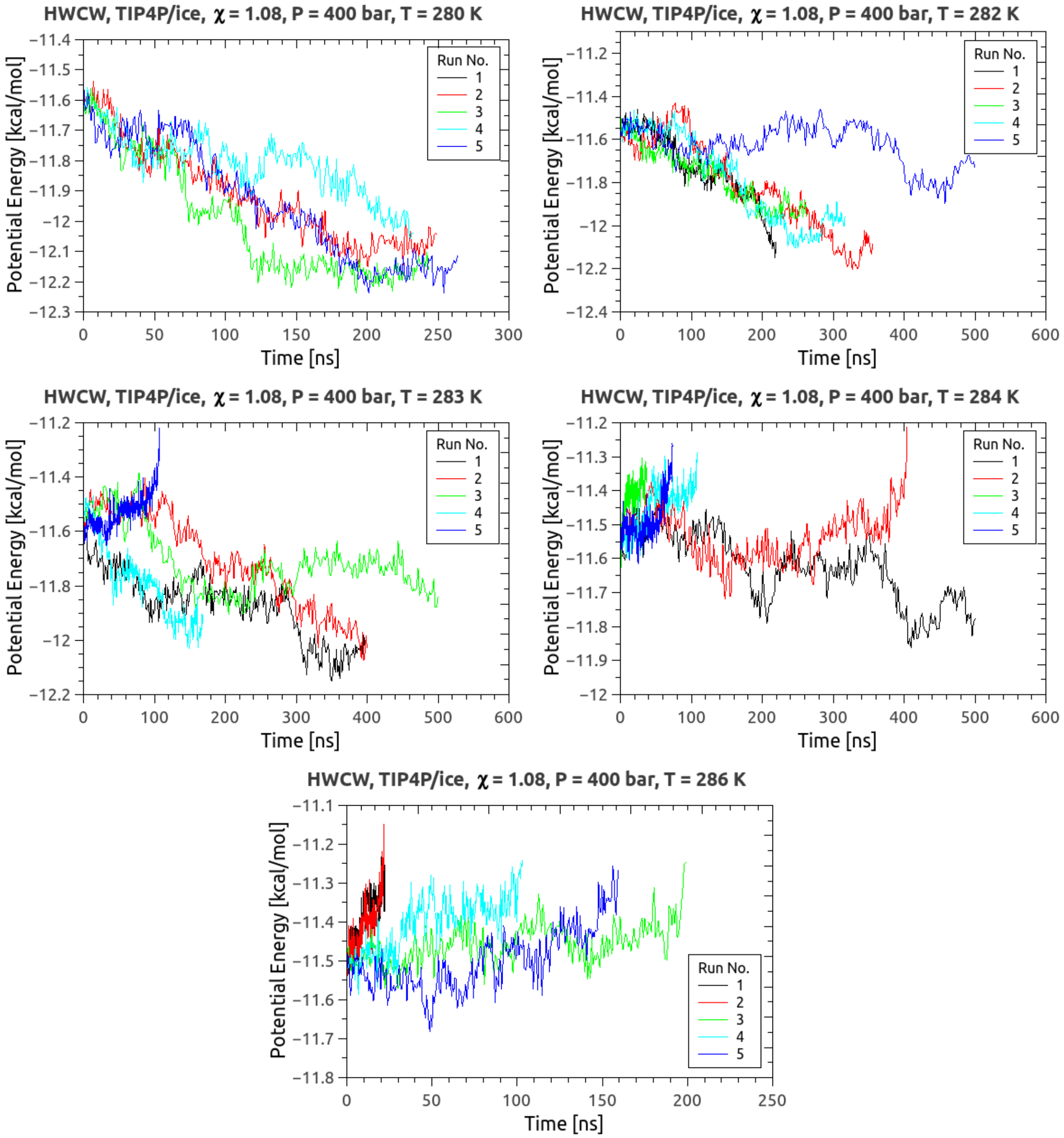

T (K)	Number 1	Number 2	Number 3	Number 4	Number 5
280	g	g	g	g	g
282	g	g	g	g	g
283	g	g	g	g	d
284	g	d	d	d	d
286	d	d	d	d	d
T3 (K)	284.5	283.5	283.5	283.5	282.5

FIG. 38. Runs conducted at 400 bar using TIP4P/ice and χ = 1.08 modification. The calculated temperature is T_3 = 283.5 K with a standard deviation of 0.7 K.

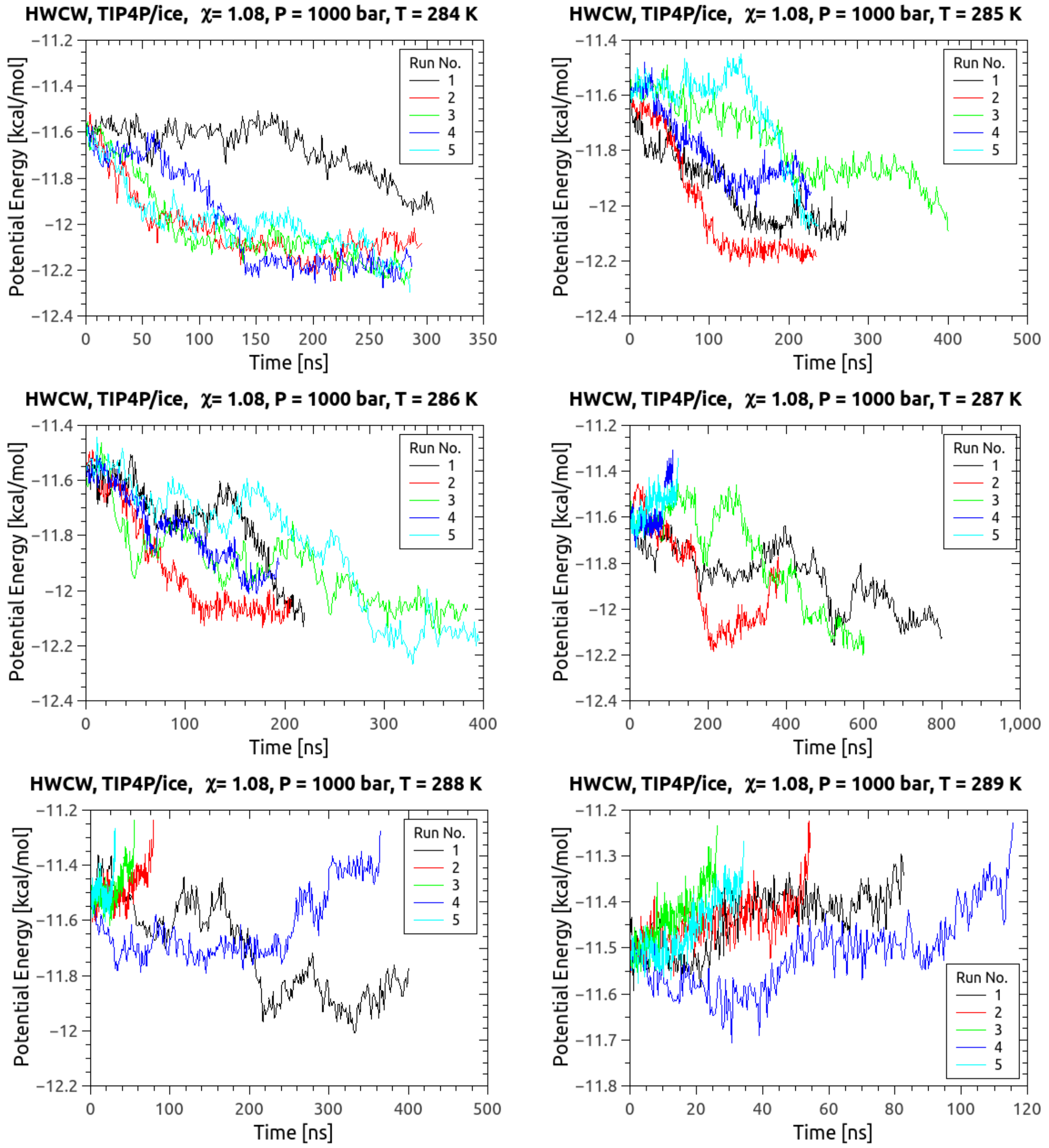

T (K)	Number 1	Number 2	Number 3	Number 4	Number 5
284	*g*	*g*	*g*	*g*	*g*
285	*g*	*g*	*g*	*g*	*g*
286	*g*	*g*	*g*	*g*	*g*
287	*g*	*g*	*g*	*d*	*d*
288	*g*	*d*	*d*	*d*	*d*
289	*d*	*d*	*d*	*d*	*d*
T_3 *(K)*	288.5	287.5	287.5	286.5	286.5

FIG. 39. Runs conducted at 1000 bar using TIP4P/ice and χ = 1.08 modification. The calculated temperature is T_3 = 287.3 K with a standard deviation of 0.8 K.

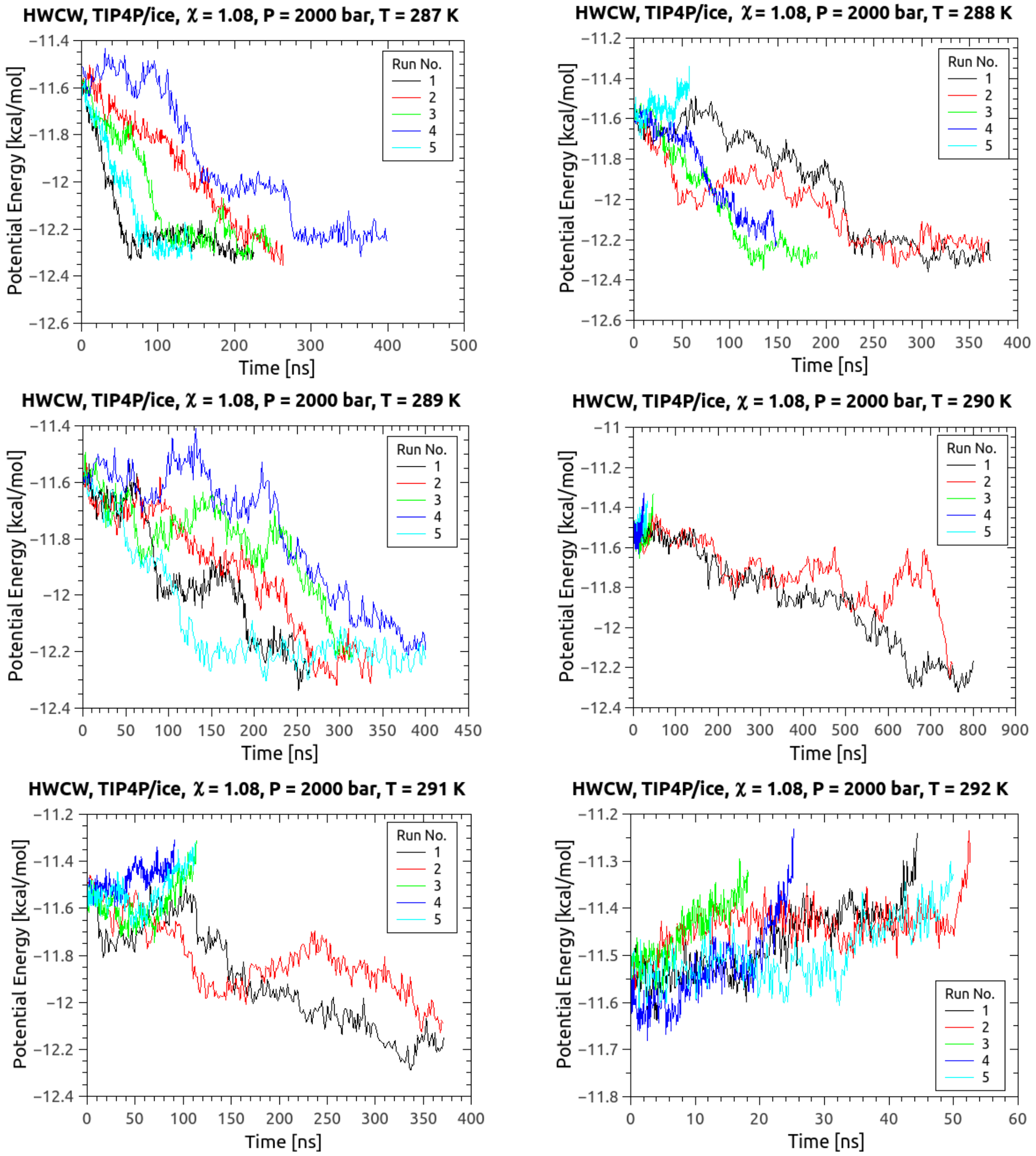

T (K)	Number 1	Number 2	Number 3	Number 4	Number 5
287	*g*	*g*	*g*	*g*	*g*
288	*g*	*g*	*g*	*g*	*d*
289	*g*	*g*	*g*	*g*	*g*
290	*g*	*g*	*d*	*d*	*d*
291	*g*	*g*	*d*	*d*	*d*
292	*d*	*d*	*d*	*d*	*d*
T_3 *(K)*	291.5	291.5	289.5	289.5	287.5

FIG. 40. Runs conducted at 2000 bar using TIP4P/ice and $\chi = 1.08$ modification. The calculated temperature is $T_3 = 289.9$ K with a standard deviation of 1.7 K.

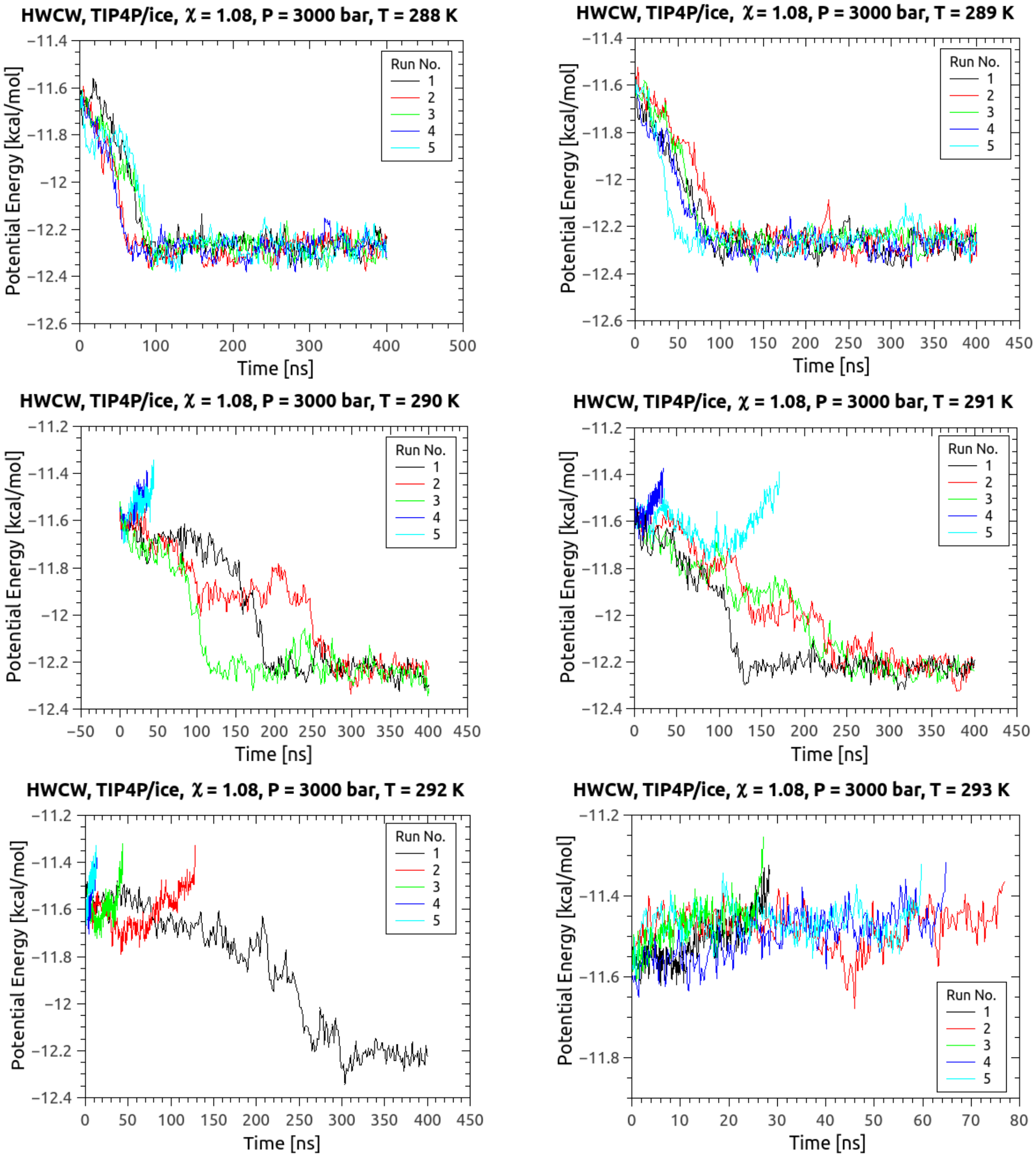

T (K)	Number 1	Number 2	Number 3	Number 4	Number 5
288	*g*	*g*	*g*	*g*	*g*
289	*g*	*g*	*g*	*g*	*g*
290	*g*	*g*	*g*	*d*	*d*
291	*g*	*g*	*g*	*d*	*d*
292	*g*	*d*	*d*	*d*	*d*
293	*d*	*d*	*d*	*d*	*d*
T_3 *(K)*	292.5	291.5	291.5	289.5	289.5

FIG. 41. Runs conducted at 3000 bar using TIP4P/ice and χ = 1.08 modification. The calculated temperature is T_3 = 290.9 K with a standard deviation of 1.3 K.

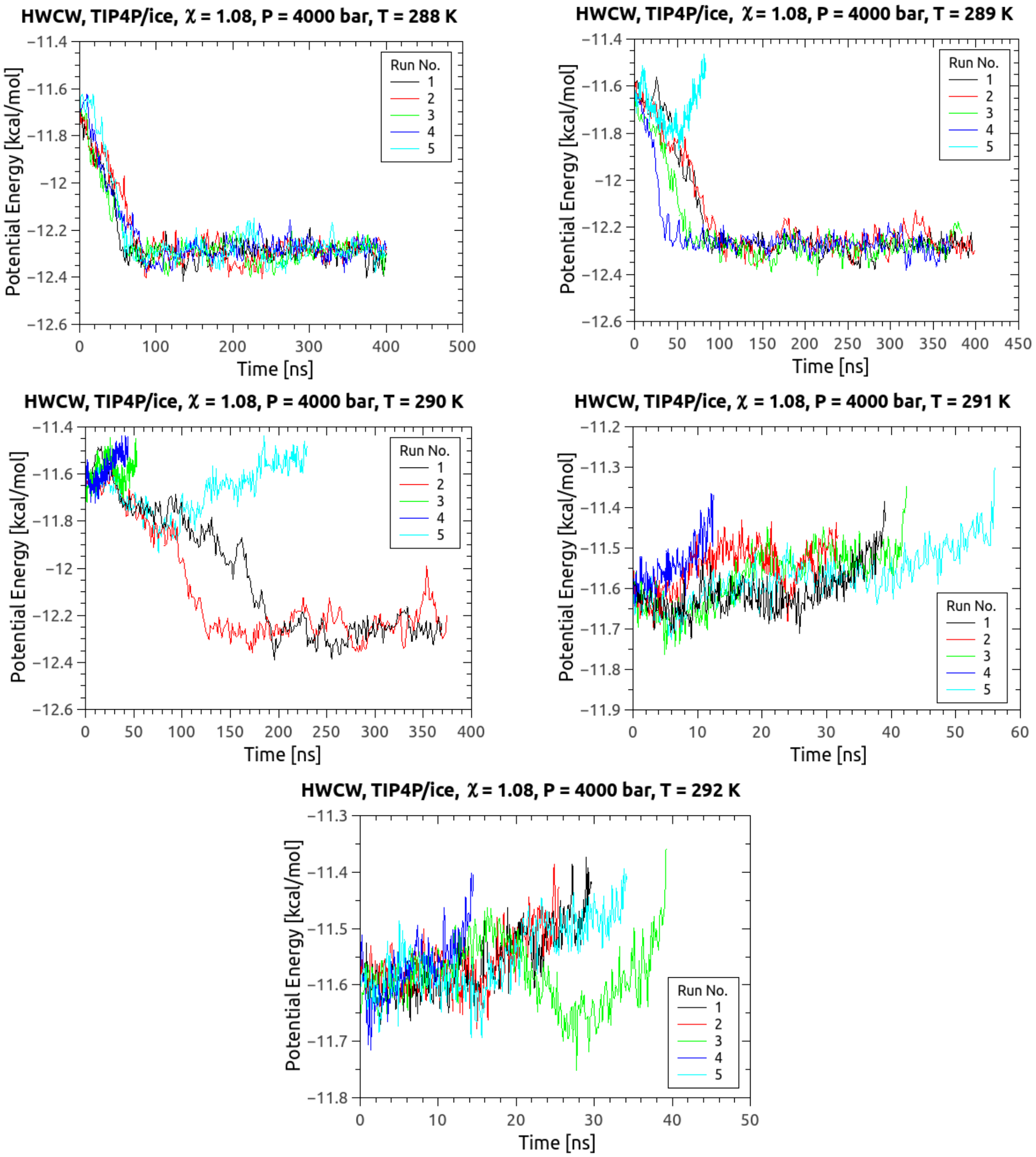

T (K)	Number 1	Number 2	Number 3	Number 4	Number 5
288	*g*	*g*	*g*	*g*	*g*
289	*g*	*g*	*g*	*g*	*d*
290	*g*	*g*	*d*	*d*	*d*
291	*d*	*d*	*d*	*d*	*d*
292	*d*	*d*	*d*	*d*	*d*
T_3 *(K)*	290.5	290.5	289.5	289.5	288.5

FIG. 42. Runs conducted at 4000 bar using TIP4P/ice and χ = 1.08 modification. The calculated temperature is T_3 = 289.7 K with a standard deviation of 0.8 K.

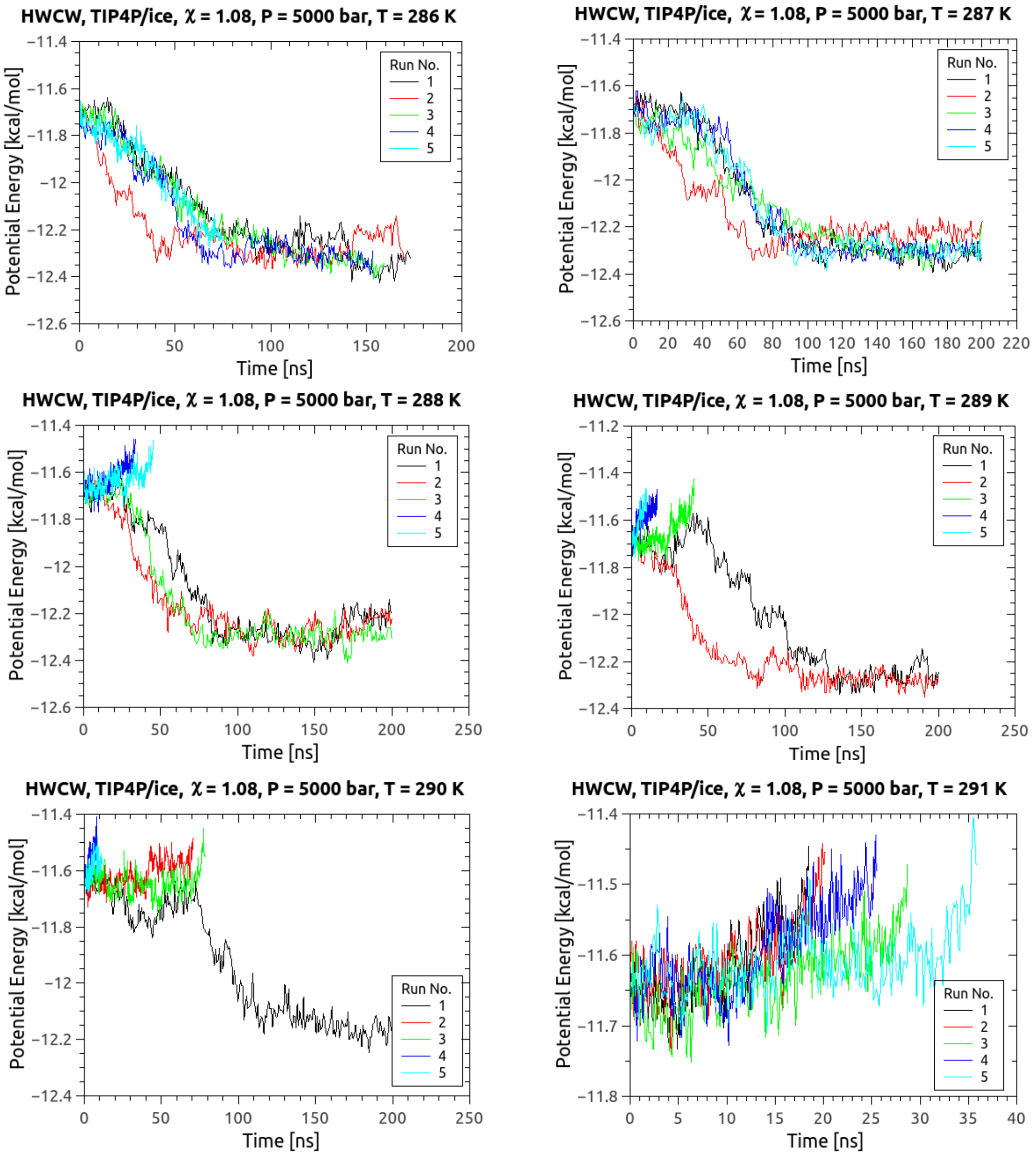

T (K)	Number 1	Number 2	Number 3	Number 4	Number 5
286	*g*	*g*	*g*	*g*	*g*
287	*g*	*g*	*g*	*g*	*g*
288	*g*	*g*	*g*	*d*	*d*
289	*g*	*g*	*d*	*d*	*d*
290	*g*	*d*	*d*	*d*	*d*
291	*d*	*d*	*d*	*d*	*d*
T_3 *(K)*	290.5	289.5	288.5	287.5	287.5

FIG. 43. Runs conducted at 5000 bar using TIP4P/ice and χ = 1.08 modification. The calculated temperature is T_3 = 288.7 K with a standard deviation of 1.3 K.

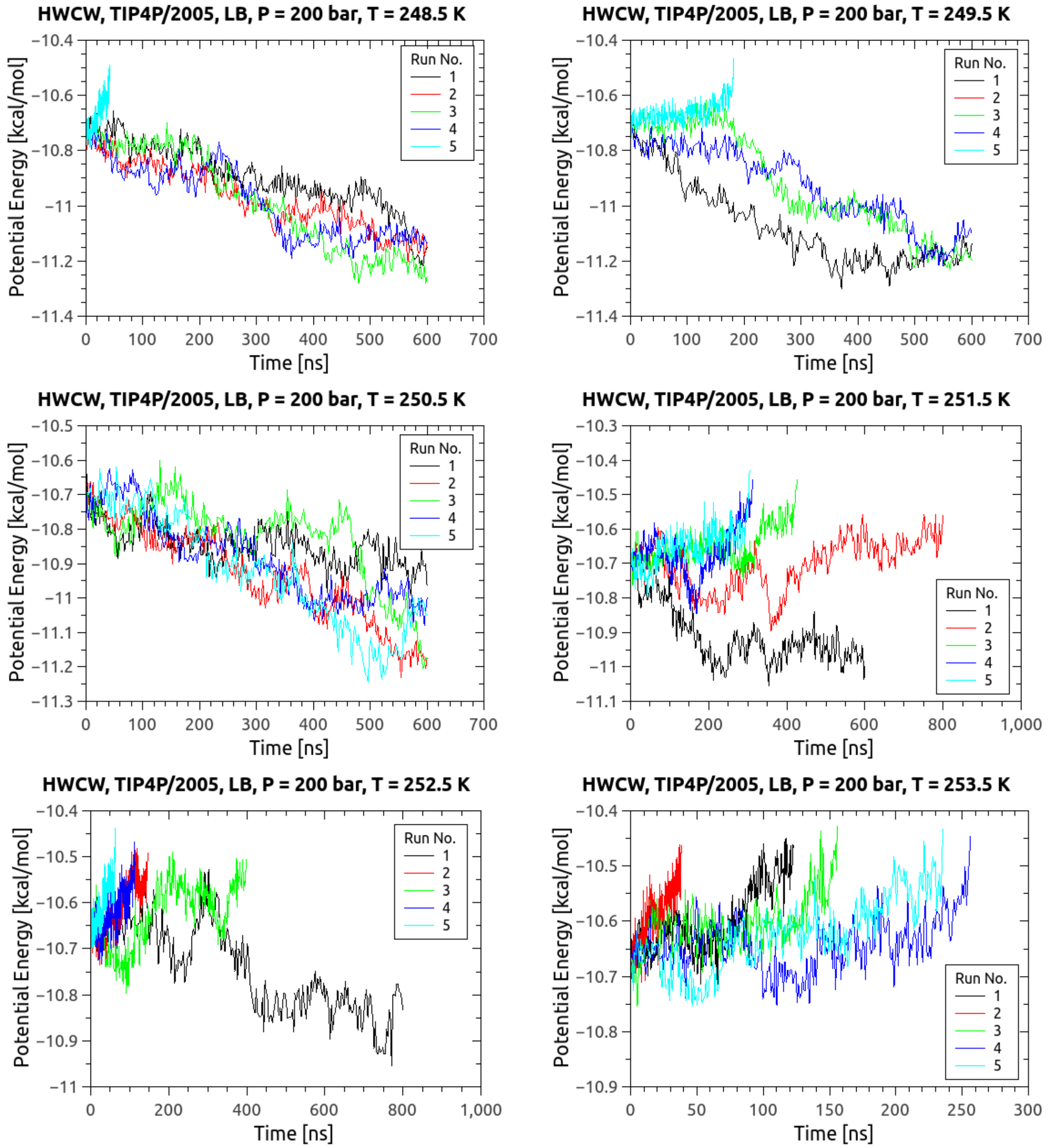

T (K)	Number 1	Number 2	Number 3	Number 4	Number 5
248.5	*g*	*g*	*g*	*g*	*d*
249.5	*g*	*g*	*g*	*g*	*d*
250.5	*g*	*g*	*g*	*g*	*g*
251.5	*g*	*s*	*d*	*d*	*d*
252.5	*g*	*d*	*d*	*d*	*d*
253.5	*d*	*d*	*d*	*d*	*d*
T_3 *(K)*	*253*	*251.5*	*251*	*251*	*248*

FIG. 44. Runs conducted at 200 bar using TIP4P/2005 and LB combining rules. The calculated temperature is T_3 = 250.9 K with a standard deviation of 1.8 K.

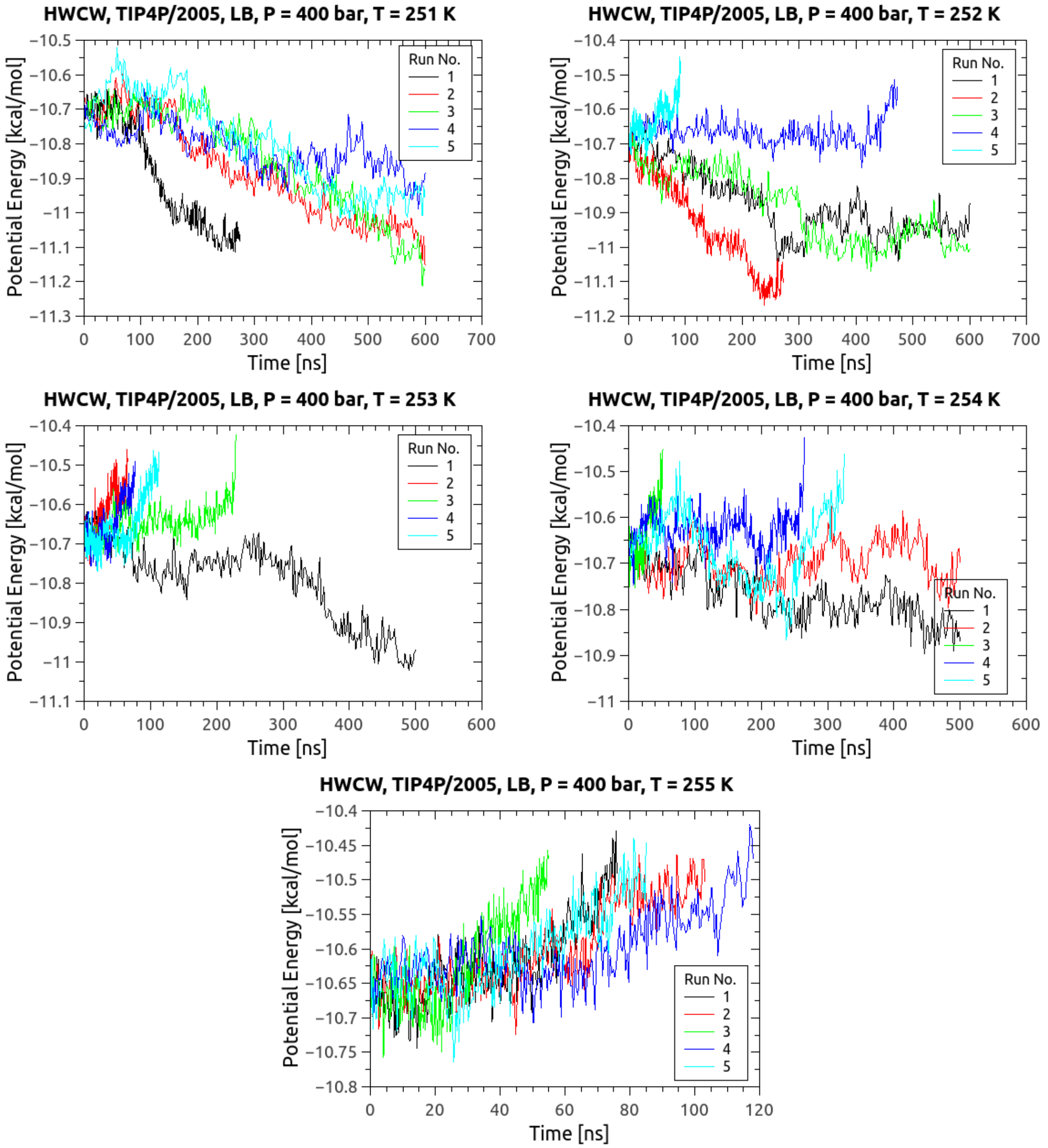

T (K)	Number 1	Number 2	Number 3	Number 4	Number 5
251	g	g	g	g	g
252	g	g	g	d	d
253	g	d	d	d	d
254	g	s	d	d	d
255	d	d	d	d	d
T_3 (K)	254.5	252.5	252.5	251.5	251.5

FIG. 45. Runs conducted at 400 bar using TIP4P/2005 and LB combining rules. The calculated temperature is T_3 = 252.5 K with a standard deviation of 1.2 K.

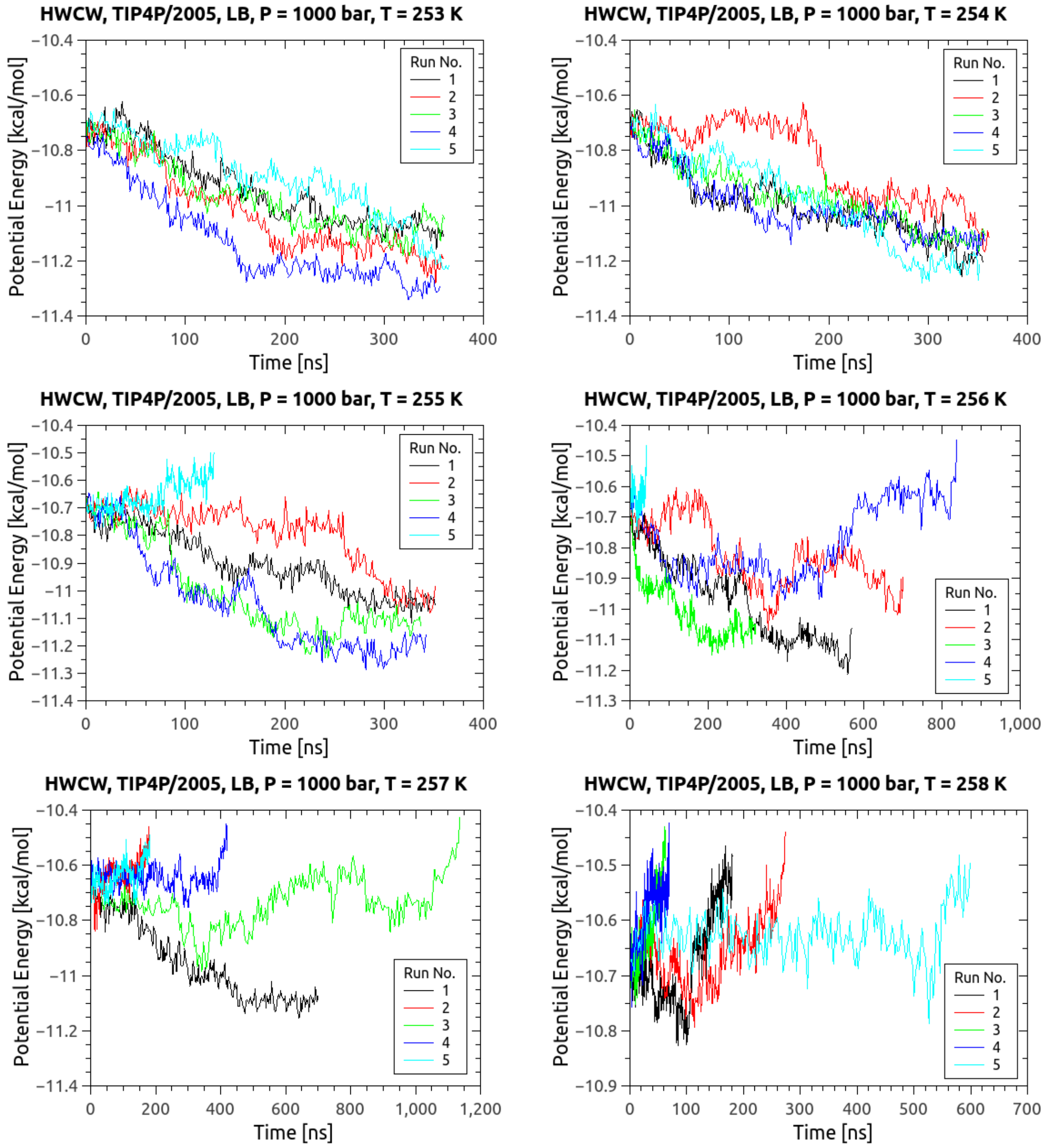

T (K)	Number 1	Number 2	Number 3	Number 4	Number 5
253	*g*	*g*	*g*	*g*	*g*
254	*g*	*g*	*g*	*g*	*g*
255	*g*	*g*	*g*	*g*	*d*
256	*g*	*g*	*g*	*d*	*d*
257	*g*	*d*	*d*	*d*	*d*
258	*d*	*d*	*d*	*d*	*d*
T_3 *(K)*	*257.5*	*256.5*	*256.5*	*255.5*	*254.5*

FIG. 46. Runs conducted at 1000 bar using TIP4P/2005 and LB combining rules. The calculated temperature is T_3 = 256.1 K with a standard deviation of 1.1 K.

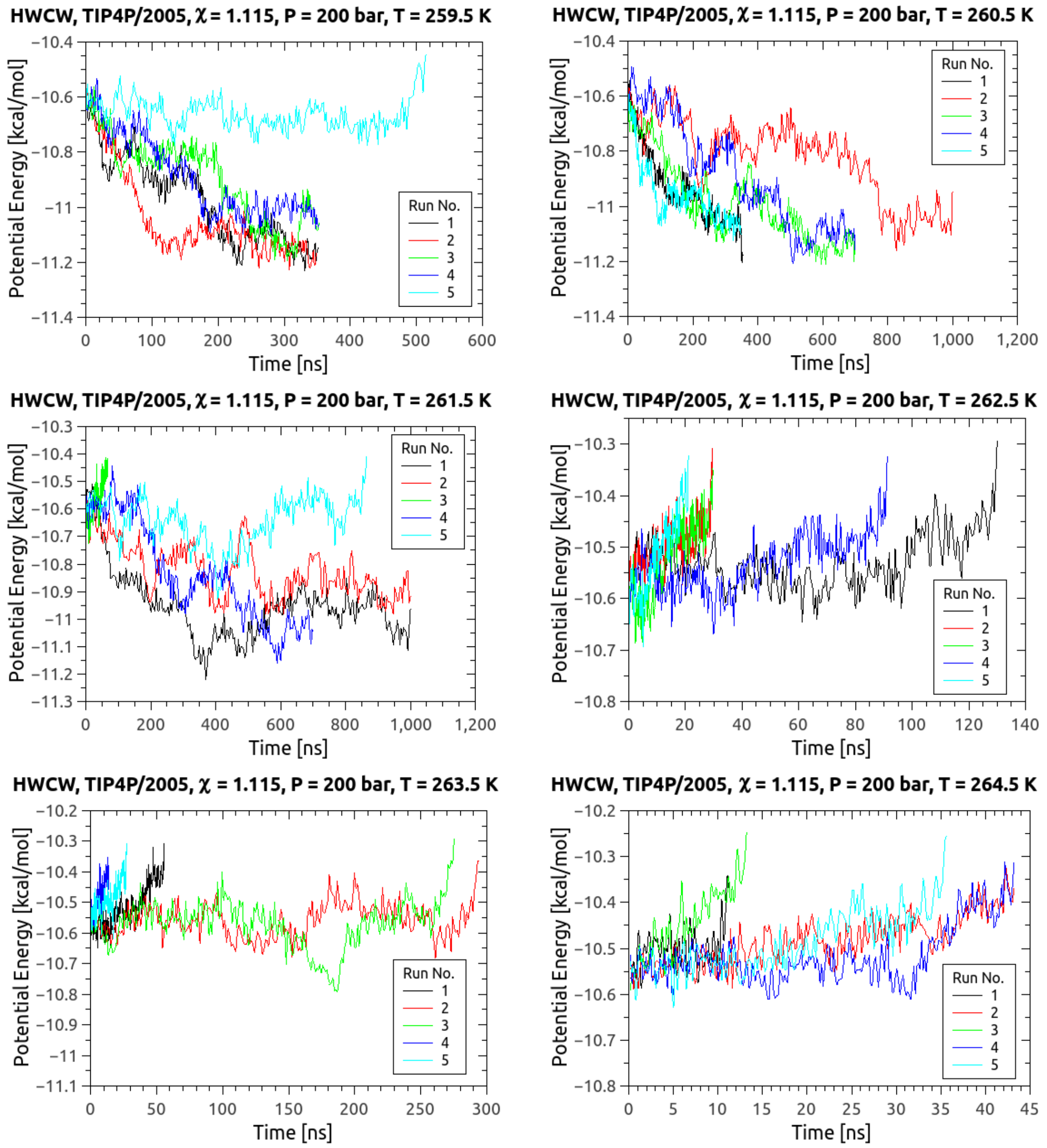

T (K)	Number 1	Number 2	Number 3	Number 4	Number 5
259.5	*g*	*g*	*g*	*g*	*d*
260.5	*g*	*g*	*g*	*g*	*g*
261.5	*g*	*g*	*g*	*d*	*d*
262.5	*d*	*d*	*d*	*d*	*d*
263.5	*d*	*d*	*d*	*d*	*d*
264.5	*d*	*d*	*d*	*d*	*d*
T_3 (K)	*262*	*262*	*262*	*261*	*259*

FIG. 47. Runs conducted at 200 bar using TIP4P/2005 and χ = 1.115 modification. The calculated temperature is T_3 = 261.2 K with a standard deviation of 1.3 K.

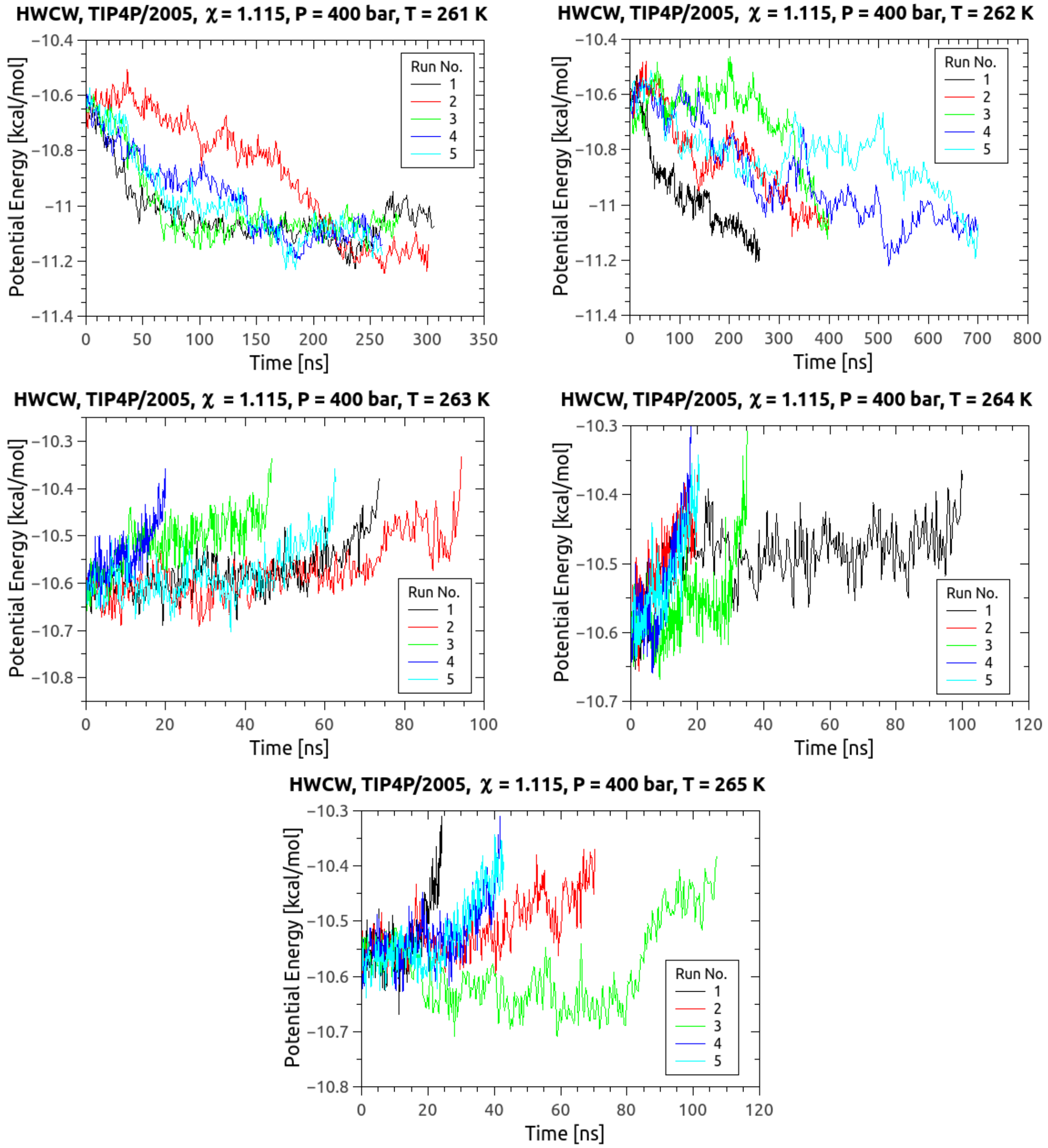

T (K)	Number 1	Number 2	Number 3	Number 4	Number 5
261	*g*	*g*	*g*	*g*	*g*
262	*g*	*g*	*g*	*g*	*g*
263	*d*	*d*	*d*	*d*	*d*
264	*d*	*d*	*d*	*d*	*d*
265	*d*	*d*	*d*	*d*	*d*
T_3 *(K)*	*262.5*	*262.5*	*262.5*	*262.5*	*262.5*

FIG. 48. Runs conducted at 400 bar using TIP4P/2005 and χ = 1.115 modification. The calculated temperature is T_3 = 262.5 K with a standard deviation of 0.0 K.

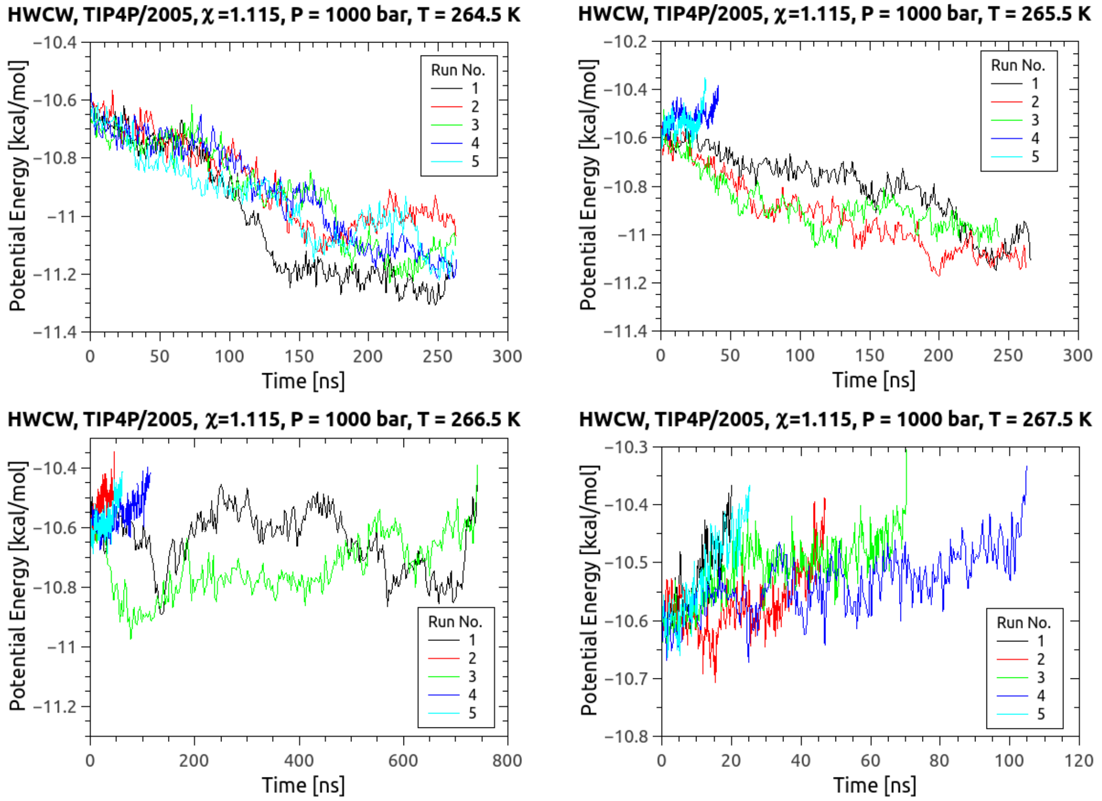

T (K)	Number 1	Number 2	Number 3	Number 4	Number 5
264.5	*g*	*g*	*g*	*g*	*g*
265.5	*g*	*g*	*g*	*d*	*d*
266.5	*d*	*d*	*d*	*d*	*d*
267.5	*d*	*d*	*d*	*d*	*d*
T_3 *(K)*	*266*	*266*	*266*	*265*	*265*

FIG. 49. Runs conducted at 1000 bar using TIP4P/2005 and χ = 1.115 modification. The calculated temperature is T_3 = 265.6 K with a standard deviation of 0.5 K.